NATIONAL ACADEMY OF SCIENCES OF UKRAINE ● G. V. KURDYUMOV INSTITUTE FOR METAL PHYSICS

A MONTHLY RESEARCH JOURNAL

METALLOPHYSICS AND ADVANCED TECHNOLOGIES

(Metallofizika i Noveishie Tekhnologii)

FOUNDED IN SEPTEMBER, 1979

Volume 48, No. 5; May 2026

CONTENTS

Editorial Announcements	Information for Foreign Subscribers	V
	Information for Contributors	VII
Crystal-Lattice Defects	Characterization of the Defect Structure of Crystalline Compounds by the Total Integrated-Reflectivity Method *V. B. MOLODKIN, I. M. FODCHUK, A. R. KUZMIN, V. V. DOVGANYUK, I. I. HUTSULIAK, M. S. SOLODKYI, R. A. ZAPLITNYY, Ya. D. GARABAZHIV, and V. V. LIZUNOV*	449
	Influence of Annealing on the CTE of Sintered Al–Si–Ni and Al–TiC Materials *V. V. KAVERINSKIY, G. A. BAGLIUK, S. F. KYRYLIUK, Z. P. SUKHENKO, I. M. KIRIAN, and O. D. RUD*	463
Phase Transformations	The Effect of Hot Deformation in the α and α + β Phase Fields on the Microstructure and Precipitate Evolution of the Zr–Sn–Nb–Fe Alloy *A. W. ALDEEN, D. Y. MAHDI, and M. S. TUMA*	483
Metal-Containing Smart Materials	Functional Nanostructured Composites Based on Ternary and Quaternary Copper Compounds *A. M. TITENKO, L. D. DEMCHENKO, Yu. M. TROSHCHENKOV, O. A. TITENKO, and V. M. MURAVYOV*	495
Metallic Surfaces and Films	Formation of Manganese-Silicide Films by Magnetron Sputtering, Measurement of Crystal Structure, Thermoelectric and Electrophysical Parameters *K. T. DOVRANOV, M. T. NORMURADOV, I. R. BEKPULATOV, T. O. BUZRUKOV, E. O. DAVRANOV, R. YORKULOV, and I. AKBAROV*	513

CONTENTS, No. 5 (Vol. 48)

	Young's Modulus of Sub-10 nm MgO Films *via* the Tunnelling-Current Nanoindenter Method *V. O. BURLAKOV and O. V. FILATOV*	527
Physics of Strength and Plasticity	Wear Behaviour of AA 7075 Joints Made by Double-Side Friction Stir Welding *V. KIRAN KUMAR, K. V. DURGA RAJESH, S. R. KOTESWARA RAO, P. VENKATESWARA BABU, and T. SRINIVASA RAO*	537

Scientific Editors of Issue—*O. S. Gatsenko, V. A. Tatarenko*
Executive Managing Editor—*O. S. Gatsenko*
Editors—*L. I. Makarenko, M. V. Manilo, I. V. Zagorulko*
The artwork for direct reproduction is made by computer group of EPD of the G. V. Kurdyumov Institute for Metal Physics, N.A.S. of Ukraine

Editorial Office Address:
G. V. Kurdyumov Institute for Metal Physics, N.A.S. of Ukraine, EPD—'MNT',
36 Academician Vernadsky Boulevard, UA-03142 Kyiv, Ukraine
Telephone: +380 44 4249042. Fax: +380 44 4242561. E-mail: mfint@imp.kiev.ua
Media Identifier R30-03171

Approved for publication by the Academic Council of the G. V. Kurdyumov Institute for Metal Physics of the National Academy of Sciences of Ukraine
Published in English or Ukrainian languages according to resolution of Editorial Board of the journal

Printed by Publishing House 'Akademperiodyka', of the NAS of Ukraine
4 Tereshchenkivs'ka Str., UA-01024 Kyiv, Ukraine
Registration Certificate of Publishing Subject: ДК № 544 on 27.07.2001

Journal website: http://mfint.imp.kiev.ua
Journal DOI: https://doi.org/10.15407/mfint

Issue DOI: https://doi.org/10.15407/mfint.48.05

НАЦІОНАЛЬНА АКАДЕМІЯ НАУК УКРАЇНИ ● ІНСТИТУТ МЕТАЛОФІЗИКИ ім. Г. В. Курдюмова

МЕТАЛОФІЗИКА ТА НОВІТНІ ТЕХНОЛОГІЇ

ЩОМІСЯЧНИЙ НАУКОВИЙ ЖУРНАЛ
ЗАСНОВАНИЙ У ВЕРЕСНІ 1979 р.

Том 48, № 5; травень, 2026

ЗМІСТ

Редакційні оголошення	Інформація для закордонних передплатників	V
	Інформація для авторів	VII
Дефекти кристалічної ґратниці	Характеризація дефектної структури кристалічних сполук методом повної інтеґральної відбивної здатности *В. Б. МОЛОДКІН, І. М. ФОДЧУК, А. Р. КУЗЬМІН, В. В. ДОВГАНЮК, І. І. ГУЦУЛЯК, М. С. СОЛОДКИЙ, Р. А. ЗАПЛІТНИЙ, Я. Д. ГАРАБАЖІВ, В. В. ЛІЗУНОВ*	449
	Вплив відпалу на коефіцієнт термічного розширення спечених матеріялів Al–Si–Ni й Al–TiC *В. В. КАВЕРІНСЬКИЙ, Г. А. БАГЛЮК, С. Ф. КИРИЛЮК, З. П. СУХЕНКО, І. М. КІР'ЯН, О. Д. РУДЬ*	463
Фазові перетворення	Вплив гарячої деформації в фазових полях α та $\alpha + \beta$ на мікроструктуру та еволюцію осаду стопу Zr–Sn–Nb–Fe *А. В. ОЛДІН, Д. Й. МАХДІ, М. С. ТУМА*	483
Металовмісні смарт-матеріяли	Функціональні наноструктуровані композити на основі потрійних і четверних сполук Купруму *А. М. ТІТЕНКО, Л. Д. ДЕМЧЕНКО, Ю. М. ТРОЩЕНКОВ, О. А. ТІТЕНКО, В. М. МУРАВЙОВ*	495
Металічні поверхні та плівки	Формування плівок силіциду Манґану методом магнетронного розпорошення, міряння кристалічної структури, термоелектричних та електрофізичних параметрів *К. Т. ДОВРАНОВ, М. Т. НОРМУРАДОВ, І. Р. БЕКПУЛАТОВ, Т. О. БУЗРУКОВ, Е. О. ДАВРАНОВ, Р. ЙОРКУЛОВ, І. АКБАРОВ*	513
	Модуль Юнґа плівок MgO товщиною менше 10 нм, визначений методом наноіндентора з тунельним	

струмом
В. О. БУРЛАКОВ, О. В. ФІЛАТОВ 527

Фізика міцності та пластичності

Зношування з'єднань криці АА 7075, виготовлених двостороннім зварюванням тертям з перемішуванням
В. КІРАН КУМАР, К. В. ДУРГА РАДЖЕШ, С. Р. КОТЕСВАРА РАО, П. ВЕНКАТЕШВАРА БАБУ, Т. СРІНІВАСА РАО 537

Наукові редактори випуску: *О. С. Гаценко, В. А. Татаренко*
Відповідальний секретар редакційної колегії *О. С. Гаценко*
Редактор-коректор *О. С. Гаценко*
Технічні редактори: *І. В. Загорулько, Л. І. Макаренко, М. В. Маніло*
Художні редактори: *І. В. Загорулько, Л. І. Макаренко, М. В. Маніло*
Оригінал-макет для прямого репродукування виготовлено комп'ютерною групою РВВ Інституту металофізики ім. Г. В. Курдюмова НАН України

Адреса редакції:
Інститут металофізики ім. Г. В. Курдюмова НАН України, РВВ—Редакція «МНТ»
бульв. Акад. Вернадського, 36; 03142 Київ, Україна
Тел.: +380 44 4249042; факс: +380 44 4242561
Ел. пошта: mfint@imp.kiev.ua
Ідентифікатор медіа R30-03171

Затверджено до друку вченою радою Інституту металофізики ім. Г. В. Курдюмова НАН України
Друкується за постановою редакційної колегії журналу англійською або українською мовами

Підписано до друку 28.05.2026 р. Формат 70×100/16.
Ум. друк. арк. 8,78. Обл.-вид. арк. 8,07.
Тираж 55 пр. Зам. № 0000 від 29.05.2026 р.

Віддруковано ВД «Академперіодика» НАН України
вул. Терещенківська, 4; 01024 Київ, Україна
Свідоцтво суб'єкта видавничої справи ДК № 544 від 27.07.2001 р.

Сайт журналу: http://mfint.imp.kiev.ua
DOI (журналу): https://doi.org/10.15407/mfint
DOI (випуску): https://doi.org/10.15407/mfint.48.05

INFORMATION (GUIDELINES) FOR CONTRIBUTORS

Submission of Manuscripts: Manuscripts should be sent by e-mail (mfint@imp.kiev.ua). Additionally, they can be sent by regular mail to Executive Managing Editor, Editorial Office, G. V. Kurdyumov Institute for Metal Physics, N.A.S. of Ukraine, 36 Academician Vernadsky Boulevard, UA-03142 Kyiv, Ukraine. Manuscripts may also be submitted to a member of the Editorial Advisory Board or to the appropriate Regional Editor who is familiar with the research presented.
Submission of a paper to '*Metallophysics and Advanced Technologies*' (transliteration: '*Metallofizika i Noveishie Tekhnologii*', *i.e.*, '*MfNT*') will be taken to imply that it represents original work not previously published, that it is not being considered for publication elsewhere, and that, if accepted for publication, it will not be republished without the consent of the Editors and Publisher. It is a condition of acceptance by the Editor of a manuscript for publication that the Publishers acquire automatically the copyright in the manuscript throughout the world. Journal '*MfNT*' supports the generally accepted principles described in documents on publication ethics and unacceptable practices, which are presented on the journal website.
Scope of the Journal: *Electronic Structure and Properties, Crystal-Lattice Defects, Phase Transformations, Physics of Strength and Plasticity, Metallic Surfaces and Films, Structure and Properties of Nanoscale and Mesoscopic Materials, Amorphous and Liquid States, Interactions of Radiation and Particles with Condensed Matter, Materials in Extremal Conditions, Reactor and Aerospace Metals Science, Medical Metals Science, New Metallic Materials and Synthetic Metals, Metal-Containing Smart Materials, Physical and Technical Basis of Experiment and Diagnostics, Articles under Discussion*.
Language: The language of publication may be English (preferably) or Ukrainian.
Abstract: Each paper requires an abstract of 200–250 words summarizing the significant coverage and findings (the use of mathematical symbols and expressions in abstract is not recommended).
Keywords and PACS numbers: 5–7 keywords and PACS numbers reflecting the content of the contribution should be supplied (see 'Physics and Astronomy Classification Scheme 2010').
Manuscript Preparation: Papers should be formatted according to the template, which can be downloaded from the Journal's website. The length of **research papers** should not in general exceed 5000 words and 10 figures; **review articles** should not exceed 10000 words and 30 figures, including tables and diagrams. Authors are urged to arrange the subject matter clearly under headings such as: 1. Introduction, 2. Experimental/Theoretical Details, 3. Results, 4. Discussion, 5. Conclusion, References. Subsections should be identified with section and subsection numbers (such as 6.1. Second-Value Subheading).
References and Notes: Notes are indicated in the text by consecutive superior Arabic numbers (without parentheses). References should be numbered consecutively (in square brackets) throughout the text. The full list should be collected and typed at the end of the paper in numerical order. Listed references should be completed in all details including **DOI** (if available) but excluding article titles in journals. **All authors'** initials should precede their names. Examples of references preparation:

1. S. O. Firstov and T. G. Rogul, *Metallofiz. Noveishie Tekhnol.*, **44**, No. 1: 127 (2022) (in Ukrainian). https://doi.org/10.15407/mfint.44.01.0127
2. V. B. Tarelnyk, O. P. Gaponova, and Ye. V. Konoplianchenko, *Prog. Phys. Met.*, **23**, No. 1: 27 (2022). https://doi.org/10.15407/ufm.23.01.027
3. A. Meisel, G. Leonhardt, and R. Szargan, *Röntgenspektren und Chemische Bindung* [X-Ray Spectra and Chemical Bond] (Leipzig: Akademische Verlagsgesellschaft Geest & Portig K.-G.: 1977) (in German).
4. J. M. Ziman, *Printsipy Teorii Tverdogo Tela* [Principles of the Theory of Solids] (Moscow: Mir: 1974) (Russian translation).
5. M. A. Stucke, D. M. Dimiduk, and D. M. Hazzledine, *High Temperature Ordered Intermetallic Alloys. V* (Eds. I. Baker and R. Darolia) (Pittsburgh, PA, USA: MRS: 1993), p. 471.
6. *Handbook of Mathematical Functions with Formulas, Graphs and Mathematical Tables* (Eds. M. Abramowitz and I. A. Stegun), Nat'l Bureau of Standards. Appl. Math. Ser. Vol. **55** (Washington, D.C.: U.S. Govt. Printing Office: 1964).
7. B. B. Karpovych and O. B. Borovkoff, *Proc. of Symp. 'Micromaterials Engineering' (Dec. 25–31, 1999)* (Kyiv: RVV IMF: 2000), vol. **2**, p. 113 (in Russian).
8. A. E. Krug, *Abstr. Int. Conf. Phys. Phenomena (Dec. 25–31, 1991, Alushta)* (Kharkiv: 1991), p. 12.
9. T. M. Radchenko, *Vplyv Uporyadkuvannya Defektnoyi Struktury на Transportni Vlastyvosti Zmishanykh Krystaliv* [Influence of Ordering of the Defect Structure on Transport Properties of the Mixed Crystals] (Thesis of Disser. for the Degree of Dr. Phys.-Math. Sci.) (Kyiv: G. V. Kurdyumov Institute for Metal Physics, N.A.S.U.: 2015) (in Ukrainian). https://doi.org/10.13140/RG.2.2.35430.22089

10. E. M. Gololobov, V. B. Shipilo, N. I. Sedrenok, and A. I. Dudyak, *Sposob Polucheniya Karbonitridov Metallov* [Production Method of Metal Carbonitrides], Authors' Certificate 722341 SSSR (Publ. November 21, 1979) (in Russian).
11. V. G. Trubachev, K. V. Chuistov, V. N. Gorshkov, and A. E. Perekos, *Sposob Polucheniya Metallicheskikh Poroshkov* [The Technology of Metallic Powder Production]: Patent 1639892 SU. MKI, B22 F9/02, 9/14 (Otkrytiya i Izobreteniya, **34**, No. 13: 11) (1991) (in Russian).
12. Yu. M. Koval' and V. V. Nemoshkalenko, *O Prirode Martensitnykh Prevrashcheniy* [On the Nature of Martensitic Transformations] (Kyiv: 1998) (Prepr./N.A.S. of Ukraine. Inst. for Metal Physics. No. 1, 1998) (in Russian).

Journal title abbreviations should conform to generally accepted styles:
https://www.cas.org/support/documentation/references/corejournals;
https://cdn.journals.aps.org/files/rmpguapb.pdf;
https://images.webofknowledge.com/WOK46P9/help/WOS/A_abrvjt.html;
https://mathscinet.ams.org/msnhtml/serials.pdf.

Equations and Formulae: Formulas in the text should be inserted by **MathType**, fully compatible with MS Office. Vectors should be typed in bold without arrows above. Note that complicated formulae, mathematical expressions or (de)notations are not recommended in the title, abstract, and keywords.

Tables: Number tables consecutively with Arabic numerals and give a clear descriptive caption at the top.

Figures: All figures should be numbered with consecutive Arabic numbers, have descriptive captions and be mentioned in the text. Keep figures separate at the end of the text and clearly label each figure with author's name and figure number. The labels at axis should contain the designation (or notation) of quantities and their units.

Preparation: Figures submitted must be of a high enough standard for reproduction with 300–600 dpi resolution (including half-tone illustrations). Redrawing or retouching of unusable figures will be charged to the authors.

Colour Plates: Whenever, the use of colour is an integral part of the research, or where the work is generated in colour, the Journal will publish (in paper version) the colour illustrations with charge to the author. Reprints in colour will carry a surcharge. Please write to the Publisher for details.

Submission of Electronic Text: Authors should submit the electronic version of their paper by e-mail to the Editorial Office. The text file should be saved in the native formats of the MS Word with a name consisting the name of the first author, for example, Hotovchenko.docx. The electronic form of figures (in TIF, EPS, JPG, PNG formats preferably and with name consisting the name of the first author also, for example, Hotovchenko_fig2a.jpg) should be planned so that they reduce to 12.7 cm column width (or less), and keep them separated from the text file. It is desirable to submit additionally all the **figures** within the format of the program, in which they were created.

Proofs: Contributors will receive page proofs for correction by e-mail as a PDF document. These must be returned to Kyiv office (mfint@imp.kiev.ua with subject beginning by word 'mfint') within 5 days of receipt.

Page Charges: There are no page charges to individuals or institutions.

Reprints: Authors can freely download a PDF version of their published article from journal website: https://mfint.imp.kiev.ua. The printed issues may be ordered by completing the appropriate form sent with proofs and prepaid by authors under the terms as for subscription.

Further Information: All questions arising during the **peer review** or after acceptance of manuscripts, especially those relating to reprints, should be directed to G. V. Kurdyumov Institute for Metal Physics, N.A.S. of Ukraine, Executive Managing Editor, Editorial Office, 36 Academician Vernadsky Blvd., UA-03142 Kyiv, Ukraine;
Fax: +380 44 4242561, e-mail: mfint@imp.kiev.ua (with subject beginning by word 'mfint').

We ask the authors to apply with their manuscript Copyright Transfer Agreement form.

Copyright Transfer Agreement

We, the undersigned authors of the manuscript '_____', transfer to the Founders, Publisher, and Editorial Board of the Journal 'Metallophysics and Advanced Technologies' (according to agreements between them) the right to publish this manuscript in original language or in translation to the other languages. We confirm that publication of this manuscript **will not** infringe a copyright of other persons or organizations and publication ethics.

Author(s):_____
(Last Name, First Name, Affiliation)

Correspondence Address:_____

Phone and e-mail: _____

_____ _____
(Signature) *(Date)*

ІНФОРМАЦІЯ (ПРАВИЛА) ДЛЯ АВТОРІВ

Науковий журнал «Металофізика та новітні технології» (МфНТ) щомісяця публікує статті, які раніше ще не публікувалися та не перебувають на розгляді для опублікування в інших виданнях. Статті мають містити результати експериментальних і теоретичних досліджень в області фізики та технологій металів, стопів і сполук з металічними властивостями; рецензії на монографії; інформацію про конференції, семінари; відомості з історії металофізики; рекламу нових технологій, матеріялів, приладів. Журнал дотримується загальноприйнятих принципів, зазначених на його сайті в документах з публікаційної етики та щодо неприйнятних практик.

Тематика журналу: *Електронні структура та властивості, Дефекти кристалічної ґратниці, Фазові перетворення, Фізика міцности та пластичности, Металічні поверхні та плівки, Будова та властивості наномасштабних і мезоскопічних матеріялів, Аморфний і рідкий стани, Взаємодії випромінення та частинок із конденсованою речовиною, Матеріяли в екстремальних умовах, Реакторне й авіакосмічне металознавство, Медичне металознавство, Нові металеві матеріяли та синтетичні метали, Металовмісні смарт-матеріяли, Фізико-технічні основи експерименту та діягностики, Дискусійні повідомлення*.

Статті публікуються однією з двох мов: англійською (віддається перевага) або українською.

Статті, в оформленні яких не дотримано наступних правил для опублікування в МфНТ, повертаються авторам без розгляду по суті. (Датою надходження вважається день повторного надання статті після дотримання зазначених нижче правил.)

1. Стаття має бути підписаною всіма авторами (із зазначенням їхніх адрес електронної пошти); слід вказати прізвище, ім'я та по батькові автора, з яким редакція буде вести листування, його поштову адресу, номери телефону та факсу й адресу електронної пошти.

2. Виклад матеріялу має бути чітким, **структурованим** (розділами, наприклад, «1. Вступ», «2. Експериментальна/Теоретична методика», «3. Результати та їх обговорення», «4. Висновки», «Цитована література»), стислим, без довгих преамбул, відхилень і повторів, а також без дублювання в тексті даних таблиць, рисунків і підписів до них. Анотація та розділ «Висновки» мають не дублювати один одного. Числові дані слід наводити в загальноприйнятих одиницях.

3. Об'єм оригінальної (неоглядової) статті має бути не більше 5000 слів (з урахуванням основного тексту, таблиць, підписів до рисунків, списку використаних джерел) і 10 рисунків. **Об'єм оглядової статті** — до 10000 слів та 30 рисунків.

4. За потреби до редакції може надаватися друкований (А4, подвійний інтервал) примірник рукопису з ілюстраціями.

5. До редакції обов'язково надається (по **e-mail**) файл статті, набраний у текстовому редакторі Microsoft Word, з назвою, що складається з прізвища першого автора (латиницею), наприклад, Hotovchenko.docx.

6. Електронна версія рукопису та його друкований варіянт (в разі його надання) мають бути ідентичними. Вони мають оформлюватися за шаблоном, який можна завантажити з сайту журналу, і містити 5–7 **індексів PACS** в редакції 'Physics and Astronomy Classification Scheme 2010'. Тексти статей мають також містити **назву статті**, **список авторів**, **повні назви** та **поштові адреси установ**, в яких вони працюють, **анотацію статті** (200–250 слів), **5–7 ключових слів** двома мовами (**англійською** та **українською**), а заголовки таблиць і підписи до рисунків мають подаватися **як мовою рукопису, так і англійською мовою**; англомовна анотація може бути представленою в більш розгорнутому варіянті (до 500 слів). Назва статті, її анотація та ключові слова мають не містити складні формули, математичні вирази чи позначення.

7. Електронні версії рисунків мають бути представленими у вигляді окремих файлів (у форматах TIF, EPS, JPG, PNG з розріжненням у 300–600 dpi) з назвами, що складаються з прізвища першого автора (латиницею) та номера рисунка, наприклад, Hotovchenko_fig2a.jpg. Додатково рисунки надаються у форматі програми, в якій вони створювалися.

8. Написи на рисунках (особливо на півтонових) слід по можливості замінити літерними позначеннями (набраними на контрастному фоні), а криві позначити цифрами або різними типами ліній/маркерів, які мають бути роз'ясненими в підписах до рисунків або в тексті. На графіках усі лінії/маркери мають бути достатньої товщини/розміру для якісного відтворення їх у зменшеному в 2–3 рази вигляді (рекомендована початкова ширина рисунка — 12,7 см). Світлини мають бути чіткими та контрастними, а написи та позначення мають не закривати істотні деталі (для чого можна використовувати стрілки). Замість зазначення в підтекстовці збільшення під час зйомки бажано проставити масштаб (на контрастному фоні) на одній з ідентичних світлин. На графіках підписи до осей, **виконані мовою статті**, мають містити позначення (або найменування) величин, що відкладаються вздовж осей, і відділені комою їхні одиниці вимірювання.

9. Формули в текст треба вставляти за допомогою редактора формул **MathType**, сумісного з MS Office. **Вектори** слід набирати напівтовстим шрифтом без стрілок зверху.

10. Рисунки, таблиці, формули, а також підрядкові **примітки (виноски)** мають нумеруватися поспіль по всій статті.

11. Посилання на літературні джерела слід давати у вигляді порядкового номера, надрукованого в рядок у квадратних дужках. Список цитованої літератури складається почергово за першою згадкою джерела. Приклади оформлення посилань наведено нижче (просимо звернути увагу на порядок розташування ініціалів і прізвищ авторів, бібліографічних відомостей і на розділові знаки, а також на необхідність зазначення **всіх** співавторів цитованої роботи та її ідентифікатора **DOI**, якщо він є):

1. S. O. Firstov and T. G. Rogul, *Metallofiz. Noveishie Tekhnol.*, **44**, No. 1: 127 (2022) (in Ukrainian). https://doi.org/10.15407/mfint.44.01.0127
2. V. B. Tarelnyk, O. P. Gaponova, and Ye. V. Konoplianchenko, *Prog. Phys. Met.*, **23**, No. 1: 27 (2022). https://doi.org/10.15407/ufm.23.01.027
3. A. Meisel, G. Leonhardt, and R. Szargan, *Röntgenspektren und Chemische Bindung* [X-Ray Spectra and Chemical Bond] (Leipzig: Akademische Verlagsgesellschaft Geest & Portig K.-G.: 1977) (in German).
4. J. M. Ziman, *Printsipy Teorii Tverdogo Tela* [Principles of the Theory of Solids] (Moscow: Mir: 1974) (Russian translation).
5. M. A. Stucke, D. M. Dimiduk, and D. M. Hazzledine, *High Temperature Ordered Intermetallic Alloys. V* (Eds. I. Baker and R. Darolia) (Pittsburgh, PA, USA: MRS: 1993), p. 471.
6. *Handbook of Mathematical Functions with Formulas, Graphs and Mathematical Tables* (Eds. M. Abramowitz and I. A. Stegun), Nat'l Bureau of Standards. Appl. Math. Ser. Vol. **55** (Washington, D.C.: U.S. Govt. Printing Office: 1964).
7. B. B. Karpovych and O. B. Borovkoff, *Proc. of Symp. 'Micromaterials Engineering' (Dec. 25–31, 1999)* (Kyiv: RVV IMF: 2000), vol. **2**, p. 113 (in Russian).
8. A. Eh. Krug, *Abstr. Int. Conf. Phys. Phenomena (Dec. 25–31, 1991, Alushta)* (Kharkiv: 1991), p. 12.
9. T. M. Radchenko, *Vplyv Uporyadkuvannya Defektnoyi Struktury na Transportni Vlastyvosti Zmishanykh Krystaliv* [Influence of Ordering of the Defect Structure on Transport Properties of the Mixed Crystals] (Thesis of Disser. for the Degree of Dr. Phys.-Math. Sci.) (Kyiv: G. V. Kurdyumov Institute for Metal Physics, N.A.S.U.: 2015) (in Ukrainian). https://doi.org/10.13140/RG.2.2.35430.22089
10. E. M. Gololobov, V. B. Shipilo, N. I. Sedrenok, and A. I. Dudyak, *Sposob Polucheniya Karbonitridov Metallov* [Production Method of Metal Carbonitrides], Authors' Certificate 722341 SSSR (Publ. November 21, 1979) (in Russian).
11. V. G. Trubachev, K. V. Chuistov, V. N. Gorshkov, and A. E. Perekos, *Sposob Polucheniya Metallicheskikh Poroshkov* [The Technology of Metallic Powder Production]: Patent 1639892 SU. MKI, B22 F9/02, 9/14 (Otkrytiya i Izobreteniya, **34**, No. 13: 11) (1991) (in Russian).
12. Yu. M. Koval' and V. V. Nemoshkalenko, *O Prirode Martensitnykh Prevrashcheniy* [On the Nature of Martensitic Transformations] (Kyiv: 1998) (Prepr./N.A.S. of Ukraine. Inst. for Metal Physics. No. 1, 1998) (in Russian).

Слід використовувати загальноприйняті скорочення назв журналів:
https://www.cas.org/support/documentation/references/corejournals;
https://cdn.journals.aps.org/files/rmpguapb.pdf;
https://images.webofknowledge.com/WOK46P9/help/WOS/A_abrvjt.html;
https://mathscinet.ams.org/msnhtml/serials.pdf.

Необхідною вимогою є також надання авторами додаткового списку цитованої літератури (**References**) в **латинській транслітерації** (система **BGN/PCGN**; рекомендовані транслітератори: http://www.slovnyk.ua/services/translit.php; http://ru.translit.net/?account=bgn).

Після транслітерованих назв книг, дисертацій, патентів та ін. слід у квадратних дужках наводити їхній англомовний переклад (див. приклади вище). При транслітерації статей з МфНТ слід використовувати написання П.І.Б. авторів, наведені **лише** в англомовному змісті відповідного випуску, і **офіційну** транслітеровану назву журналу (див. також першу сторінку кожної статті та сайт).

12. Коректура авторам надсилається електронною поштою у вигляді pdf-файлу після завершення етапу **рецензування**. На перевірку коректури авторам відводяться 5 робочих днів. Після закінчення зазначеного терміну стаття автоматично направляється до друку. Виправлення слід відмітити та прокоментувати в самому pdf-файлі або оформити у вигляді переліку виправлень (підписаного уповноваженим представником колективу авторів) і переслати електронною поштою на адресу редакції.

Електронний варіянт статті надсилається на e-mail: mfint@imp.kiev.ua (з темою, що починається словом 'mfint'). Друкована версія рукопису (якщо у ній є потреба) надсилається за адресою: **Інститут металофізики ім. Г. В. Курдюмова НАН України, редакція МфНТ; бульвар Акад. Вернадського, 36; 03142 Київ, Україна** або відповідному реґіональному редактору (див. сайт).

Автори можуть вільно завантажити pdf-файли опублікованих статей з сайту журналу (https://mfint.imp.kiev.ua), а також замовити друковані примірники випуску журналу зі своєю статтею, надіславши до редакції журналу **разом з коректурою відповідну заявку та квитанцію про оплату** друку необхідної кількості примірників випуску на умовах, аналогічних передплатним.

Відповідно до угод між редакцією МфНТ, засновниками та видавцем журналу, редакція вважає, що автори, надсилаючи їй рукопис статті, передають засновникам, видавцю та редколеґії право опублікувати цей рукопис мовою ориґіналу та в перекладі іншими мовами, і просить авторів відразу прикладати до рукопису «Угоду про передачу авторського права».

Угода про передачу авторського права

Ми, що нижче підписалися, автори рукопису «_____», передаємо засновникам, видавцю та редколеґії журналу «Металофізика та новітні технології» (згідно з угодами між ними) право опублікувати цей рукопис мовою ориґіналу та в перекладі іншими мовами. Ми підтверджуємо, що ця публікація **не** порушує авторського права інших осіб або організацій і принципів наукової етики. При цьому за авторами зберігаються всі інші права як власників цього рукопису.

Підписи авторів: _____ (П.І.Б., дата, адреса, тел., e-mail)

Metallophysics and Advanced Technologies
Металофіз. новітні технол.
Metallofiz. Noveishie Tekhnol.
2026, vol. 48, No. 5, pp. 449–462
https://doi.org/10.15407/mfint.48.05.0449
Reprints available directly from the publisher

PACS numbers: 07.85.-m, 61.05.cc, 61.05.cp, 61.72.Dd, 61.72.J-, 61.72.Lk

Characterization of the Defect Structure of Crystalline Compounds by the Total Integrated-Reflectivity Method

V. B. Molodkin, I. M. Fodchuk*, A. R. Kuzmin*, V. V. Dovganyuk*, I. I. Hutsuliak*, M. S. Solodkyi*, R. A. Zaplitnyy*, Ya. D. Garabazhiv*, and V. V. Lizunov

G. V. Kurdyumov Institute for Metal Physics, N.A.S. of Ukraine,
36 Academician Vernadsky Blvd.,
UA-03142 Kyiv, Ukraine
**Yuriy Fedkovych Chernivtsi National University,*
2 Kotsyubynsky Str.,
UA-58002 Chernivtsi, Ukraine

The defect structure of crystalline compounds is investigated using the total integrated-reflectivity method. For interpretation of the experimental data, a generalized dynamical theory of x-ray diffraction is applied to real crystals containing randomly distributed microdefects of various types and a disturbed surface layer. The dynamics of the concentration and size variations are analysed for several types of interconnected dominant defects, including spherical and disk-shaped clusters, as well as dislocation loops.

Key words: total integrated reflectivity, high-resolution x-ray diffractometry, dynamical theory, kinematical theory, diffraction curves, crystalline compounds.

Досліджено дефектну структуру кристалічних сполук методою повної інтеґральної відбивної здатности. Для інтерпретації експериментальних даних використано узагальнену динамічну теорію дифракції Х-променів

Corresponding author: Ihor Mykhaylovych Fodchuk
E-mail: ifodchuk@ukr.net

Citation: V. B. Molodkin, I. M. Fodchuk, A. R. Kuzmin, V. V. Dovganyuk, I. I. Hutsuliak, M. S. Solodkyi, R. A. Zaplitnyy, Ya. D. Garabazhiv, and V. V. Lizunov, Characterization of the Defect Structure of Crystalline Compounds by the Total Integrated-Reflectivity Method, *Metallofiz. Noveishie Tekhnol.*, **48**, No. 5: 449–462 (2026). DOI: 10.15407/mfint.48.05.0449

у реальних кристалах з хаотично розподіленими мікродефектами різних типів і порушеним приповерхневим шаром. Досліджено динаміку зміни концентрацій і розмірів декількох типів взаємопов'язаних домінувальних дефектів (сферичні та дископодібні кластери, дислокаційні петлі).

Ключові слова: повна інтеґральна відбивна здатність, високороздільча Х-променева дифрактометрія, динамічна теорія, кінематична теорія, криві дифракційного відбивання, кристалічні сполуки.

(Received 3 March, 2026; in final version, 16 April, 2026)

1. INTRODUCTION

This article is dedicated to the memory of Prof. V. B. Molodkin, Corresponding Member of the National Academy of Sciences of Ukraine.

Over the recent decades V. B. Molodkin and his colleagues working at G. V. Kurdyumov Institute for Metal Physics, NAS of Ukraine have demonstrated the possibility of radically increasing the sensitivity and information capacity of defective structure diagnostics. This was achieved through the application of dynamical diffraction, the theoretical foundations of which were established by V. B. Molodkin [1–4].

Modern non-destructive structural diagnostics is based on the experimental study of how structural imperfections influence the diffraction scattering pattern of the investigated object using various x-ray wavelengths, followed by the structural characteristics decoding based on the pattern parameters. The kinematical theory of Bragg and diffuse scattering in crystals with defects, developed by M. O. Krivoglaz, has been and remains the theoretical basis for quantitative research on defect characteristics and their distribution [5, 6]. However, the single-scattering approximation, which underlies the kinematical theory, leads to significant limitations in its application. Specifically, the kinematical theory is effective for polycrystals and single crystals highly distorted by defects, but it becomes largely inapplicable when the dimensions of the crystals and coherent scattering regions exceed the extinction length. In such cases, the theory of multiple dynamical scattering is required [7–9].

Another drawback of the kinematical theory is that it allows for the investigation of defect characteristics only if a single dominant type is present in the crystal. This is due to the fact that the kinematical pattern remains virtually identical across all diffraction conditions; it reflects experimental measurements of the defects' influence on a single scattering pattern, from which characteristics of only one defect type can be determined. Currently, most modern devices are multiparametric, and single-crystal components simultaneously contain multiple types of defects. Furthermore, the sensitivity of kinematical scattering is insufficient for the quantitative diagnostics of even a

single defect type in structurally perfect single crystals. In this case, coherent scattering can be correctly described only within the framework of the dynamical theory of x-ray scattering [10–12], accounting for multiple scattering processes.

In addition, it was predicted and experimentally confirmed by double-axis and triple-axis diffractometry methods that dynamical effects also occur with diffuse x-ray scattering near Bragg reflections from imperfect single crystals [13–15]. In the case of Bragg diffraction geometry, these effects cause a significant reduction in diffuse scattering intensity within the total reflection region (the extinction effect) and its redistribution near the Bragg peak (anomalous transmission and absorption effects) [8, 9]. During the dynamical x-ray scattering in crystals with defects, much like in the dynamical theory for ideal crystals, the boundary conditions and diffraction geometry of the investigated crystal exert a substantial influence on the distribution and magnitude of the diffracted x-ray intensity, in contrast to the kinematical theory. Furthermore, the thickness of the crystal and the radiation energy significantly affect the behaviour of diffracted intensities in both perfect and defective crystals. Isolating and utilizing the diffuse scattering component under dynamical diffraction conditions enhances the informative potential of these methods, as diffuse scattering carries the most comprehensive and direct information regarding the structural perfection of the objects. At sufficiently high defect concentrations, they can contribute significantly to the diffuse scattering intensity in the Bragg peak region. A correct description of diffuse scattering is provided by the dynamical theory of x-ray diffraction in crystals with randomly distributed defects.

The primary advantage of angular intensity distributions is the ability to determine the concentration and size of defects, as well as their type (interstitial or vacancy) and the symmetry of the static distortion fields they create. Among these highly informative methods is the total integrated reflectivity (TIR) method, where information about defects is extracted from the full diffraction curves, which represent the distributed scattering intensity. Consequently, when considering relatively perfect single crystals with defects, it is necessary to apply diagnostics based specifically on the dynamical scattering theory [16, 17].

This approach is based on the analysis of the TIR from investigated crystal. In Refs. [18–22], the dislocation structure of crystalline compounds was studied based on the kinematical theory of x-ray scattering. In contrast, the TIR method employs the dynamical theory to obtain more comprehensive information about the defective structure. We have approved this method for crystalline compounds with a well-developed defective structure. Its application enables the estimation of the concentrations and sizes of several defect types, namely, dislocation loops, disk-shaped formations (extended blocks) and spherical

formations (grains). This method allows for the most complete and accurate diagnostics of defects within the bulk of single crystals and the determination of the parameters of disturbed surface layers.

Cadmium telluride CdTe crystalline compounds are widely used in the fabrication of x-ray and γ-ray detectors [23, 24]. However, CdTe crystals are characterized by a well-developed defect structure (various types of dislocations, dislocation loops, foreign phase inclusions, cluster formations, *etc*.), which subsequently has a negative impact on their sensing properties. Although the methods for growing high-perfection crystalline compounds improve every year, the influence of the defect structure on the electrical and spectroscopic properties of detectors remains an ever-present and relevant problem.

In the article, the using of TIR method is illustrated by the example of semiconductor materials. Nevertheless, the appropriateness of using such methods in the researching of metallic single crystals with microdefects is even higher than for semiconductors. This is due to the fact that an approximate description of the effects of radiation scattering (including dynamical effects) in such crystalline compounds can lead not only to a quantitative, but also to a qualitatively incorrect description of the defect structure. For example, the kinematical theory of scattering for single crystals with dislocations assumes a complete absence of a coherent component of the intensity. However, in the dynamical approach, taking into account the effects of multiple scattering, leads to an effective cut-off of the contribution of distant dislocations to the scattering characteristics and, as a result, even with a sufficiently high concentration of dislocations in the crystal, coherent peaks are observed.

This paper presents the results of testing the method of total integrated reflectivity and computer simulation of the defect structure for several types of defects in cadmium telluride crystalline compounds.

2. OBJECTS OF RESEARCH

The objects of research are a set of (111)CdTe crystalline compound samples from Acrorad Co., Ltd., grown by the traveling heater method, with dimensions of $5\times5\times1$ mm^3 [25, 26]. Experimental studies were conducted on a Panalytical Philips X'Pert PRO diffractometer using radiation Cu$K_{\alpha1}$. The divergence of the primary beam and the angular acceptance of the analyser crystal used before the detector is $\Delta\alpha \cong 12''$.

3. TOTAL INTEGRATED REFLECTIVITY METHOD

The generalized dynamical theory of x-ray diffraction in real crystals with randomly distributed microdefects of various types and a dis-

turbed surface layer was used to interpret the experimental results [27]. The best results were obtained for a model containing the following dominant types of microdefects: disk-shaped clusters, small spherical clusters, and dislocation loops. The presence of thermal diffuse scattering was accounted for by scattering on point defects, represented by spherical clusters with sizes equal to the covalent radii of cadmium and tellurium atoms. The strain distribution in the disturbed surface layer was represented by a multistep profile corresponding to the so-called 'layer-by-layer approximation'. Within this approximation, the disturbed layer is represented as a set of sublayers with thickness t_i, in each of which the strain epsilon is constant.

Unlike the kinematical theory, the dynamical theory introduces two additional structurally sensitive parameters (which in several cases are significantly more informative than the Krivoglaz's factor (static Debye–Waller factor E^2): these are the integrated extinction coefficients of the coherent (μ_{ds}^0) and diffuse (μ^*) components of TIR. This provides an opportunity, unavailable in the kinematical case, to determine unambiguously the parameters of several defect types simultaneously using TIR measurements [8, 9].

In the case of a uniform distribution of bounded defects with radius R_0 and concentration c, the following expression is valid [28]:

$$\begin{gathered}\mu_{ds}^0 = cE^2C^2m_0B,\ m_0 = \pi v_c H^2 \left|\chi_{Hr}\right|^2 / (2\lambda^2), \\ B = b_1 + b_2 \ln(e / r_0^2),\ b_1 = B_1 + B_2 / 3,\ b_2 = B_1 + \cos^2\theta_B B_2 / 2,\end{gathered} \tag{1}$$

where $r_0 = R_0/\Lambda$, $\Lambda = \lambda(\gamma_0\gamma_H)^{1/2}/(C\left|\chi_{Hr}\right|)$ is the extinction length, **H** is the diffraction vector, e is the base of the natural logarithm, and it is assumed that $r_0 < 1$.

For spherical clusters: $B_1 = 0$, $B_2 = (4\pi A_{cl}/v_c)^2$, $A_{cl} = \Gamma\varepsilon R_0^3$ is the cluster strength, ε is relative strain at the cluster boundary, and $\Gamma = (1+\nu)/((3(1-\nu))$. For disk-shaped clusters: $B_1 = B_2 = (4\pi A_{cl}/v_c)^2$, $A_{cl} = \Gamma\varepsilon h_p R_p^2$ is the cluster strength. For randomly distributed dislocation loops: $B_1 = 4(\pi b_0^2 / v_c)^2 / 15$, $B_2 = bB_1$, $\beta = (3\nu^2 + 6\nu - 1)/(4(1-\nu^2))$, v_c is the unit cell volume, ν is the Poisson's ratio, and **b** is the Burgers vector.

If $\mu_{ds}^0 << \mu_0$ and $r_0 << 1$, the following approximate relationship is valid [29]:

$$\begin{gathered}\mu^* \approx \mu_{ds}^0 f_\mu(r_0), \\ f_\mu(r_0) = \frac{5 + 2r_0 \ln r_0 - 3r_0/8}{3(1 - \ln r_0)} \text{ for dislocation loops}, \\ f_\mu(r_0) = \frac{4 + r_0 \ln r_0 - 2r_0}{5 - 6\ln r_0} \text{ for dislocation clusters},\end{gathered} \tag{2}$$

The relationship between the Krivoglaz's factor exponent $L_{\text{H}} = -\ln E$ and the defect characteristics is described by the following expressions:

$$L_{\text{H}} \approx 0,5cv_{\text{c}}^{-1}R_0^3(Hb)^{3/2} \text{ for dislocation loops}, \quad (3)$$

$$L_{\text{H}} \approx 0,5cn_0\eta^2(1-\eta^2/100) \text{ for spherical clusters } (\eta^2<<10), \quad (4)$$

$$L_{\text{H}} \approx cn_0\eta^{3/2} \text{ for spherical clusters } (\eta^2<<10),$$

where $n_0 \approx 4\pi R_0^3/3v_{\text{c}}$ is the number of matrix unit cells replaced by a cluster, $\eta = \alpha_0 n_0^{1/3} h$, $\alpha_0 = \Gamma\varepsilon(6\pi^2/n_0)^{1/3}$, ν_0 is the number of atoms in the cubic matrix cell, $h = Ha/2\pi$, and a is the lattice constant.

Through the parameters E, μ_{ds}^0, and μ^*, the TIR value R_{i} is linked to the defect characteristics (c, R_0, ε, b).

In the case of arbitrary (asymmetric) Bragg diffraction geometry, the expression for the TIR, which combines the limiting cases of 'thin' ($\mu_0 l << 1$) and 'thick' ($\mu_0 l >> 1$) crystals, is as follows:

$$R_{\text{i}} = R_{\text{i}}^{\text{dyn}} PE + R_{\text{i}}\Pi(1-E^2), \quad (5)$$

$R_{\text{i}}^{\text{dyn}} = 16CQ\Lambda/3\pi\gamma_0$, $R_{\text{i}} = C^2Qt/\gamma_0$ is the TIR of a perfectly mosaic crystal,

$$\Pi(\mu^*, t) = \begin{cases} (2(\mu_0+\mu^*)t/\gamma)^{-1}, & \mu_0 t >> 1, \\ (1+(\mu_0+\mu^*)t/\gamma)^{-1}, & \mu_0 t < 1,\ t >> \Lambda_B, \end{cases}, \quad (6)$$

$1/\gamma = (1/\gamma_0 + 1/|\gamma_{\text{H}}|)/2$, $\Lambda_B = l(/\gamma_0|\gamma_{\text{H}}|)^{1/2}/(2\pi C\chi_{\text{Hr}}) = L/2\pi$, $P = 1 - 3\pi s/4$ with $s = (\mu_0 + \mu_{\text{ds}}^0)\Lambda E/\gamma C$, $s << 1$, P is the polarization factor, $Q = (\pi|\chi_{\text{Hr}}|^2)/(\lambda\sin(2\theta))$ is the reflectivity per path length unit, χ_{Hr} is the real part of the Fourier component of the crystal polarizability, t is the crystal thickness, γ_0, γ_{H} are the direction cosines of the wave vectors of the plane wave incident on the crystal and the diffracted wave, respectively, relative to the inward normal to the entry surface, and μ_0 is the linear photoelectric absorption coefficient.

Here, the integrated effective absorption coefficients μ_{ds}^0 and μ^* are described by the approximate expressions (1), (2) under conditions $\mu_{\text{ds}}^0 << \mu_0$ and $R_0 << \Lambda$.

4. RESEARCH RESULTS

Experimental dependences of TIR, normalized on the reflectivity of ideal crystal, on the reflection order (extinction thickness Λ_{hkl}) are shown in Fig. 1. These dependences are non-monotonic. Samples Nos. 2 and 4 exhibit higher TIR values than sample No. 2; notably, the maximum increase in reflectivity is observed at lower reflection orders for

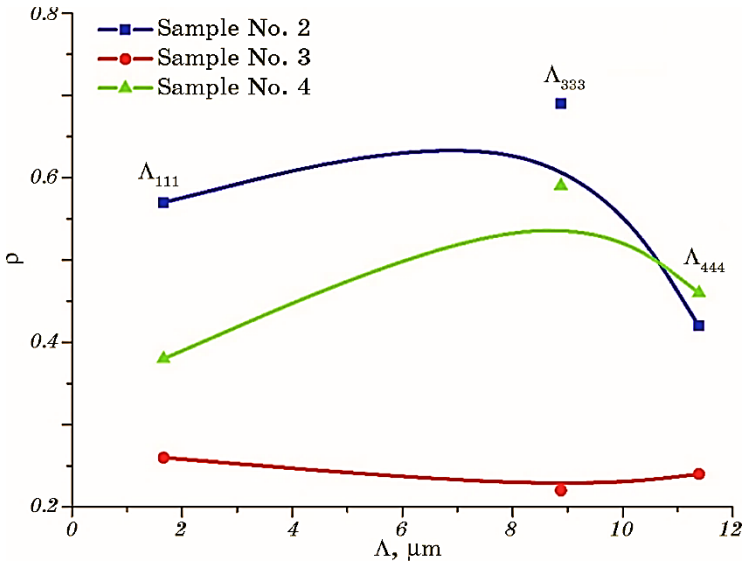

Fig. 1. Dependences of the normalized TIR ρ on the reflection order (extinction thickness values) for a set of samples.

sample No. 2. The calculation of the normalized TIR was performed with a precision of 0.01, meaning the calculated dependences of the normalized TIR on the reflection order will have same shape.

We considered several possible combinations of microdefects with different sizes and concentrations present in the investigated crystals [30]: disk-shaped clusters—relatively large CdTe grains surrounded by dislocation loops of corresponding sizes, and small spherical clusters—

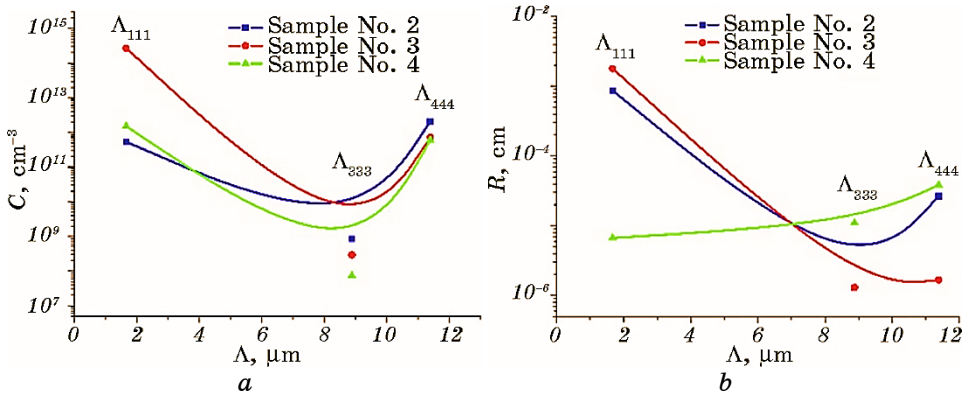

Fig. 2. Dependences of concentrations (*a*) and sizes (*b*) of dislocation loops on the reflection order.

TABLE 1. Values of concentrations C and sizes R of dislocation loops depending on the order of reflection.

Sample		Reflection		
		111	333	444
2	C, cm^{-3}	$5.3 \cdot 10^{11}$	$8.5 \cdot 10^{8}$	$2.1 \cdot 10^{11}$
3		$2.7 \cdot 10^{14}$	$2.9 \cdot 10^{8}$	$7.2 \cdot 10^{11}$
4		$1.5 \cdot 10^{12}$	$7.3 \cdot 10^{7}$	$5.6 \cdot 10^{11}$
2	R, cm	$8.7 \cdot 10^{-4}$	$1.3 \cdot 10^{-6}$	$2.6 \cdot 10^{-5}$
3		$1.8 \cdot 10^{-3}$	$1.3 \cdot 10^{-6}$	$1.6 \cdot 10^{-6}$
4		$6.7 \cdot 10^{-6}$	$1.1 \cdot 10^{-5}$	$3.8 \cdot 10^{-5}$

small CdTe grains located in the spaces between large grains; disk-shaped clusters—relatively large CdTe grains, and dislocation loops.

The best agreement between the experimental and theoretical TIR dependences (Fig. 1, $\rho = \rho_{exp} \approx \rho_{teor}$, the deviation does not exceed 1%) was obtained for the first model, which assumes the presence of three types of dominant defects in the crystal. This allowed for the determination of the characteristics (concentration and size) of the dominant defects in the crystals (Figs. 2–4, Tables 1–3).

Samples Nos. 2–4 exhibit several characteristic features on $C(\Lambda_{hkl})$ dependences (Figs. 2–4, *a*). Specifically, the concentration of dislocation loops for all samples (Fig. 2) comparing to the control sample decreases sharply from the surface to a depth of ≅ 9 μm, followed by an increase. The decrease in concentration at a depth of 9 μm is associated

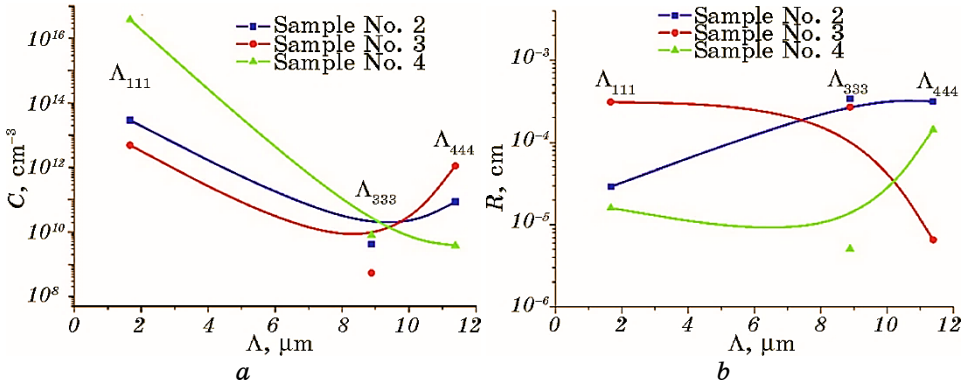

Fig. 3. Dependences of concentrations (*a*) and sizes (*b*) of disk-shaped clusters on the reflection order.

TABLE 2. Values of concentrations C and sizes R of disk-shaped clusters *versus* the reflection order.

Sample		Reflection		
		111	333	444
2	C, cm^{-3}	$2.9 \cdot 10^{13}$	$4.2 \cdot 10^{9}$	$8.5 \cdot 10^{10}$
3		$4.9 \cdot 10^{12}$	$5.4 \cdot 10^{8}$	$1.1 \cdot 10^{12}$
4		$3.8 \cdot 10^{16}$	$8.1 \cdot 10^{9}$	$3.8 \cdot 10^{9}$
2	R, cm	$2.9 \cdot 10^{-5}$	$3.4 \cdot 10^{-4}$	$3.2 \cdot 10^{-4}$
3		$3.1 \cdot 10^{-4}$	$2.7 \cdot 10^{-4}$	$6.6 \cdot 10^{-6}$
4		$1.6 \cdot 10^{-5}$	$5.1 \cdot 10^{-6}$	$1.4 \cdot 10^{-4}$

with a possible ordering of the structure, followed by its subsequent disordering deeper into the crystal. This is confirmed by the uniformity of the dislocation loop sizes at this extinction depth in samples Nos. 2 and 3. Sample No. 4 is characterized by a nearly monotonic behaviour of the $R(\Lambda_{hkl})$ dependence.

A somewhat different trend is observed in the $C(\Lambda_{hkl})$ dependences for disk-shaped clusters. Samples Nos. 2 and 3 are characterized by an inflection point in the region of the (333) reflection, followed by an increase toward (444). Sample No. 4 has a monotonic decrease with increasing Λ_{hkl}. A notable feature is that at the depth of Λ_{333}, the concentration values for all samples remain within the same order of magnitude. A completely different behaviour is observed for the size dependences $R(\Lambda)$. Sample No. 2 exhibits a monotonic curve within a single

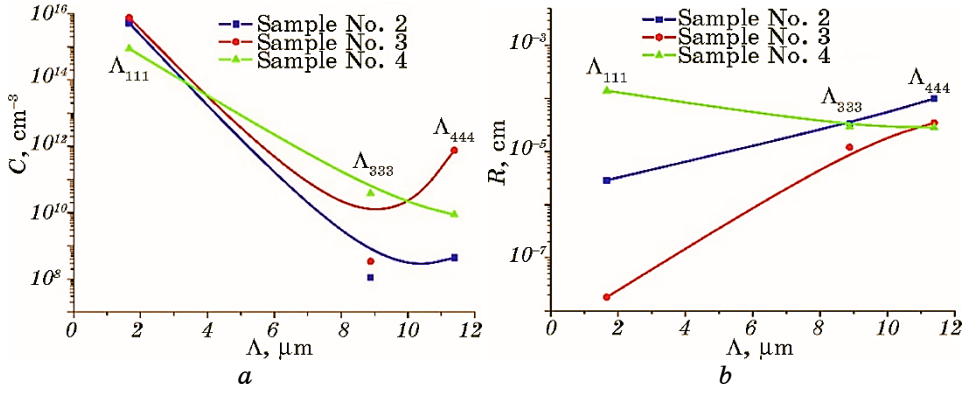

Fig. 4. Dependences of concentrations (*a*) and sizes (*b*) of spherical clusters on the reflection order.

TABLE 3. Values of concentrations C and sizes R of spherical clusters *versus* the reflection order.

Sample		Reflection		
		111	333	444
2	C, cm^{-3}	$5.2 \cdot 10^{15}$	$1.1 \cdot 10^{8}$	$4.4 \cdot 10^{8}$
3		$7.5 \cdot 10^{15}$	$3.4 \cdot 10^{8}$	$7.6 \cdot 10^{11}$
4		$8.8 \cdot 10^{14}$	$3.8 \cdot 10^{10}$	$8.7 \cdot 10^{9}$
2	R, cm	$2.9 \cdot 10^{-6}$	$3.4 \cdot 10^{-5}$	$9.9 \cdot 10^{-5}$
3		$1.8 \cdot 10^{-8}$	$1.2 \cdot 10^{-5}$	$3.5 \cdot 10^{-5}$
4		$1.4 \cdot 10^{-4}$	$2.9 \cdot 10^{-5}$	$2.9 \cdot 10^{-5}$

order of magnitude. Sample No. 3 shows a gradual decrease toward (333), which intensifies down to the depth of (444). The pattern for sample No. 4 is fundamentally different: a gradual decrease toward (333) followed by an increase toward (444).

Regarding the concentration dependences of spherical clusters for samples No. 2 and No. 3, a sharp decrease toward (333) is observed, followed by an increase in values toward (444). For sample No. 4, the curve shows a monotonic decrease in concentration values. The general behaviour of the size dependences shares a common feature for all samples—the proximity of $R(\Lambda_{hkl})$ values for higher-order reflections. The scatter of cluster size values for the (111) reflection is explained by the influence of the disturbed surface layer, with the most favourable situation observed for sample No. 3. The anomalous deviation of the $R(\Lambda_{111})$ value can be attributed to the effects of mechanical surface treatment.

5. CONCLUSIONS

The defective structure of crystalline compounds was investigated using the total integrated reflectivity method based on the dynamical theory of x-ray diffraction. The most optimal combination of microdefects was identified during the simulation process: disk-shaped clusters (representing relatively large CdTe grains) surrounded by dislocation loops of corresponding sizes, and small spherical clusters (representing small CdTe grains) located in the spaces between the large grains. The dynamics of changes in the concentration and size of microdefects as a function of the extinction depth were demonstrated.

The general behaviour of $C(\Lambda_{hkl})$ and $R(\Lambda_{hkl})$ can be explained by the significant influence of the disturbed surface layer in all samples, as a

scatter in the size values of spherical microdefects is observed across all samples, while the range of concentration variations remains minimal. For the complex consisting of a disk-shaped microdefects and a dislocation loops, the dynamics of concentration and size changes are interconnected in samples Nos. 3 and 4. For sample No. 2, a significant deviation in sizes occurs. This can be attributed to the mosaic nature of the structure and the influence of the surface and grain boundaries, with the impact of the second one increasing with depth.

Overall, the considered model of the defective structure requires further supplementation with model microdefects that would allow for a better interpretation of grain boundary effects. Nevertheless, the proposed method for calculating the defective structure yields results that correlate well with the results of previous studies of these samples.

The authors are obliged to the Armed Forces of Ukraine for providing security that made it possible to carry out this work. This work was partially supported by the Ministry of Education and Science of Ukraine (grant No. 0125U000832, authors A. R. Kuzmin, M. S. Solodkyi; grant No. 0125U001483, authors I. M. Fodchuk, I. I. Hutsuliak, V. V. Dovganyuk, R. A. Zaplitnyy). This research was also supported by the National Academy of Sciences of Ukraine under contracts No. III-1-23 'Multiparametrical phase-variation diagnostics and modelling of electromagnetic properties of structures with inhomogeneously distributed imperfections'.

AUTHORS' CONTRIBUTIONS

V.B.M. generated key ideas, methodology, and analysis. I.M.F.: conceptualization; formulation and development of overarching research goals and aims; preparation, creation, and presentation of the manuscript, specifically writing the initial draft; provision of study materials, reagents, and research samples; data curation management. A.R.K.: preparation, creation, and presentation of the manuscript, specifically critical review, commentary, or revision, including prepublication stages; application of statistical, mathematical, computational, and other methods to analyse diffraction curves and experimental TIR curves. V.V.D.: modernization of the software suite (including programming code where necessary for data interpretation) for initial use in calculating microdefect concentrations and sizes. I.I.H.: preparation and creation of the manuscript, specifically x-ray diffractometry data processing (plotting and analysis of diffraction curves); primary translation of text. M.S.S.: preparation and creation of the manuscript, specifically x-ray diffractometry data processing (plotting and analysis of experimental TIR curves). R.A.Z.: modernization of the software suite (including programming code where neces-

sary for data interpretation) for subsequent reuse in calculating microdefect concentrations and sizes. Ya.D.G.: literature review; formatting/preparation of the theoretical section and references. V.V.L.: conceptualization; formulation or development of overarching research goals and aims; preparation, creation, and presentation of the published work, specifically editing the initial draft; provision of study materials; final editing of the manuscript. All authors gave final approval of the version to be published.

REFERENCES

1. V. B. Molodkin and E. A. Tikhonova, *Fiz. Met. Metalloved.*, **24**: 385 (1967) (in Russian).
2. V. B. Molodkin, S. I. Olikhovskii, and M. E. Osinovskii, *Metallofizika*, **5**: 3 (1983) (in Russian).
3. V. B. Molodkin, S. I. Olikhovskii, and M. E. Osinovskii, *Metallofizika*, **5**: 112 (1983) (in Russian).
4. V. B. Molodkin, S. I. Olikhovskii, E. N. Kislovskii, E. G. Len, and E. V. Pervak, *phys. status solidi (b)*, **227**: 429 (2001).
5. M. A. Krivoglaz, *Diffuznoe Rasseyanie Rentgenovskikh Luchey i Neitronov na Fluktuatsionnykh Neodnorodnostyakh v Neideal'nykh Kristallakh* [Diffuse Scattering of X-Rays and Neutrons on Fluctuation Inhomogeneities in Non-Ideal Crystals] (Kiev: Naukova Dumka: 1984) (in Russian).
6. M. A. Krivoglaz, *Diffraction of X-Rays and Thermal Neutrons in Imperfect Crystals* (Berlin–Heidelberg: Springer: 1992).
7. V. M. Pylypiv, T. P. Vladimirova, I. M. Fodchuk, B. K. Ostafiychuk, Ye. M. Kyslovskyy, V. B. Molodkin, S. I. Olikhovskii, O. V. Reshetnyk, O. S. Skakunova, V. V. Lizunov, and O. Z. Garpul', *phys. status solidi (a)*, **208**: 2558 (2011).
8. V. B. Molodkin, S. I. Olikhovskii, S. V. Dmitriev, A. I. Nizkova, and V. V. Lizunov, *Acta Cryst. A*, **76**: 45 (2020).
9. V. B. Molodkin, S. I. Olikhovskii, S. V. Dmitriev, and V. V. Lizunov, *Acta Cryst. A*, **77**: 433 (2021).
10. V. V. Lizunov, V. B. Molodkin, S. V. Lizunova, N. G. Tolmachev, O. S. Skakunova, S. V. Dmitriev, B. V. Sheludchenko, S. M. Brovchuk, L. M. Skapa, R. V. Lekhnyak, V. V. Molodkin, and K. V. Fuzik, *Progress in Physics of Metals*, **15**, Iss. 2: 55 (2014) (in Russian).
11. V. V. Lizunov, V. B. Molodkin, S. V. Lizunova, N. G. Tolmachev, E. S. Skakunova, S. V. Dmitriev, B. V. Sheludchenko, S. M. Brovchuk, L. N. Skapa, R. V. Lekhnyak, and E. V. Fuzik, *Metallofiz. Noveishie Tekhnol.*, **36**, No. 7: 857 (2014) (in Russian).
12. V. V. Lizunov, S. M. Brovchuk, A. I. Nizkova, V. B. Molodkin, S. V. Lizunova, B. V. Sheludchenko, A. I. Grankina, I. I. Rudnitska, S. V. Dmitriev, M. G. Tolmachev, R. V. Lekhnyak, L. M. Skapa, and N. P. Irkha, *Metallofiz. Noveishie Tekhnol.*, **36**, No. 9: 1271 (2014) (in Russian).
13. S. I. Olikhovskii, V. B. Molodkin, E. G. Len, E. S. Skakunova, and S. V. Lizunova, *Phys. Rev. B*, **99**: 235304 (2019).
14. V. B. Molodkin, H. I. Nyzkova, V. V. Lizunov, N. G. Tolmachev, S. V. Dmitriev,

L. I. Makarenko, O. V. Reshetnik, T. P. Vladimirova, Ya. V. Vasylyk, and I. N. Zabolotnyy, *Metallofiz. Noveishie Tekhnol.*, **41**, No. 12: 1677 (2019) (in Russian).
15. V. B. Molodkin, H. I. Nyzkova, V. V. Lizunov, A. O. Bilots'ka, L. I. Makarenko, T. P. Vladimirova, O. V. Reshetnyk, Ya. V. Vasylyk, and Ye. A. Tsapko, *Metallofiz. Noveishie Tekhnol.*, **44**, No. 4: 595 (2020) (in Ukrainian).
16. V. B. Molodkin, V. Yu. Storizhko, V. P. Kladko, V. V. Lizunov, A. I. Nizkova, O. Yo. Gudymenko, S. I. Olikhovskii, M. G. Tolmachev, S. V. Dmitriev, I. I. Demchyk, E. I. Bogdanov, and B. I. Hinko, *Semiconductor Physics, Quantum Electronics and Optoelectronics*, **24**, No. 1: 5 (2021).
17. V. B. Molodkin, V. Yu. Storizhko, V. P. Kladko, V. V. Lizunov, A. I. Nizkova, O. Yo. Gudymenko, S. I. Olikhovskii, M. G. Tolmachev, S. V. Dmitriev, I. I. Demchyk, E. I. Bogdanov, and B. I. Hinko, *Semiconductor Physics, Quantum Electronics and Optoelectronics*, **26**, No. 1: 17 (2023).
18. I. Fodchuk, A. Kuzmin, I. Hutsuliak, M. Solodkyi, V. Dovganyuk, O. Maslyanchuk, Y. Roman, R. Zaplitnyy, O. Gudymenko, V. Kladko, V. Molodkin, and V. Lizunov, *Proc. of SPIE*, **11369**: 113691H (2020).
19. O. Maslyanchuk, I. Fodchuk, M. Solovan, I. Boledzyuk, A. Kuzmin, V. Gnatyuk, and T. Aoki, *Proc. of SPIE*, **12126**: 121260K (2021).
20. I. M. Fodchuk, A. R. Kuzmin, O. L. Maslyanchuk, I. I. Hutsuliak, M. S. Solodkyi, Yu. T. Roman, M. M., Solovan, and O. Yo., Gudymenko, *Phys. Chem. Solid State*, **23**, No. 1: 144 (2022).
21. I. M. Fodchuk, A. R. Kuzmin, I. I. Hutsuliak, M. D. Borcha, and V. O. Kotsyubynsky, *Semiconductor Physics, Quantum Electronics and Optoelectronics*, **26**, No. 4: 415 (2023).
22. I. M. Fodchuk, A. R. Kuzmin, I. I. Gutsuliak, M. S. Solodkyi, O. L. Maslyanchuk, Yu. T. Roman, V. P. Kladko, O. Yo. Gudymenko, V. B. Molodkin, and V. V. Lizunov, *Metallofiz. Noveishie Tekhnol.*, **43**, No. 10: 1289 (2021) (in Ukrainian).
23. V. V. Brus, O. L. Maslyanchuk, M. M. Solovan, P. D. Maryanchuk, I. M. Fodchuk, V. A. Gnatyuk, N. D. Vakhnyak, S. V. Melnychuk, and T. Aoki, *Sci. Rep.*, **9**, No. 1: 1065 (2019).
24. O. Maslyanchuk, M. Solovan, V. Brus, P. Maryanchuk, E. Maistruk, I. Fodchuk, and V. Gnatyuk, *Nucl. Instrum. Methods Phys. Res. A*, **988**: 164920 (2021).
25. H. Shiraki, M. Funaki, Y. Ando, A. Tachibana, S. Kominami, and R. Ohno, *IEEE Trans. Nucl. Sci.*, **56**, Iss. 4: 1717 (2008).
26. H. Shiraki, M. Funaki, Y. Ando, S. Kominami, K. Amemiya, and R. Ohno, *IEEE Trans. Nucl. Sci.*, **57**, Iss. 1: 395 (2010).
27. V. B. Molodkin, H. I. Nyzkova, V. V. Lizunov, V. V. Molodkin, S. V. Dmitriev, L. I. Makarenko, O. S. Kononenko, I. I. Demchyk, and N. P. Irkha, *Metallofiz. Noveishie Tekhnol.*, **40**, No. 9: 1133 (2018) (in Russian).
28. V. B. Molodkin, S. I. Olikhovskii, E. G. Len, Ye. M. Kyslovskyy, O. V. Reshetnyk, T. P. Vladimirova, B. V. Sheludchenko, E. S. Skakunova, V. V. Lizunov, E. V. Kochelab, I. M. Fodchuk, and V. P. Klad'ko, *Metallofiz. Noveishie Tekhnol.*, **38**, No. 1: 99 (2016).
29. V. V. Lizunov, V. B. Molodkin, S. I. Olikhovskiy, S. V. Lizunova, N. G. Tolmachev, A. I. Nizkova, E. S. Skakunova, S. V. Dmitriev, B. V. Sheludchenko, T. G. Sych, E. V. Fuzik, R. V. Lekhnyak, and L. N. Skapa,

Metallofiz. Noveishie Tekhnol., **37**, No. 2: 265 (2015) (in Russian).
30. V. V. Dovganyuk, I. M. Fodchuk, O. G. Gymchynsky, A. V. Oliynych-Lysyuk, Ye. M. Kyslovs'ky, A. O. Bilots'ka, T. P. Vladimirova, R. F. Seredenko, and Z. Swiantek, *Metallofiz. Noveishie Tekhnol.*, **28**, No. 10: 1291 (2006) (in Russian).

Metallophysics and Advanced Technologies
Металофіз. новітні технол.
Metallofiz. Noveishie Tekhnol.
2026, vol. 48, No. 5, pp. 463–481
https://doi.org/10.15407/mfint.48.05.0463
Reprints available directly from the publisher

PACS numbers: 61.05.cp, 61.66.Dk, 61.72.Dd, 61.72.Ff, 65.40.De, 81.20.Ev, 81.40.Ef

Influence of Annealing on the CTE of Sintered Al–Si–Ni and Al–TiC Materials

V. V. Kaverinskiy, G. A. Bagliuk, S. F. Kyryliuk, Z. P. Sukhenko, I. M. Kirian*, and O. D. Rud*

I. M. Frantsevych Institute for Problems in Materials Science, N.A.S. of Ukraine,
3 Omeljan Pritsak Str.,
UA-03142 Kyiv, Ukraine
**G. V. Kurdyumov Institute for Metal Physics, N.A.S. of Ukraine,*
36 Academician Vernadsky Blvd.,
UA-03142 Kyiv, Ukraine

This study investigates the effects of annealing and annealing temperature on the temperature-dependent coefficient of thermal expansion (CTE) for two advanced materials: sintered Al–Si–Ni alloy and Al–TiC composite with *in situ* synthesized carbide particles. The experiments reveal significant differences in the annealing impact on the CTE behaviour of these materials. For the Al–TiC composite, the CTE demonstrates an Arrhenius-type dependence on temperature, with annealing causing a consistent reduction in CTE across the studied temperature range. While the activation energy associated with the Arrhenius-type dependence remains unaffected largely, the pre-exponential factor is altered significantly, pointing to structural and microstructural transformations. XRD analysis confirms that increasing the annealing temperature decreases the crystallite size, particularly, in the carbide phase, that correlates with the observed CTE reduction. In contrast, the Al–Si–Ni alloy exhibits a more complex response to annealing. Annealing at 420°C increases slightly the CTE at higher measuring temperatures (> 100°C), while annealing at 550°C causes a notable rise in CTE at lower temperatures and leads to more stable, nearly linear temperature dependence.

Corresponding author: Oleksandr Dmytrovych Rud
E-mail: rud@imp.kiev.ua

Citation: V. V. Kaverinskiy, G. A. Bagliuk, S. F. Kyryliuk, Z. P. Sukhenko, I. M. Kirian, and O. D. Rud, Influence of Annealing on the CTE of Sintered Al–Si–Ni and Al–TiC Materials, *Metallofiz. Noveishie Tekhnol.*, **48**, No. 5: 463–481 (2026). DOI: 10.15407/mfint.48.05.0463

Crystallite size in the alloy increases with annealing, aligning with the observed rise in CTE. These findings highlight the critical role of microstructural changes induced by annealing in controlling the thermal-expansion properties of Al-based alloys. Understanding these mechanisms offers valuable insights for tailoring material performance in applications requiring precise thermal stability.

Key words: coefficient of thermal expansion, sintered aluminium alloys, aluminium-matrix composites, annealing, structure, crystallite size.

У дослідженні проаналізовано вплив температури відпалу на температурну залежність коефіцієнта термічного розширення (КТР) для двох сучасних матеріялів: спеченого стопу Al–Si–Ni та композиту Al–TiC з карбідними частинками, синтезованими *in situ*. Експерименти виявили значні відмінності у поведінці КТР цих матеріялів після відпалу. Для композиту Al–TiC КТР демонструє залежність від температури типу Арреніюсової, причому відпал спричиняє постійне пониження КТР у всьому дослідженому температурному діяпазоні. Хоча енергія активації, пов'язана із Арреніюсовою залежністю, залишається майже незмінною, значно змінюється передекспоненційний множник, що вказує на структурні та мікроструктурні трансформації. Аналіза за допомогою дифракції X-променів показала, що з підвищенням температури відпалу зменшується розмір кристалітів, особливо у карбідній фазі, що корелює зі спостережуваним пониженням КТР. Стоп Al–Si–Ni показав складнішу реакцію на відпал. Відпал за температури у 420°C незначно збільшив КТР за вищих температур міряння (> 100°C), тоді як відпал за 550°C спричинив помітне зростання КТР за нижчих температур і привів до стабільної, майже лінійної залежности КТР від температури. Розмір кристалітів у стопі збільшувався після відпалу, що узгоджується зі зростанням КТР. Ці результати підкреслюють ключову роль мікроструктурних змін, спричинених відпалом, у реґулюванні властивостей термічного розширення стопів на основі алюмінію. Розуміння цих механізмів дає змогу вдосконалювати матеріяли для застосувань, що потребують високої термічної стабільности.

Ключові слова: коефіцієнт теплового розширення, спечені алюмінійові стопи, алюмінійові матричні композити, відпал, структура, розмір кристалітів.

(Received 9 May, 2025; in final version, 15 October, 2025)

1. INTRODUCTION

The field of device construction, particularly for aerospace applications, necessitates lightweight materials with specific physical properties [1, 2]. One critical property is a coefficient of thermal expansion (CTE) compatible with materials such as steel and copper alloys. This compatibility is essential for orientation and navigation devices in flying objects, where dimensional instability can account for 20–50% of total device error [3]. Consequently, the development of lightweight

materials with low CTE values remains a pressing challenge in modern metallurgy and materials science.

Aluminium serves as the foundation for many lightweight materials due to its numerous advantages: low density (2700 kg/m^3), high corrosion resistance, excellent plasticity, affordability, non-toxicity, and ease of processing [4]. These properties often surpass those of other lightweight metals like magnesium, beryllium, or lithium. However, aluminium high linear thermal-expansion coefficient ($23.4 \cdot 10^{-6}\ K^{-1}$ in the 20–100°C range) [5] presents a significant drawback compared to materials like steel ($\cong 10–15 \cdot 10^{-6}\ K^{-1}$) [6] and copper ($16.8 \cdot 10^{-6}\ K^{-1}$) [7]. Therefore, reducing aluminium CTE through specialized alloying is crucial for its application in precision instrument making.

The Al–Si–Ni alloys, which contain 25–30% wt. silicon and 5–7% wt. nickel, exhibit CTE values comparable to steel. However, manufacturing homogenous Al–Si–Ni alloys with appropriate structures and properties poses significant challenges due to their broad solidification temperature range [8]. For example, an alloy with 30% wt. silicon and 7% wt. nickel has a liquidus temperature of ≅ 850°C and a solidus temperature of 557°C, as illustrated in Ref. [8]. During this interval, silicon and intermetallic compounds, known for their brittleness, tend to grow within the liquid phase, leading to phase segregation due to the difference in density. As a result, casting is unsuitable for these alloys, and production typically relies on powder metallurgy. This method involves pre-alloyed powders produced through rapid solidification, followed by solid-phase sintering and hot deformation processing [9]. Only this approach ensures a homogenous structure with fine silicon and Al_3Ni inclusions and acceptable mechanical properties [10].

As an alternative to Al–Si–Ni alloys, aluminium matrix composites (AMCs) are gaining attention. AMCs reinforced with ceramic particles exhibit superior strength, elastic modulus, and resistance to creep and fatigue compared to unreinforced aluminium. These properties make them highly attractive for the aerospace and automotive industries. In addition to improved strength, AMCs demonstrate enhanced hardness and wear resistance. Commonly used reinforcements include SiC, Al_2O_3, TiC, and TiB_2 [11–16]. Among these, Al–TiC composites stand out due to their excellent wear resistance, high strength-to-weight ratio, and mechanical properties. Moreover, the lattice parameters of TiC particles closely match those of solid aluminium, making them effective nucleation centres during the alloy crystallization [17, 18].

Several techniques are available for making particle-reinforced metal matrix composites (MMCs), ranging from casting [19, 20] to powder metallurgy (PM) methods [17, 20]. The segregation of reinforcement during solidification limits the performance of cast-route composites in various applications. Inhomogeneous distributions of the reinforcement have been widely reported to deteriorate mechanical

properties, particularly fatigue and fracture performance [19].

Al–TiC composites hold a key position among materials with low coefficients of thermal expansion, particularly for use in high-precision equipment and electronics. These composites are notable not only for their reduced CTE but also for their enhanced strength and hardness. Titanium carbide (TiC) forms exceptionally strong bonds with the aluminium matrix, making these materials resistant to mechanical deformation, even at elevated temperatures [21]. The presence of TiC particles limits the thermal expansion of the aluminium matrix while contributing to improved heat resistance. However, this comes at the expense of reduced plasticity, as the rigid TiC particles restrict the matrix's ability to deform under stress. Thanks to their high-temperature stability, Al–TiC composites are particularly suitable for demanding applications such as engine components and heat dissipation systems, where performance under high loads is critical.

The most common method for producing Al–TiC composites is powder metallurgy, which ensures a uniform distribution of TiC particles within the aluminium matrix. This process typically involves mixing aluminium and titanium carbide powders, followed by pressing and sintering in a vacuum or an inert gas environment, such as argon. Compared to traditional casting, powder metallurgy offers significant advantages, including minimized chemical reactions between the aluminium matrix and TiC reinforcement, as the synthesis occurs at lower temperatures [18]. However, a challenge with this approach is the poor wettability of titanium carbide particles by aluminium, often caused by oxide films on the TiC surface. This issue can limit the potential benefits of carbide reinforcement [22].

To overcome this limitation, alternative technologies have been developed, including the use of Al–Ti–C master alloys. These master alloys are created *via in situ* reactions in a mixture of elemental aluminium, titanium, and carbon powders, resulting in the formation of finely dispersed TiC particles within the aluminium matrix. This process occurs at relatively moderate temperatures (900–1000°C) [22–26], producing composites with improved properties.

One of the most promising techniques is *in situ* thermal synthesis, which ensures the formation of submicron-sized, spherical TiC particles that are well integrated into the aluminium matrix [27–29]. This method can avoid undesirable structural components formation, such as ternary carbides (MAX phases), intermetallics, or unreacted carbon residues. Figure 1 shows an isothermal section of the Al–Ti–C phase diagram at 900°C, calculated using the CALPHAD method [30, 31]. In this diagram, the marked narrow two-phase region that represents the Al–TiC equilibrium seems to be an ideal for thermal *in situ* synthesis of Al–TiC composites.

Studies [27, 28] have demonstrated that, when the aluminium con-

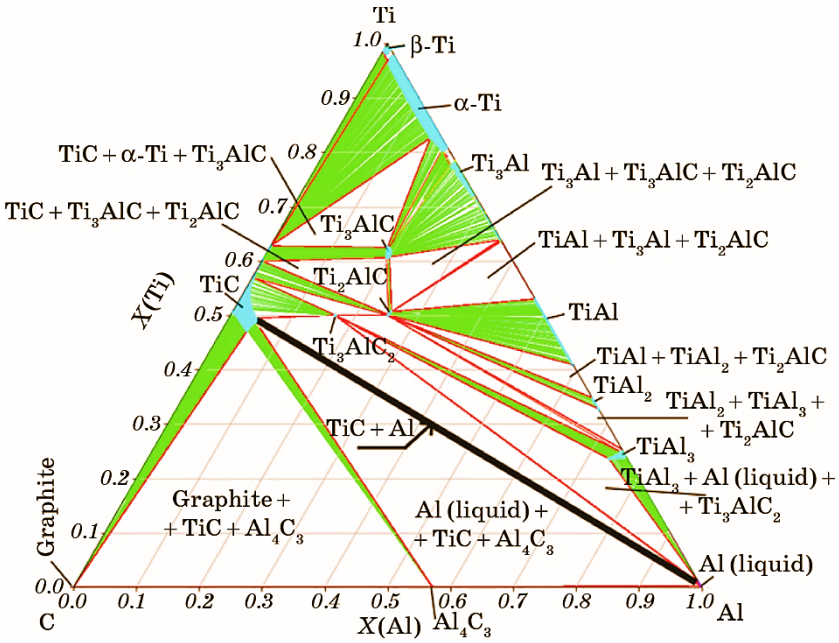

Fig. 1. Isothermal section of the calculated phase diagram of Al–Ti–C for 900°C [30].

tent exceeds 45%, the resulting TiC particles have roundish polyhedral submicron-sized shape, as shown in the micrograph in Fig. 2. These particles enhance the composite overall properties, making Al–TiC an ideal material for advanced applications.

Increasing the volume of carbides in the aluminium matrix is an effective way to lower the composite coefficient of thermal expansion. However, higher carbide content tends to increase porosity, which can adversely affect the composite mechanical properties [32]. In Al–TiC composites, the typical content of titanium carbide particles is limited to 10–15%. Beyond this range, the material plasticity decreases significantly, and its machinability becomes more challenging [33].

One promising solution to this issue is the application of additional hot stamping processes. This technique has been shown to reduce porosity, even at higher carbide concentrations, enabling the production of composites with exceptionally low CTE values (comparable to steel), while still retaining acceptable mechanical properties [28].

Despite significant advancements in the production and application of Al–TiC composites, their thermal expansion behaviour remains insufficiently studied. This is particularly true for their response to long-term high-temperature exposure, such as annealing. Similarly, for both Al–Si–Ni and Al–TiC composites, there is a lack of detailed

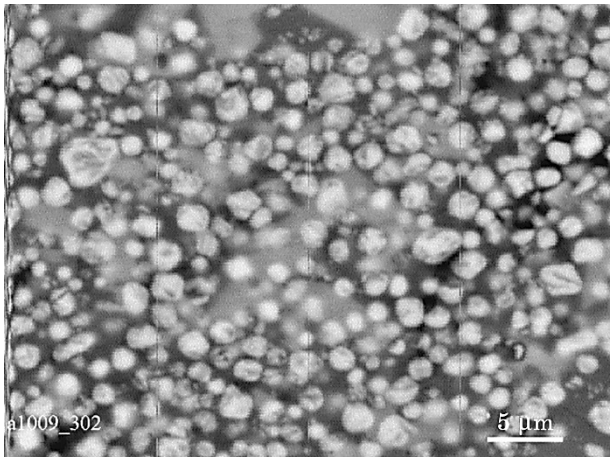

Fig. 2. Typical SEM image of the structure of *in situ* synthesized Al–TiC composite (45% Al) [27].

information regarding the impact of annealing on CTE values and how these values vary with temperature.

The present investigation aims to address this gap by exploring the relationship between annealing temperature and the CTE of these composites. This study seeks to provide new insights into the temperature-dependent behaviour of Al–TiC and Al–Si–Ni composites.

2. MATERIALS AND METHODS

The materials investigated in this study were an Al–Si–Ni sintered alloy and an Al–TiC composite, with their compositions summarized in Table 1.

Since the prior studies revealed that the Al–Si–Ni alloy production through merely mixing the does not achieve the desired mechanical properties and leads to a coarse structure even after hot stamping, prealloyed powder has been used [9]. The Al–Si–Ni alloy was prepared

TABLE 1. Compositions of the studied materials (% wt.). The composition of Al–TiC composite reflects the mass proportions of the initial materials for synthesis, corresponding to approximately 55% TiC by weight.

Al–Si–Ni sintered alloy	Al	Si	Ni
	65.8	28.5	5.7
Al–TiC composite	Al	Ti	C
	45	44	11

from powder of ground rapidly solidified ribbons produced using the melt-spinning technique. The ribbons with a thickness of 30–50 μm and a width of 9–12 mm were fabricated by casting molten material onto a rotating copper reel under controlled conditions, including a melt temperature of 1080°C, precise crucible pressure, and drum rotation speed. The process was conducted under a protective helium atmosphere using quartz crucibles at the G. V. Kurdyumov Institute for Metal Physics, N.A.S. of Ukraine [10].

The ribbons were mechanically ground in a Fritsch Pulverisette P-6 planetary ball mill to produce alloy powder. Grinding parameters included a rotation speed of 200 rpm, a ball-to-powder mass ratio of 10:1, and a grinding duration of 30 minutes with 12 steel balls (20 mm diameter) and approximately 37 g of powder. The resulting powder had an average particle size of 106 ± 5 μm, with particle sizes ranging from 4 to 381 μm.

Compaction of the Al–Si–Ni powders was achieved using a hydraulic press at pressures of 500–600 MPa. The powders were compacted into low-carbon steel capsules with external and internal diameters of 28 mm and 32 mm, respectively, and a total height of 37 mm (including the base and lid). These capsules optimized the deformation process and ensured uniform compression. Sintering was performed at 530°C for 2 hours, preceded by degassing at 350°C for 30 minutes. This temperature was selected to remain below the ternary eutectic point (540–550°C) for rapidly solidified materials with non-equilibrium phases, as noted in Ref. [3]. Solid-phase sintering was employed to prevent liquid-phase formation, which could lead to porosity and chemical distortion, as observed in earlier studies [10].

Hot deformation (forging) of the sintered samples was conducted at 520°C in a specially designed die. Before forging, the samples underwent additional lateral compression (20–30%) at the same temperature. After forging, the steel shells were removed by machining. The final samples exhibited no brittle fractures and were suitable for further processing.

Thermal synthesis of the Al–TiC master alloy followed the procedures detailed in Refs. [23, 27, 28]. Initial aluminium, titanium and carbon (graphite) powders mixtures has been blended in a barrel mixer with alcohol, pressed into briquettes at 500 MPa using a hydraulic press (GP60), and sintered in an argon-filled sealed chamber at 950°C using indirect induction heating. The sintered briquettes (spongy and porous because of TiC synthesis reaction) were subsequently crushed in a planetary mill for 5–15 minutes to achieve the desired particle size, with sieving used to ensure a maximum particle size of 10 μm. The obtained particles were polycrystalline aggregates of TiC crystals in aluminium matrix. The obtained powder was then pressed at 550 MPa into blanks measuring 40 mm in diameter and 12 mm in height. These

blanks were sintered in argon at 600°C for 1 hour and then subjected to hot stamping in a semi-closed die on an arc-stator press.

Post-stamping annealing was performed in a laboratory muffle furnace (SNOL 7.2/1300, ThermoLab) at 400°C, 500°C, and 600°C for the Al–TiC composite and at 420°C and 550°C for the Al–Si–Ni system material samples. The duration of the annealing for each case was 2 hours. Dilatometric measurements were carried out using a dilatometer with an inductive transducer. The error of CTE estimation on the final experimental curves was $\pm 0.3 \cdot 10^{-6}\,K^{-1}$. Microstructural analysis was conducted using an optical microscope (BH200M-RT) with digital micrographs captured using a SIGETA M3CMOS 32000 camera. The x-ray diffraction (XRD) study of the materials was carried out on a DRON-4 diffractometer with radiation MoK_α.

3. RESULTS AND DISCUSSION

3.1. Coefficient of Thermal-Extension Temperature Dependence

3.1.1. CTE of Sintered Al–Si–Ni Alloy

Figure 3 presents the temperature dependence of the studied Al–Si–Ni alloy CTE in temperature range of 50–300°C in its initial and annealed states. The studied samples were in the initial state and annealed at 420 and 550°C. From the provided plots, we can see that the CTE values of Al–Si–Ni alloy significantly increase with the temperature. For instance, in the initial state at 50°C its value is the lowest observed at

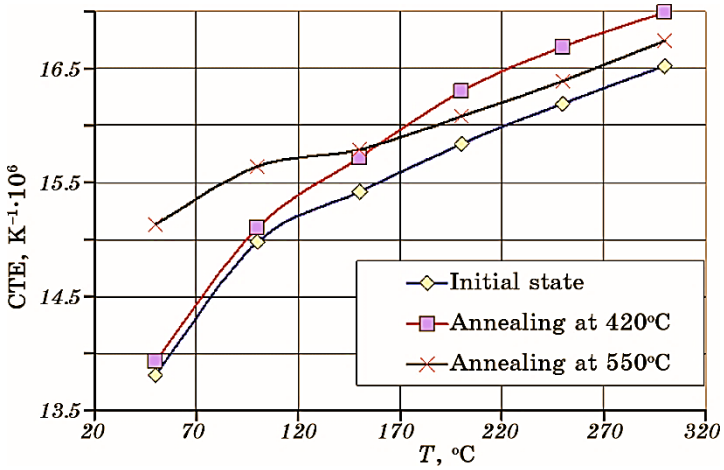

Fig. 3. Influence of annealing on the sintered Al–Si–Ni-alloy CTE temperature dependence.

$13.8 \cdot 10^{-6}\ K^{-1}$. However, at 300°C it rises to $16.5 \cdot 10^{-6}\ K^{-1}$. The growth is not linear, especially for not annealed and annealed at 420°C samples. A significant jump is observed in the range of 50–100°C.

Annealing at 420°C almost does not affect the material CTE at lower temperatures. The observed difference in the range of 50–150°C is comparable with the measurement accuracy. At higher temperatures, some slight but notable ($\cong 0.5 \cdot 10^{-6}\ K^{-1}$) increase of CTE for the annealed at 420°C specimen is observed. Annealing at 550°C leads to more significant growth of CTE at lower temperatures: for 50°C, the difference is of $1.3 \cdot 10^{-6}\ K^{-1}$, and for 100°C, it is of $0.66 \cdot 10^{-6}\ K^{-1}$. However, at temperatures higher than 200°C, the difference becomes insignificant and close to the measurement inaccuracy. It could be seen that, after annealing at 550°C, CTE of the material appears more stable—the mentioned jump at 50–100°C disappeared and its temperature dependence becomes almost linear and less pronounced.

Regarding the nature of the effect of annealing on the CTE, it can be assumed that annealing somehow affects the redistribution of the final mechanical stresses between the matrix and the silicon and intermetallic particles. Annealing can stabilize finely dispersed, in particular intermetallic, particles and prevent their agglomeration. When the particles remain evenly distributed and are not prone to coalescence, this contributes to an increase in the density of interphase boundaries, since each particle forms its boundary with the matrix. Annealing helps to eliminate residual stresses accumulated during the deformation of the composite. This relaxation contributes to the redistribution of particles at the microstructural level, where strong adhesion between the phases creates additional interphase boundaries.

3.1.2. CTE of Al–TiC Composite

The CTE temperature dependence of the Al–TiC composite was studied for the cases of annealing temperatures of 400, 500 and 600°C. CTE of the non-annealed samples has not been studied. The temperature dependencies of CTE values for the studied annealing temperatures are presented in Fig. 4.

From the presented results, it is evident that the CTE of the Al–TiC composite under consideration increases noticeably with a rise in temperature. Unlike the Al–Si–Ni system, annealing in this case significantly reduces the CTE. Furthermore, the observed reduction is relatively uniform across all temperatures. Increasing the annealing temperature further decreases the CTE.

The supposed reasons of the observed effect might be related to the relaxation of residual stress, dislocation density, changes in the morphology of particles or crystallite size caused by the annealing. Annealing, particularly, at higher temperatures, may lead to the redistribu-

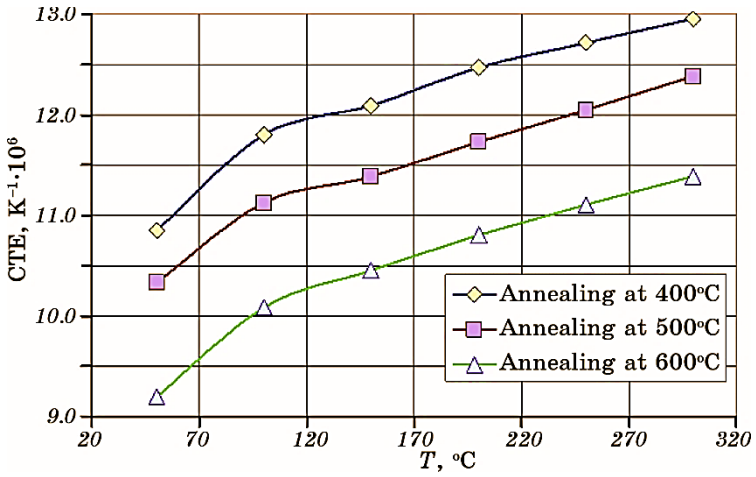

Fig. 4. Influence of annealing on the Al–TiC composite CTE temperature dependence.

tion of TiC particles within the matrix or changes in the density of interphase boundaries.

3.2. Microstructure of Composites

3.2.1. Sintered Al–Si–Ni Alloy

Microstructure photos of the initial and annealed material's samples are shown in Fig. 5. There is no notable difference in the material microstructure depending on the annealing temperature. In both presented cases are observed small almost eventually distributed silicon and intermetallic inclusions in the aluminium matrix. The shape of the inclusion is close to equiaxed polyhedra. The numerical characteristics of the microstructure are presented in Table 2, which includes average sizes of silicone and intermetallic inclusions and a number of all types

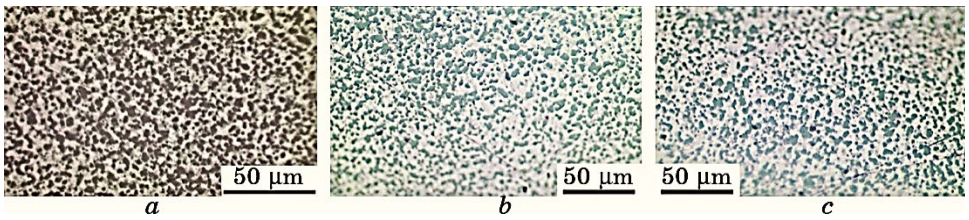

Fig. 5. Microstructure of the sintered Al–Si–Ni alloy after forging (*a*) and annealing at 420°C (*b*) and 550°C (*c*).

TABLE 2. Quantitative characteristics of the sintered Al–Si–Ni-alloy microstructure after different annealing temperatures.

Annealing temperature, °C	Average inclusions sizes, μm		Total number of the inclusions per 1 mm^2, $\times 10^4$
	Si	Al_3Ni	
Initial state	2.57 ± 0.13	1.43 ± 0.10	5.42 ± 0.86
420	2.77 ± 0.12	1.80 ± 0.07	4.05 ± 0.30
550	2.81 ± 0.09	1.82 ± 0.10	3.68 ± 0.20

of inclusions per 1 mm^2.

As can be seen in Table 2, some growth of the average inclusion sizes (both for silicon and for Al_3Ni) is observed after annealing at 420°C compared with the initial state. However, the difference in the measured values of the samples annealed at 420°C and 550°C is very slight and insignificant. Nevertheless, the difference between the number of inclusions per 1 mm^2, which seems to be a more reliable and precisely measured parameter, is rather different for all three studied cases. There is a decrease of this number after annealing and with razing its temperature. This may indicate some growth of the particles, gradual vanishing of the smallest ones, and growth in the distance between the inclusions. This seems to be a typical case of Ostwald's ripening, which accelerates with the temperature increasing.

Despite there being no direct evidence that the observed ripening of the inclusions when annealing effects directly the CTE of the material, it can be declared that those phenomena accompany each other, in this case—the particles ripen and CTE values increase when annealing and temperature growth.

3.2.2. Al–TiC Composite

Typical microstructure images (optical metallography) after annealing at different temperatures are shown in Fig. 6. The images demonstrate that the structure does not undergo radical changes under the influence of different annealing temperatures. Nevertheless, careful quantitative evaluation allows for the identification of even minor shifts in the structure.

The quantitative characteristics of the microstructure are presented in Table 3. The following parameters have been measured: the size of TiC particles (measured at ×500 magnification), the thickness of carbide cluster layers (measured at ×200 magnification), and the porosity estimation (carried out at ×50 magnification).

The measurement data indicate that the annealing temperature has almost no effect on the size of titanium carbide particles. The differ-

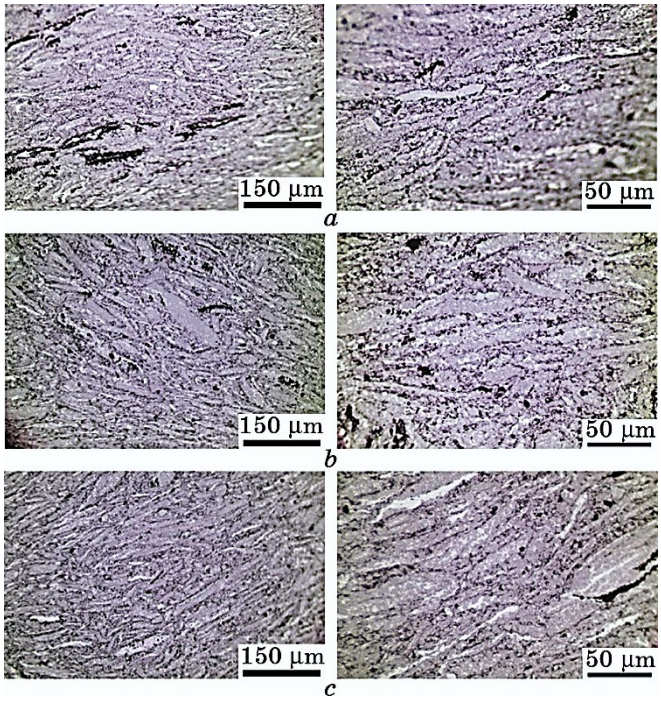

Fig. 6. Microstructure of the Al–TiC composite after stamping and annealing at following temperatures: 400°C (*a*), 500°C (*b*), 600°C (*c*).

TABLE 3. Quantitative characteristics of the Al–TiC-composite microstructure after different annealing temperatures.

Annealing temperature, °C	TiC particles average size, μm	Thickness of carbide cluster layers, μm	Porosity estimation, %
400	2.18 ± 0.11	7.83 ± 0.36	7.8 ± 1.4
500	2.33 ± 0.07	9.84 ± 0.37	4.6 ± 1.5
600	2.40 ± 0.08	11.96 ± 0.44	3.1 ± 0.9

ence in average values lies within the margin of statistical error. The size distribution of the particles follows a lognormal pattern, with no significant differences observed in the nature of the distribution.

The thickness of the carbide cluster layers observed in the structure changes only slightly with annealing temperature. A visual inspection of the microstructures reveals that in annealed at lower temperature samples, the carbide particles are more aggregated into clusters. With increasing annealing temperature, the particles become somewhat more separated, and more distinct matrix layers appear between them. It was also ob-

served that annealing reduces porosity in the material. Anyway, the influence of the annealing on the microstructure seems to be very slight.

3.3. X-Ray Diffraction Analysis

3.3.1. Sintered Al–Si–Ni Alloy

Observed by means of optical microscopy structural changes could only practically explain the possible reasons for CTE changes after a long-term thermal impact such as annealing. The x-ray diffraction (XRD) analysis is able to reveal more fine structure factors, among which are crystallite sizes and lattice parameters of the phases. An example of an XRD pattern for the studied material—a case of annealing at 420°C—is shown in Fig. 7. The present phases are typical and expected for the material, which are aluminium solid solution—the matrix, silicon and intermetallic compound Al_3Ni. The phase composition is qualitatively and quantitatively identical in each of the studied samples and is not affected by the annealing. Nevertheless, the XRD analysis reveals also the crystallite sizes and lattice parameters of the phases, as has been mentioned above. These results are presented in Table 4.

The given results show that this does not affect the lattice parameters of any phase presented in the material. However, there is a significant influence on the crystallite size both for matrix and for inclusions. The crystallite size of the aluminium matrix grew about 1.3 times after annealing at 420°C and more than 1.3 extra with the rise of the annealing to 550°C. Even more significant grows the crystallite size of silicon. For the Al_3Ni inclusions, however, only annealing at 550°C can af-

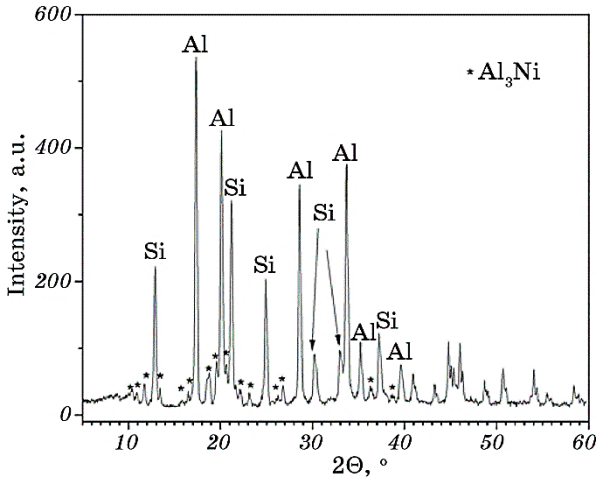

Fig. 7. Typical XRD pattern for the studied sintered Al–Si–Ni alloy.

TABLE 4. Effect of annealing temperature on the fine-structure characteristics of the phases present in the sintered Al–Si–Ni alloy according to XRD analysis.

Annealing temperature, °C	Phase	Lattice parameters, Å			Crystallite size, Å
		a	*b*	*c*	
Not annealed	Al	4.053	–	–	660
	Si	5.443	–	–	700
	Al_3Ni	6.602	7.382	4.811	450
420	Al	4.057	–	–	865
	Si	5.448	–	–	1150
	Al_3Ni	6.620	7.378	4.817	430
550	Al	4.059	–	–	1180
	Si	5.440	–	–	1800
	Al_3Ni	6.619	7.388	4.822	990

fect significantly its crystallite size, which increases more than twice.

Thus, for the studies here sintered Al–Si–Ni alloy annealing leads to both Ostwald ripening of the inclusions and growth of the crystallite size of matrix and inclusions. Moreover, the crystallite size of Al_3Ni starts to grow only at high annealing temperatures close to the solidus temperature. The observed structural changes could result in the mentioned CTE changes. It might be assumed that the Al_3Ni crystallite size increase, which appears at 550°C annealing, could be the reason for observed CTE rising at lower measuring temperatures. Moreover, it might be the phase most responsible for the annealing dependence of CTE for the material. The matrix and the silicon inclusions (their crystallite growth and ripening) could be responsible for more subtle changes in CTE temperature behaviour, which are the increase of CTE at higher temperatures after annealing at 420°C and its relative stabilization at the whole temperature range after annealing at 550°C.

3.3.2. Al–TiC Composite

The carried-out x-ray phase analysis has not shown any significant difference in the phase composition of the studied samples annealed at different temperatures. As you can see in the XRD pattern in Fig. 8, the only observed phases in the material are Al-based solid solution and TiC. The estimated part of TiC was about 55% wt.

The XRD also provides information on the lattice parameters and crystallite sizes for each of the present phases. The obtained results are presented in Table 5. In the XRD study, it was analysed as not annealed

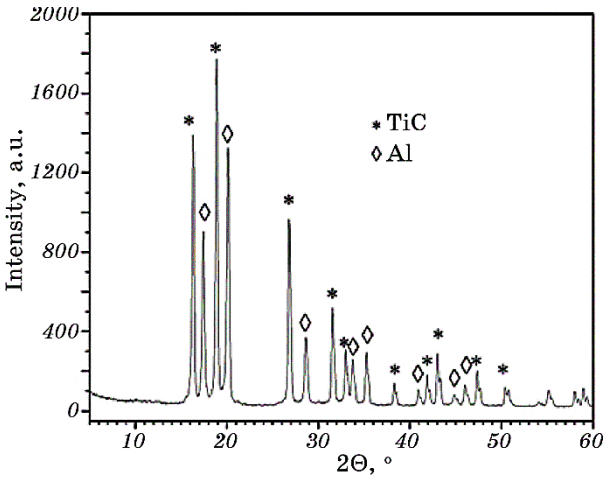

Fig. 8. XRD pattern for the studied Al–TiC composite.

TABLE 5. Effect of annealing temperature on the fine-structure characteristics of the phases present in the Al–TiC composite according to XRD analysis.

Annealing temperature, °C	Phase	Lattice parameter, Å	Crystallite size, Å
Not annealed	Al	4.0548	511
	TiC	4.3255	940
500	Al	4.0597	414
	TiC	4.3272	533
600	Al	4.0581	310
	TiC	4.3284	480

instead of annealed at 400°C. Others were the same.

We can see that annealing does not have any effect on the lattice parameters of any phase. However, the impact on the crystallite sizes is rather more valuable. It is notable that the annealing and its temperature rising lead not to growth but to a significant decrease of the crystallite sizes both for Al-based solid solution and for TiC. The annealing almost twice reduces its value for TiC. Rising annealing temperature from 500°C to 600°C has an additional 10% effect on the crystallite size of TiC declining.

Thus, for the studied material we observe that the CTE decreasing with the annealing temperature growth is clearly accompanied by the crystallite sizes decreasing both for the metal matrix and for the carbides. The observed relationship between decreasing CTE and reduced crystallite sizes is a realistic outcome of annealing. It might highlight

the complex interplay between microstructure evolution, defect dynamics, and interfacial phenomena in determining the thermal properties of a material.

3.4. Discussion

The relationship between annealing temperature, grain size, and the coefficient of thermal expansion in MMC is known and a well-documented phenomenon in materials science for different materials. Generally, as the grain size decreases, the CTE tends to increase due to the enhanced contribution of grain boundaries, which have different thermal expansion behaviours compared to the grain interiors. For example, in work [34], they studied the effects of grain size on the thermal expansion behaviour of the Fe–Ni invar alloy. The results showed a possibility of achieving different thermal expansion coefficients over a wide range of $(3.1–7.8)\cdot10^{-6}\ K^{-1}$ for the same alloy through grain size control. The thermal expansion difference between grain boundaries and crystallites was enlarged in the invar alloy.

However, in certain MMCs, increasing the annealing temperature can lead to a reduction in CTE. This effect is often attributed to the relaxation of residual stresses and changes in the microstructure, such as the redistribution of reinforcing particles like carbides within the metal matrix. For instance, in aluminium matrix composites reinforced with silicon carbide SiC and other particles, heat treatment has been shown to influence mechanical properties and thermal expansion [35]. Specifically, the CTE after treatment without reinforcement applied was reduced, while no significant difference was seen with reinforcement applied.

Additionally, the presence of reinforcing particles with a lower CTE than the metal matrix can lead to a mismatch in thermal expansion, inducing internal stresses that affect the overall CTE of the composite. The distribution and morphology of these particles, influenced by annealing, play a crucial role in determining the composite's thermal expansion behaviour [36].

The study [37] declares that, despite the known fact that the CTEs of alloys and composites are mainly changed by a volume fraction and shape of the second phases [38, 39], the CTE of particle-reinforced MMCs is affected by several other factors. These include: plasticity due to CTE mismatch between reinforcement and matrix, during heating or cooling; reinforcement fracture, residual stress, and local stresses at points of contact between reinforcement [40]. An incompressible plastic layer may form at the particle/matrix interface, and result in a lower expansion of the matrix, and thus, the overall composite [41]. The CTE of the composite is generally less than the rule of mixtures value because the presence of ceramic particles (usually of

low CTE) introduces a constraint on the expansion of the metallic matrix (usually of high CTE). In this regard, it is important to point out that interface can exert some influence on the value of CTE, especially, for very small particle sizes.

Thus, the observed here influence of annealing and its temperature on the Al-based MMCs' CTE and its relationship with the crystallite sizes does not contradict general concepts for such composites. Moreover, the obtained results significantly complement the insight into the thermal dependence of sintered Al–Si–Ni and Al–TiC materials CTE and the annealing effect on it observed at different temperature ranges.

It was shown that annealing could either increase or decrease the crystallite size, but lower crystallite size for the studied here composites often means the lower values of CTE. In the sintered Al–Si–Ni alloy, annealing and raising its temperatures results in crystallite size increasing and inclusions ripening that leads to CTE increase. A key role in this phenomenon can be played by Al_3Ni particles, the crystallite growth of which after high-temperature annealing can lead to an increase in the CTE at lower temperatures and its relative stabilization. On the other hand, the Al–TiC shows the contrary reaction on annealing—its crystallite decrease, which may lead to the observed CTE lowering.

4. CONCLUSIONS

An experimental investigation was carried out to study the influence of annealing and its temperature on the temperature dependence of the coefficient of thermal expansion for sintered Al–Si–Ni alloy and Al–TiC composite material containing *in situ* synthesized carbide particles.

The CTE of both materials increases with rising temperature. However, the effect of annealing on the sintered Al–Si–Ni alloy CTE differs from that observed in the Al–TiC composite. Annealing at a lower temperature (420°C) slightly increases the CTE at higher (> 100°C) measuring temperatures. In contrast, annealing near the solidus temperature (550°C) significantly raises the CTE at lower measuring temperatures, makes it more stable, and results in nearly linear temperature dependence.

Changes in CTE following annealing are accompanied by structural modulations. Notably, variations in crystallite size, determined through XRD analysis, were observed. A decrease in crystallite size correlates with a reduction in CTE for both materials. However, annealing affected crystallite size differently in the studied materials: in the sintered Al–Si–Ni alloy, annealing and increased temperature led to larger crystallites, whereas in the Al–TiC composite, higher annealing temperatures caused a reduction in crystallite size, particularly in the carbide phase. These differences in the effects of annealing on crystallite size are likely contributing factors to the contrasting CTE

behaviours of the two materials.

REFERENCES

1. O. E. Osintsev, *Met. Sci. Heat Treat.*, **40**: 172 (1998) (in Russian).
2. Z. Ahmad, *Aluminium Alloys: New Trends in Fabrication and Applications* (IntechOpen: 2012).
3. V. V. Vasenyev, *Razrabotka Kompozitsionnogo Materiala na Osnove Sistemy Al–Si–Ni s Nizkim Koeffitsientom Lineynogo Rasshireniya i Tekhnologii Izgotovleniya Izdeliya Raketno-Kosmicheskoy Tekhniki* [Development of a Composite Material Based on the Al–Si–Ni System with a Low Coefficient of Linear Expansion and Manufacturing Technology for Rocket and Space Equipment] (Thesis of Disser. for Dr. Techn. Sci.) (Moskva: 2017) (in Russian).
4. E. L. Rooy, *Introduction to Aluminum and Aluminum Alloys* (ASM International: 1990).
5. O. E. Osintsev and S. L. Nikitin, *Vysokoprochnyye Korrozionnostoykie Liteynyye Alyuminievyye Splavy Sistemy Al–Mg s Povyshennym Soderzhaniem Kremniya* [High-Strength, Corrosion-Resistant, Cast Aluminium Alloys of the Al–Mg System with Increased Silicon Content] (Moskva: MATI: 2008) (in Russian).
6. *Temperature Coefficient of Linear Expansion of Steel*
7. G. V. Samsonov, *Handbook of the Physicochemical Properties of the Elements* (Springer: 1968).
8. T. Bedo, B. Varga, D. Cristea, A. Nitoi, A. Gatto, E. Bassoli, G. Bulai, I.-L. Velicu, I. Ghiuta, S. Munteanu, M. A. Pop, C. Gabor, M. Cosnita, L. Parv, and D. Munteanu, *Metals*, **9**, Iss. 5: 483 (2019).
9. V. V. Kaverinsky, G. A. Bagliuk, S. F. Kyrylyuk, D. G. Verbylo, Z. P. Sukhenko, I. M. Kirian, M. A. Skoryk, and O. D. Rud, *Metallofiz. Noveishie Tekhnol.*, **47**, No. 3: 257 (2025).
10. G. A. Bagliuk, T. O. Monastyrska, V. V. Kaverinsky, V. P. Bevz, V. K. Nosenko, I. M. Kirian, D. L. Pakula, V. V. Kyrylchuk, A. M. Lakhnik, and O. D. Rud, *Metallofiz. Noveishie Tekhnol.*, **45**, No. 8: 951 (2023).
11. J. M. Torralba, C. E. da Costa, and F. Velasco, *J. Mater. Process. Technol.*, **133**: 203 (2003).
12. O. Beffort, S. Long, C. Cayron, J. Kuebler, and P.-A. Buffat, *Composites Sci. Technol.*, **67**, Iss. 3–4: 737 (2007).
13. I. Topcu, H. O. Gulsoy, N. Kadioglu, and A. N. Gulluoglu, *J. Alloys Compd.*, **482**: 516 (2009).
14. K. M. Shorowordi, T. Laoui, A. S. M. A. Haseeb, J. P. Celis, and L. Froyen, *J. Mater. Process. Technol.*, **142**, Iss. 3: 738 (2003).
15. J. C. Viala, M. Peronnet, F. Bosselet, and J. Bouix, *Proc. Int. Conf. Compos. Mater. (ICCM-12) (July 5–9, 1999, Paris)*.
16. P. Lü, X. Yue, H. Ru, and L. Yu, *Rare Metals*, **29**: 92 (2010).
17. X. C. Tong and A. K. Ghosh, *J. Mater. Sci.*, **36**: 4059 (2001).
18. S. Mohapatra, A. K. Chaubey, D. K. Mishra, and S. K. Singh, *J. Mater. Research Technol.*, **5**, Iss. 2: 117 (2016).
19. R. S. Rana, P. Rajesh, and S. Das, *Int. J. Sci. Eng. Res.*, **3**, No. 6: 1 (2012).
20. M. O. Shabani and A. Mazahery, *Ceram. Int.*, **39**, Iss. 2: 1351 (2013).

21. A. Onat, H. Akbulut, and F. Yilmaz, *J. Alloys Compd.*, **436**: 375 (2007).
22. C. Selcuk and A. R. Kennedy, *Mater. Lett.*, **60**: 3364 (2006).
23. Y. A. Shishkina, G. A. Bagliuk, A. A. Mamonova, and I. B. Tikhonova, *Powder Metall. Met. Ceram.*, **52**: 154 (2013).
24. M. S. Song, B. Huang, M. X. Zhang, and J. G. Li, *Int. J. Refractory Metals Hard Mater.*, **27**, Iss. 3: 584 (2009).
25. Q. C. Jiang, H. Y. Wang, Y. G. Zhao, and X. L. Li, *Mater. Res.*, **40**: 521 (2005).
26. X. Zhang, X. Zeng, S. Zeng, and Q. Li, *Trans. Nonferrous Met. Soc. China*, **6**: 114 (1996).
27. Y. A. Shishkina, G. A. Bagliuk, A. A. Mamonova, M. E. Holovkova, and Y. B. Tykhonova, *Ceram.: Sci. Life*, **31**, No. 2: 52 (2016) (in Ukrainian).
28. Y. O. Shishkina, G. A. Bagliuk, Y. S. Kyryliuk, S. F. Kyryliuk, O. V. Tolochyna, and V. M. Talash, *Mater. Sci.*, **59**: 679 (2024).
29. S. Purush and M. J. Koczak, *Mater. Sci. Eng. A*, **144**: 37 (1991).
30. V. V. Kaverinsky, G. A. Bagliuk, and Z. P. Sukhenko, *J. Mater. Eng. Perform.*, **33**: 9976 (2024).
31. *PyCALPHAD: Computational Thermodynamics*
32. M. N. Arif, M. Bukhari, D. Brabazon, and M. Hashmi, *IOP Conf. Ser.: Mater. Sci. Eng.*, **701**: 012057 (2019).
33. B. Harris, *Engineering Composite Materials* (London: The Institute of Materials: 1999).
34. Y. Liu, L. Liu, Z. Wu, J. Li, B. Shen, and W. Hu, *Scripta Mater.*, **63**, Iss. 4: 359 (2010).
35. K. Chattrakul, N. Sornsuwit, and P. Muangnoy, *Processes*, **12**: 2464 (2024).
36. O. Matvienko, O. Daneyko, T. Kovalevskaya, A. Khrustalyov, I. Zhukov, and A. Vorozhtsov, *Metals*, **11**, Iss. 2: 279 (2021).
37. B. Karthikeyan, S. Ramanathan, and V. Ramakrishnan, *Adv. Mater. Research*, **264–265**: 663 (2011).
38. S. J. Feltham, B. Yates, and R. J. Martin, *Mater. Sci.*, **17**: 2309 (1982).
39. C.-S. Park, C.-H. Kim, M.-H. Kim, and C. Lee, *Mater. Chem. Phys.*, **88**: 46 (2004).
40. N. Chawla and K. K. Chawla, *Metal Matrix Composites* (New York: Springer: 2006).
41. V. Ramakrishnan, A. Ramasamy, P. P. Gupta, and H. Murthy Narayana, *Proc. 16th National. Heat Mass Transf. Conf.* (Calcutta: 2002), p. 216.

Metallophysics and Advanced Technologies
Металофіз. новітні технол.
Metallofiz. Noveishie Tekhnol.
2026, vol. 48, No. 5, pp. 483–493
https://doi.org/10.15407/mfint.48.05.0483
Reprints available directly from the publisher

PACS numbers: 61.72.Ff, 61.72.Mm, 64.75.Nx, 68.37.Hk, 68.37.Lp, 81.30.Mh, 82.80.Yc

The Effect of Hot Deformation in the α and α + β Phase Fields on the Microstructure and Precipitate Evolution of the Zr–Sn–Nb–Fe Alloy

A. W. Aldeen, D. Y. Mahdi, and M. S. Tuma

Department of Materials Engineering,
College of Engineering, University of Kufa,
Najaf, Iraq

The microstructure and precipitates' evolution after hot deformation of Zr–Sn–Nb–Fe samples in the α and α + β phases are investigated using transmission electron microscopy (TEM), energy dispersive x-ray spectroscopy (EDS), scanning electron microscopy (SEM), and electron backscatter diffraction (EBSD) accessories. The results show that the grain structure of the hot-deformed Zr–Sn–Nb–Fe-alloy samples is elongated along the thermal-deformation direction, forming a long, strip-like structure. Numerous recrystallized small grains and subgrain boundaries exist between these strips. The precipitated phases in the deformed samples with increasing temperature are primarily β-Zr, with minor amounts of β-Nb and $Zr(Fe, Nb)_2$, exhibiting a relatively uniform dispersion.

Key words: Zr–Sn–Nb–Fe alloy, hot deformation, microstructure, precipitate phase.

Еволюцію мікроструктури та преципітатів після гарячої деформації зразків Zr–Sn–Nb–Fe у фазах α й α + β досліджували за допомогою трансмісійної електронної мікроскопії (ТЕМ), енергодисперсійної рентґенівської спектроскопії (ЕДРС), сканувальної електронної мікроскопії (СЕМ) та дифракції зворотньо розсіяних (відбитих) електронів (ДЗРЕ). Результати

Corresponding author: Ali Wafaa Aldeen
E-mail: aliw.altalqani@uokufa.edu.iq

Citation: A. W. Aldeen, D. Y. Mahdi, and M. S. Tuma, The Effect of Hot Deformation in the α and α + β Phase Fields on the Microstructure and Precipitate Evolution of the Zr–Sn–Nb–Fe Alloy, *Metallofiz. Noveishie Tekhnol.*, **48**, No. 5: 483–493 (2026). DOI: 10.15407/mfint.48.05.0483

показують, що зерниста структура зразків гарячедеформованого стопу Zr–Sn–Nb–Fe є витягнутою вздовж напрямку термічної деформації, утворюючи довгу, смугоподібну структуру. Між цими смугами розташовані численні дрібні рекристалізовані зерна та межі субзерен. Фази, що виділяються в деформованих зразках із підвищенням температури, являють собою переважно β-Zr, з незначними кількостями β-Nb та $Zr(Fe, Nb)_2$, демонструючи відносно рівномірну дисперсію.

Ключові слова: стоп Zr–Sn–Nb–Fe, гаряча деформація, мікроструктура, фаза осаду.

(Received 11 February, 2026; in final version, 30 April, 2026)

1. INTRODUCTION

Zirconium alloys have long been widely used as fuel cladding materials for nuclear power reactors due to their advantages such as small neutron absorption cross-section, high thermal conductivity, and good resistance to waterside corrosion. As reactors develop towards high fuel consumption and long life, the in-core corrosion performance, hydrogen absorption performance, irradiation elongation, and creep performance of zirconium alloy cladding at high fuel consumption have become primary concerns. In the late 1970s, developed countries began to develop new zirconium alloy cladding materials and successively developed a series of new zirconium alloys, such as France's M5, the United States' ZIRLO, Russia's E635, Japan's DNA and MDA, and South Korea's HANA series alloys [1–4]. China has been conducting research on new zirconium alloys since the early 1990s. Through a series of studies, the composition of N36 zirconium alloy (Zr–1Sn–1Nb–0.3Fe) was determined, and industrial-scale pipe development work was carried out [5, 6].

Zirconium alloy preparing must undergo ingot melting, forging, homogenization, hot extrusion, annealing after hot extrusion, multiple cold rolling and intermediate annealing, cold rolling of finished products, and final annealing. Compared with Zr-4 alloy, the addition of Nb elements to N36 zirconium alloy reduces its $\alpha \rightarrow \alpha + \beta$ phase transformation temperature from about 810°C of Zr-4 alloy to below 680°C [7]. Therefore, the processing temperature of the new zirconium alloy should be reduced accordingly. In addition, when the Nb content is higher than 0.6%, Zr–Nb zirconium alloy will undergo segregation reaction at about 610°C, generating β-Zr [8–10]. In order to avoid the reduction of the corrosion resistance of the alloy due to the formation of β-Zr [11], the heat treatment of Zr–Nb alloy needs more practical fields to understand the segregation temperature and formation of precipitates.

This study used transmission electron microscopy (TEM), scanning

electron microscopy (SEM), and electron backscatter diffraction (EBSD) accessories to investigate the microstructure of Zr–Sn–Nb–Fe zirconium alloy plate hot-deformed at 600–750°C. The grain structure, grain boundary characteristics, and precipitation formation mechanism of the hot-deformed samples were analysed, providing a theoretical basis for subsequent processing.

2. EXPERIMENTAL/THEORETICAL DETAILS

2.1. Materials Sampling Method

In this study, the nominal composition of Zr–Sn–Nb–Fe zirconium alloy was Zr–1%Sn–1%Nb–0.3%Fe, and hot deformed was used at 600–750°C with strain rate 5 s^{-1} to investigate the microstructure evolution. Using SEM with its EBSD accessory and TEM, the specimens were observed along parallel ND–RD axis of the original plate (Fig. 1). The final diameter and height of the cylindrical samples used in this experiment was 6 mm. In order to be able to identify the RD observation area of the original plate on the sample after compression deformation, a small notch is left on the cylindrical surface to mark the RD of the plate.

2.2. Structural Characterization

The final diameter and height of the cylindrical samples used in this experiment was 6 mm. In order to be able to identify the RD observation area of the original plate on the sample after compression deformation, a small notch is left on the cylindrical surface to mark the RD of the plate. The Gleeble 3500 thermal simulation testing apparatus was used to finish the thermal compression experiment. EBSD samples were prepared using a vibratory polishing and chemical polishing method. The vibratory polisher was a BUEHLER VIBROMET2, and the

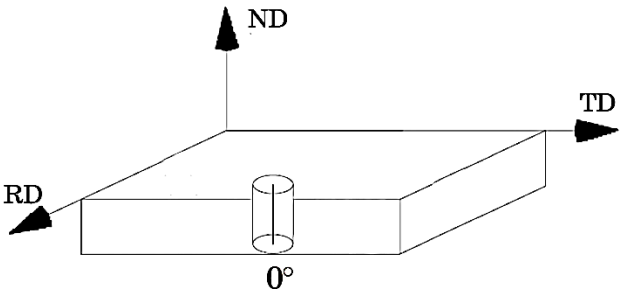

Fig. 1. Method of sampling from original plate.

chemical polishing solution was H_2SO_4:HNO_3:H_2O:HF = 15:30:45:6 (volume ratio). After chemical polishing, the samples were immediately rinsed with running water and alcohol. The prepared samples were characterized for microstructure using an EBSD system (HKL) equipped with a field emission scanning electron microscope (FEI NOVA NANO SEM 400). Electron beam scanning was used, with a typical scan step size of 0.1 μm and a scanning area of 150×150 points. HKL's CHANNEL-5 software was used for data analysis and microstructure reconstruction.

The precipitate phase was prepared using mechanical polishing and chemical etching. For observation, the sample was first polished to 5000# with sandpaper and then chemically etched using a solution of glycerol:nitric acid:hydrofluoric acid = 6:3:1 (volume ratio). After chemical polishing, it was immediately rinsed with running water. The surface was wiped clean with a clean cotton ball and ultrasonically cleaned in acetone for 3 minutes. The sample was then rinsed in 60°C concentrated nitric acid to remove polymeric substances adhering to the surface. The sample was then rinsed with running water and dried for later use. The morphology and composition of the precipitate phase were analysed using a FEI NOVA NANO SEM 400 with an EDS accessory. TEM samples were prepared using a mechanical thinning and electrolytic double-spray thinning method. The chemical thinning solution was $HClO_4$:CH_3CH_2OH = 11.5:86 (volume ratio). The prepared samples were analysed for grain structure and precipitated phases using a high-resolution transmission electron microscope.

3. RESULTS AND DISCUSSION

3.1. Grain Structure

Figure 2 shows the ND–RD plane EBSD reconstruction of the hot deformed samples at 600°C and 750°C. The analysis results show that the hot-deformed area exhibits a typical post-deformation locally dynamically recrystallized structure. Most of the grains are elongated, forming long strips approximately 20 μm long and 3 μm wide. These strips contain numerous subgrains, and most of the small grains have the same orientation or a small orientation difference. Locally, dynamically recrystallized grains are present, with an average grain size of approximately 0.5 μm. In addition, some grains show resistance to deformation process. Differences in hot deformation temperature led to variations in crystallographic orientation between the α and $\alpha+\beta$ phases in zirconium alloys, which are attributed to their distinct crystal structures, deformation mechanisms, and phase transformations governed by specific orientation relationships.

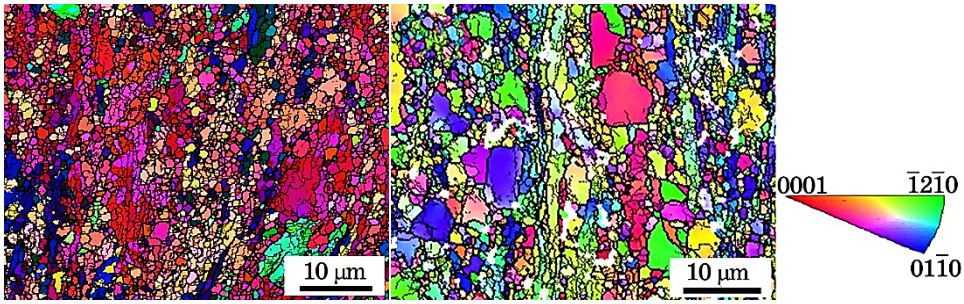

Fig. 2. EBSD Images of ND–RD observation area at 600°C (*a*), 750°C (*b*).

TEM analysis of hot deformed samples at different temperatures shows a trend that the structure consists primarily of two types of structures: lath-like structure and fine equiaxed recrystallized structure (Fig. 3, *a*). The laths contain a high density of dislocations (Fig. 3, *b*). The EBSD recrystallization positive polarity map of the hot-deformed sample also shows a small orientation difference between the deformed and recrystallized grains, indicating that dynamic recrystallization occurs through continuous subgrain boundary rotation (Fig. 4).

An average analysis of the EBSD grain boundary diagram reveals that this elongated microstructure contains high-density, small-angle grain boundaries surrounded by fine, equiaxed, dynamically recrystallized grains. There are two theories regarding its formation: the first one is the originally equiaxed grains, under high temperature and with suitable grain orientation and sufficient independent slip systems,

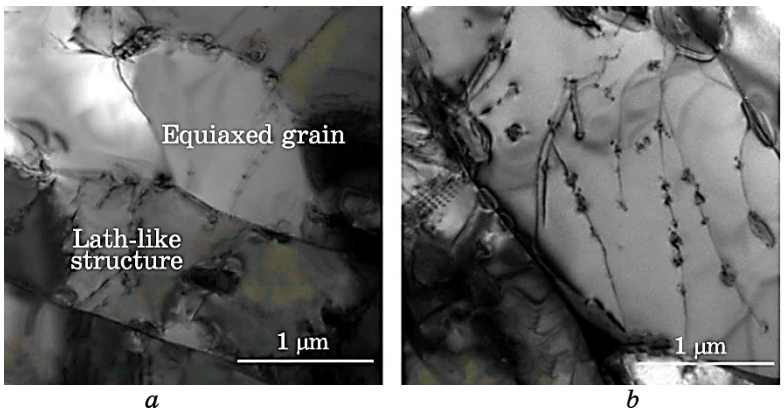

Fig. 3. TEM microstructure of deformed samples: lath and partial recrystallization structure (*a*); lath structure contains high density of dislocations (*b*).

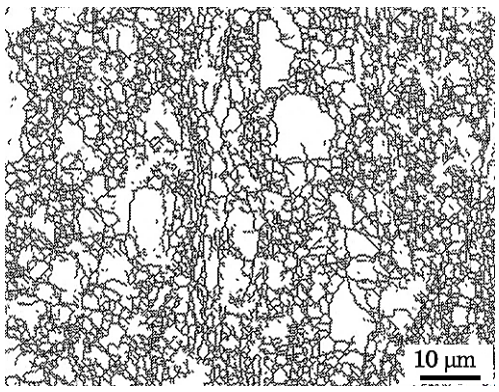

Fig. 4. EBSD grain boundaries map of hot deformed sample.

they can uniformly deform into elongated shapes, similar to the deformation of cubic metal grains; and the second one they are formed from original coarse equiaxed grains through continuous horizontal shearing and friction at high temperatures, with the large grains disappearing slowly and being partially retained [12–15]. Figure 4 shows that there are many subgrain boundaries within the large, elongated deformed grains, indicating that slip deformation also occurred within the elongated structure. The slip systems that zirconium alloys may excite at high temperatures mainly include the $\{10\bar{1}0\}<1\bar{2}10>$ cylindrical slip system, the $\{10\bar{1}0\}$ and $\{11\bar{2}1\}$ conical slip system, and can also be obtained through the $\{10\bar{1}2\}<\bar{1}011>$ twins promote the deformation of zirconium alloys, while the $\{10\bar{1}0\}<1\bar{2}10>$ and $\{10\bar{1}1\}<1\bar{2}10>$ slip systems can provide 2 and 4 independent slip systems [16, 17], respectively. This indicates that although Zr–Sn–Nb–Fe alloy has a relatively large number of independent slip systems at high temperatures, it still has fewer independent slip systems compared to cubic metals. On the other hand, from the perspective of orientation distribution, the orientation of the elongated structures is relatively close to that of the recrystallized equiaxed grains, both being slightly deflected tangential orientations, which are conducive to the activation of the $<\mathbf{a}>$ and $<\mathbf{a}+\mathbf{c}>$ slip systems [18]. This indicates that the original large grain orientations corresponding to these elongated structures are conducive to plastic deformation, while the distortion energy accumulated during the deformation process is relatively low. The original coarse grain orientations of other parts are not conducive to plastic deformation, and the distortion energy accumulated during the deformation process is relatively high.

Studies by K. Murty *et al.* have shown that under higher extrusion ratios, Zr–0.25Sn–1.0Nb–0.35Fe zirconium-alloy extrusion billets also exhibit similar elongated structures, while Zr-4 alloys all exhibit

fine equiaxed recrystallized structures. This indicates that the slower-diffusion Nb element may hinder the dynamic recrystallization of Zr–Sn–Nb–Fe zirconium alloys [19]. Therefore, during hot deformation, deformed structures with high distortion energy will become fine equiaxed dynamic grain structures due to dynamic recrystallization. The presence of Nb element hinders the dynamic recrystallization of some deformed structures with lower distortion energy, and the dislocations inside will merge to form small-angle grain boundaries or subgrain boundaries, still basically preserving the original grain structure the elongated tissue after deformation.

3.2. Precipitated Phase

SEM analysis showed that there were precipitates in the hot-deformed samples deformed at 600°C and 750°C (Fig. 5). Most precipitates which were distributed in a string-like pattern along the hot deformed direction, with an average size of more than 250 nm in an average. Most of the precipitates at 600°C are fine particles and the energy dispersive spectroscopy analysis shows that the mainly composed of Nb indicating high β-Nb precipitate percentage, and some of $Zr(Nb, Fe)_2$. At 750°C, the precipitate shows the same trend of elongated along the deformed direction, indicating that these precipitates have good plasticity. In niobium–zirconium alloys, except for the metallic β-Zr and β-Nb, the others are relatively hard and brittle intermetallic compound precipitates. β-Nb is generally finer. Energy dispersive spectroscopy analysis shows that most precipitates are mainly composed of Zr and a small amount of Fe and Nb. Considering that zirconium alloys with Nb content exceeding 0.6% will undergo segregation reaction at a certain temperature. Studies by Toffolon *et al.* have shown that the segrega-

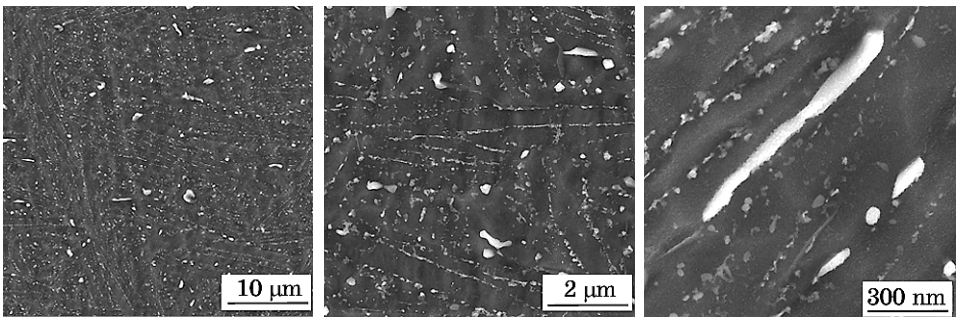

Fig. 5. SEM second phase particles image of hot deformed sample: low magnification at 600°C (*a*); high magnification at 600°C (*b*); sample deformed at 750°C (*c*).

tion temperature of Zr–1.0Nb is above 600°C, while studies by Hyun-Gil Kim *et al.* have shown that the segregation temperature of Zr–2.0Nb is approximately 585°C [8, 9]. However, the temperature during hot deformation of the Zr–Sn–Nb–Fe alloy in this study exceeds this temperature, allowing it to enter the $\alpha+\beta$ phase region. The β phase is likely to be retained at the end of deformation due to the rapid cooling rate. Therefore, the precipitates observed by SEM should almost be β-Zr.

TEM studies revealed that the precipitates in the hot-deformed samples were almost retained β-Zr structures at the grain boundaries (Fig. 6), and trace amounts of β-Nb and the $Zr(Fe, Nb)_2$ phase (Fig. 7). The Nb/Fe value in the $Zr(Fe, Nb)_2$ phase is relatively dispersed, ranging from about 0.1 to 15, while the Nb/Fe ratio in the Zr–Sn–Nb–Fe zirconium alloy containing the Nb and Fe second phase is generally in a smaller range [20–22]. This indicates that for primary products such as Zr–Sn–Nb alloy hot deformed samples, the distribution of alloying elements is not uniform. In addition to solid solutions in precipitates such as β-Zr and $Zr(Fe, Nb)_2$, a large number of alloying elements are supersaturated and solidly dissolved in the matrix, which is significantly different from a uniform equilibrium structure. A uniform equilibrium structure can be obtained through subsequent processing. K. Murty *et al.* study on Zr–0.25Sn–1.0Nb–0.35Fe zirconium alloy extrusion billets showed that the precipitates mainly consisted of harder intermetallic compound precipitates $Zr(Fe, Cr)_2$ and $(Zr, Nb)_4Fe_2$, as well as softer metallic precipitates β-Zr and β-Nb, *etc.* [19]. This indicates that even at lower deformation temperatures, Zr–Sn–Nb zirconium alloys may will produce β-Zr. Considering β-Zr and its string-like structures formed during subsequent processing, the adverse effects of distributed second-phase particles on the corrosion of zirconium al-

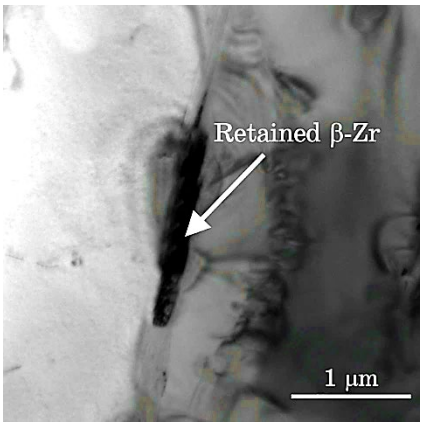

Fig. 6. Image of β-Zr precipitated in hot deformed samples.

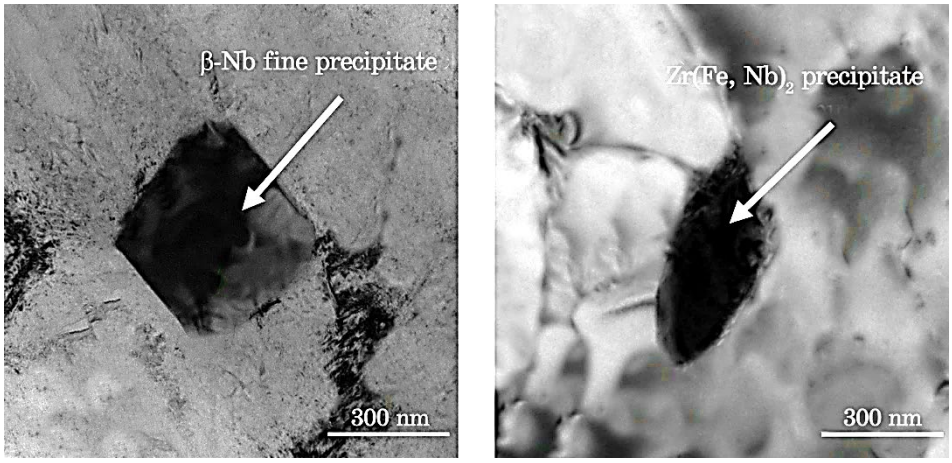

a *d*

Fig. 7. Image of precipitated β-Nb (*a*), $Zr(Fe, Nb)_2$ (*b*).

loy necessitate measures during subsequent processing to eliminate residual β-Zr and the formation of string-like second-phase distributions, resulting in a finely dispersed second-phase [21, 23]. Furthermore, considering that supersaturated Nb dissolved in the zirconium matrix also negatively impacts the corrosion resistance of zirconium alloys [24], Zr–Sn–Nb–Fe zirconium alloys should be deformed at the lowest possible temperature, with a larger rolling deformation and a lower annealing temperature to promote the full precipitation of Nb within the zirconium matrix, forming a finely dispersed second phase and improving the corrosion resistance of Zr–Sn–Nb–Fe zirconium alloys.

4. CONCLUSION

The results of studying microstructure and precipitates evolution of Zr–Sn–Nb–Fe alloy during hot deformation at α and α + β phase showed the following.

1. The alloy matrix is a mixture of lath-like structure and locally dynamically recrystallized fine-grained structure.
2. During deformation, most precipitates are distributed in a string-like pattern. At 600°C, fine particles with mainly composed of Nb indicate high β-Nb precipitate percentage, and some of $Zr(Nb, Fe)_2$. As temperature rises to the α + β two-phase region, residual β-Zr and trace amounts of β-Nb and $Zr(Fe, Nb)_2$ phases can be observed in the matrix.
3. This inhomogeneous microstructure negatively influences its corrosion resistance. Therefore, subsequent processing of Zr–Sn–Nb–Fe al-

loy should employ large deformation and low-temperature annealing processes to obtain a fine, dispersed second-phase microstructure, thereby improving the alloy corrosion resistance.

The authors gratefully acknowledge Baoji Five Elements Metal Co., Ltd, for the Zr alloy sheet. Special thanks to Mr. Erik Nilsson and Prof. Chen for their cooperation in this work.

AUTHORS' CONTRIBUTIONS

Ali W. Aldeen: methodology, validation, formal analysis, visualization, writing-original draft, review & editing, article structure construction. Dina Y. Mahdi: review & editing. Mohammed. S. Tuma: resources.

REFERENCES

1. B. O. Okonkwo, Z. Li, L. Li, J. Wang, and E.-H. Han, *Corros. Rev.*, **43**, Iss. 6: 609 (2024).
2. J. Hu and G. Cao, *Zirconium Alloy Coatings: Advances in Research and Applications* (Singapore: Springer Nature: 2025).
3. A. W. Aldeen, Z. W. Chen, I. A. Disher, M. Samiuddin, and K. Yan, *Phys. Met. Metallogr.*, **124**, No. 4: 362 (2023).
4. A. M. Garde, R. J. Comstock, G. Pan, R. Baranwal, L. Hallstadius, T. Cook, and F. Carrera, *Zirconium in the Nuclear Industry: 16th International Symposium* (Eds. M. Limbäck and R. Baranwal) (West Conshohocken, PA: ASTM International: 2012), **1529**, pp. 649–681.
5. C. Sun, Z. Yang, and Z. Wu, *World J. Nucl. Sci. Technol.*, **8**, No. 2: 30 (2018).
6. R. Qiu, B. Luan, L. Chai, X. Zhang, and Q. Liu, *Sci. China Technol. Sci.*, **56**, No. 1: 60 (2013).
7. W. Zhao, Y. Liu, H. Jiang, and Q. Peng, *J. Alloys Compd.*, **462**: 103 (2008).
8. C. Toffolon, J. Cristophe, and G, Jago, *ASTM Spec. Tech. Publ.*, **1423**: 361 (2002).
9. H.-G. Kim, J.-Y. Park, and Y.-H. Jeong, *J. Nucl. Mater.*, **347**, Nos. 1–2: 140 (2005).
10. R. Kondo, N. Nomura, Y. Tsutsumi, H. Doi, and T. Hanawa, *Acta Biomater.*, **7**, No. 12: 4278 (2011).
11. Y. P. Devi, H. Donthula, N. Keskar, A. Sarkar, K. Vaibhaw, and K. V. M. Krishna, *J. Nucl. Mater.*, **530**: 151978 (2020).
12. Y. Bi, B. Chen, L. Lu, and J. Yang, *Mater. Today Commun.*, **40**: 109524 (2024).
13. A. I. Dekhtyar, V. I. Bondarchuk, O. P. Karasevska, D. V Oryshych, D. G. Savvakin, and M. A. Skoryk, *Mater. Charact.*, **158**: 109949 (2019).
14. K. K. Saxena and V. Pancholi, *Met. Mater. Int.*, **27**, No. 7: 2106 (2021).
15. K. Saxena, V. Pancholi, G. Chaudhari, and D. Srivastava, *Mater. Sci. Forum*, **890**: 319 (2017).
16. A. Gaillac, C. Lemaignan, and P. Barberis, *Zirconium in the Nuclear Industry: 16th International Symposium* (Eds. M. Limbäck and R. Baranwal) (West Con-

shohocken, PA: ASTM International: 2012), **1529**, pp. 288–315.
17. E. Tenckhoff, *J. ASTM Int.*, **2**, No. 4: 1 (2005).
18. T. A. Hayes and M. E. Kassner, *Mechanical and Creep Behavior of Advanced Materials* (Ed. Linga Murty) (Springer: 2017), pp. 103–114.
19. K. L. Murty and I. Charit, *Prog. Nucl. Energy*, **48**, No. 4: 325 (2006).
20. A. V. Nikulina, V. A. Markelov, M. M. Peregud, Y. K. Bibilashvili, and V. A. Kotrekhov, *Zirconium in the Nuclear Industry: Eleventh International Symposium* (Eds. E. R. Bradley and G. P. Sabol) (West Conshohocken, PA: ASTM International: 1996), **1295**, pp. 785–804.
21. J. Huang, M. Yao, C. Gao, X. Liang, J. Peng, and J. Zhang, *Corros. Sci.*, **99**: 172 (2015).
22. C. Toffolon-Masclet, J.-C. Brachet, and G. Jago, *J. Nucl. Mater.*, **305**, Nos. 2–3: 224 (2002).
23. L. Chen, X. Song, H. Pang, and L. Liu, *Prog. Nucl. Energy*, **93**: 84 (2016).
24. B. D. C. Bell, S. T. Murphy, R. W. Grimes, and M. R. Wenman, *Acta Mater.*, **132**: 425 (2017).

Metallophysics and Advanced Technologies
Металофіз. новітні технол.
Metallofiz. Noveishie Tekhnol.
2026, vol. 48, No. 5, pp. 495–511
https://doi.org/10.15407/mfint.48.05.0495
Reprints available directly from the publisher

PACS numbers: 62.20.fg, 62.23.Pq, 75.60.Ej, 81.30.Kf, 81.40.Jj, 81.40.Rs, 81.70.Pg

Функціональні наноструктуровані композити на основі потрійних і четверних сполук Купруму

А. М. Тітенко, Л. Д. Демченко[*,***], Ю. М. Трощенков,
О. А. Тітенко[*], В. М. Муравйов[**]

Інститут магнетизму імені В. Г. Бар'яхтара НАН України,
бульв. Академіка Вернадського, 36[б],
03142 Київ, Україна
[*]*Національний технічний університет України*
«Київський політехнічний інститут імені Ігоря Сікорського»,
просп. Берестейський, 37,
03056 Київ, Україна
[**]*Державний університет інфраструктури та технологій,*
вул. Кирилівська 9,
04071 Київ, Україна
[***]*Department of Chemistry, Stockholm University,*
16C Svante Arrhenius väg,
SE-106 91 Stockholm, Sweden

Corresponding author: Anatoliy Mykolayovych Titenko
E-mail: titenko@imag.kiev.ua

V. G. Baryakhtar Institute of Magnetism of the N.A.S. of Ukraine,
36[b], Academician Vernadsky Blvd., UA-03142 Kyiv, Ukraine
[*]*National Technical University of Ukraine 'Igor Sikorsky Kyiv Polytechnic Institute',*
37, Beresteiskyi Ave., UA-03056 Kyiv, Ukraine
[**]*State University of Infrastructure and Technologies,*
9, Kyrylivs'ka Str., UA-04071 Kyiv, Ukraine
[***]*Department of Chemistry, Stockholm University,*
16C Svante Arrhenius väg, SE-106 91 Stockholm, Sweden

Citation: A. M. Titenko, L. D. Demchenko, Yu. M. Troshchenkov, O. A. Titenko, and V. M. Muravyov, Functional Nanostructured Composites Based on Ternary and Quaternary Copper Compounds, *Metallofiz. Noveishie Tekhnol.*, **48**, No. 5: 495–511 (2026) (in Ukrainian). DOI: 10.15407/mfint.48.05.0495

В роботі розглянуто концептуальні можливості використання інтелектуальних матеріялів здатних одночасно виконувати функції актуаторів і датчиків зміни станів. В якості таких елементів пропонується використовувати наноструктуровані феромагнетні стопи з пам'яттю форми на основі багатокомпонентних стопів міді. Проведено порівняльну аналізу непружньої деформаційної поведінки стопів CuAlMn(Fe), отриманих різними методами, з відомими аналогами, що свідчить про потенційні можливості застосування їх у деформаційних пристроях відновлювальної дії. На масивних полікристалічних зразках CuAlMn(Fe) визначено морфологічні та кінетичні особливості під час індукування мартенситних перетворень, які пов'язані зі зміною магнетного стану в результаті появи наведеної анізотропії форми і напряму залежать від запропонованого термомагнетного оброблення. Досліджено електричні та магнетні характеристики вибраних стопів. На відміну від CuAlMn-стопів, стопи CuAlMnFe майже не змінюють питому намагнетованість з температурою та часом низькотемпературного відпалу, що пов'язане з превалюванням антиферомагнетного впорядкування над феромагнетним. Виходячи з одержаних властивостей наноструктурованих CuAlMnFe-стопів зроблено висновок стосовно можливостей використання їх в якості смарт-матеріялів різноманітного призначення.

Ключові слова: смарт-матеріяли, надпружність, ефект пам'яті форми, намагнетованість, актуатор, магнетна анізотропія, термопружнє мартенситне перетворення, магнетне поле.

The paper examines the conceptual possibilities of using intelligent materials capable of simultaneously performing the functions of actuators and state-change sensors. As such elements, it is proposed to use nanostructured ferromagnetic alloys with shape memory based on multicomponent copper compounds. A comparative analysis of the inelastic deformation behaviour of CuAlMn(Fe) alloys obtained by various methods with known analogues is carried out, which indicates the potential possibilities of their use in deformation devices of restorative action. On the massive polycrystalline CuAlMn(Fe) samples, morphological and kinetic features are revealed, when martensitic transformations are induced, which are associated with a change in the magnetic state because of the appearance of the induced anisotropy of the shape and directly depend on the proposed thermomagnetic treatment. The electrical and magnetic characteristics of the selected compounds are studied. Unlike CuAlMn alloys, CuAlMnFe alloys almost do not change the specific magnetization with temperature and time of low-temperature annealing that is due to the predominance of antiferromagnetic ordering over ferromagnetic. Based on the obtained properties of nanostructured CuAlMnFe alloys, a conclusion is made regarding the possibilities of their use as smart materials for various purposes.

Key words: smart materials, superelasticity, shape-memory effect, magnetization, actuator, magnetic anisotropy, thermoelastic martensitic transformation, magnetic field.

(Отримано 27 серпня 2024 р.; остаточн. варіянт — 20 листопада 2024 р.)

1. ВСТУП

Наука про матеріяли (materials science) стало рухається до створення інтелектуальних матеріялів. Підґрунтям для такої трансформації є більш прискіпливі вимоги до їхніх можливостей, що вимагають спеціяльних властивостей (електричних, магнетних, температурозалежних). Такі матеріяли мають одночасно виконувати певні дії (актуатори) та забезпечувати функції давачів (сенсорів). Типовим представником функціональних і одночасно конструкційних матеріялів є металеві стопи з термопружніми мартенситними перетвореннями (ТМП) та ефектом пам'яті форми (ЕПФ) [1–4].

Сучасна аналіза можливостей функціональних матеріялів з ЕПФ як виконавчих елементів циклічної дії, засобів автоматизації свідчить про їхній значний потенціял і перспективи використання. Області застосування термосилових пристроїв у системах електричного управління охоплюють: термочутливі прилади (засоби сиґналізації, міряння, контролю та реґулювання параметрів робочих середовищ, захисно-запобіжні пристрої), діючі автоматично та керовані дистанційно приводи малогабаритних виконавчих пристроїв (реле, дозатори, імпульсні клапани, реґулятори, розподілювачі, запірна, реґулювальна та перемикувана арматура), конструктивні елементи механізмів, трубопроводів, електричних мереж (компенсатори, віброізолятори, термомеханічні з'єднання). Найбільш перспективним стають ФСПФ (феромагнетні стопи з пам'яттю форми) в пристроях, елементи яких об'єднують термочутливі та силові функції, забезпечуючи при цьому можливість варіювання швидкостей спрацювання в широких межах без зміни навантажувальної здатности, поліпшення масогабаритних показників і спрощення конструкцій, можливість дистанційного управління [1, 2]. Розширення сфери застосування їх спостерігається в галузях машинобудування, робототехніці, автоматиці, медицині, біології тощо [3].

Функціональні властивості смарт-матеріялів із ФСПФ забезпечуються та ґрунтуються на низці термосилових ефектів: ЕПФ, надпружности (НП), феропружности, пластичности перетворення, демпфуванні тощо. В основу НП покладено явище оборотнього відновлення вихідної форми після зовнішніх силових впливів шляхом трансформації структури або переорієнтації її за ТМП. Зазначимо чинники, які впливають на НП-поведінку в ФСПФ. За одновісного стискання спостерігається зменшення частки відновлюваної деформації, ніж за одновісного розтягу, більш крутий нахил за перетворення з більш високим критичним напруженням індукування МП [4, 5].

Дослідники перманентно спрямовують зусилля на створення адаптивних елементів конструкцій з відповідним відображенням структурних змін щодо зовнішнього впливу через зміни магнетних

та електричних станів. В цьому сенсі варто виокремити стопи Cu–Al–Mn, в яких парамагнетна матриця зазнає індукованого ТМП, а феромагнетні частинки, що утворюються під час високотемпературного старіння, не зазнають ТМП і під впливом зсувних деформацій матриці змінюють свої магнетні й електричні характеристики. Зміну магнетних властивостей зумовлено формуванням особливої наноструктури, що складається з анізотропних за формою та розташуванням фаз, які відрізняються величиною намагнетованости наситу. Чинниками, які сприяють змінам вихідної структури Cu–Al–Mn при цьому можуть бути: анізотропія пружніх констант матриці, анізотропія форми й об'ємної долі частинок, величини невідповідности кристалічних параметрів фаз ґратниць, ріжниця пружніх модулів фаз тощо.

Метою роботи є визначення можливостей застосування багатокомпонентних смарт-матеріялів ФСПФ на основі міді в якості потенційних матеріялів, що здатні одночасно поєднувати функції актуаторів і давачів шляхом використання їхньої надпружньої поведінки з відповідними змінами магнетоелектричних показників за індукування термопружніх фазових перетворень.

2. ОБ'ЄКТИ ДОСЛІДЖЕНЬ ТА ЕКСПЕРИМЕНТАЛЬНІ МЕТОДИКИ

Об'єктами досліджень було обрано багатокомпонентні стопи на основі Cu–Al–Mn, Cu–Al–Mn–Fe: $CuAl_{11,2}Mn_{6,35}Fe_{0,925}$, Cu–12,4 Al–5,03 Mn та Cu–12,4 Al–6,5 Mn (% ваг.) у вигляді масивних зразків і тонких фолій з різним вмістом леґувальних компонентів за відмінних режимів одержання та термомеханічного оброблення, а також фактичним порівнянням їхніх показників з відомими аналогами. До досліджуваних сполук застосовувалися наступні методи досліджень: структурні дослідження (XRD, SEM, DSC), магнетні методики низькопольової магнетної сприйнятливости та статичної намагнетованости (вібраційний магнетометер), електроопору (чотириточковим методом). До об'єктів досліджень застосовувалося різне оброблення, в тому числі термооброблення з накладанням зовнішнього магнетного поля різної орієнтації.

3. РЕЗУЛЬТАТИ ТА ЇХ ОБГОВОРЕННЯ

Механічні властивості CuAlMn- і CuAlMnFe-стопів. Розглянемо механічні параметри й ефекти, які реалізуються у зазначених стопах. Стопи Cu–Al–Mn мають достатньо високі механічні показники в широких інтервалах прояву оборотніх деформаційних ефектів. Недоліками є: мала пластичність і низька оброблюваність полікри-

сталічних стопів з великим зерном, що зумовлено високою пружньою анізотропією $A = C_{44}/C' \cong 12–13$ відносно пружньоізотропних стопів NiTi з $A \cong 1–2$ [6], і виділення частинок крихкої фази. До пониження пластичности призводить також гетерогенний розпад, особливо в крупнозернистому стані. Допування бінарних стопів Mn ефективно сприяє збільшенню пластичности, непружности, НП, ЕПФ [7] і стимулює індукування гігантського магнетоопору [8].

Суто визначив, що в стопах Cu–Al–Mn із вмістом Алюмінію менше 18% проявляється значний ЕПФ і вища пластичність, аніж у стопах Cu–Al–Ni під час фазових переходів. Однак загальна НП обмежена лише 2% замість 8%, які досягаються в Cu–Zn–Al, і майже 10%, які можливі в Cu–Al–Ni [9, 10]. Висока пластичність, більша за 11%, реалізується в стопі $Cu_{71,5}Al_{17,5}Mn_{11}$ зі стовпчастою текстурою <001> зерна [11]. Основним чинником малої НП в CuAlMn стопах з дрібнозернистою структурою є обмеження, пов'язане з малою величиною відношення зерна аустеніту до товщини зразка, яке спричиняє ефект затиснення.

В стопі Cu–17 Al–15 Mn до 273 К не виявлено ТМП, а НП складає вже 8,5% за 77 К. Критичні напруження для індукованого ТМП зменшуються з пониженням температури, а його ґрадієнт стає меншим за низьких температур через зменшення ентропії, яка за 77 К становить 0,46 Дж/(моль·К) і відповідає лише третині за 221 К [12].

Монокристал Cu–12,4 Al–6,5 Mn–3,2 Fe за кімнатної температури демонструє повну НП у 7%, а також реґульовний ЕПФ до 8,8%. Монокристал з ЕПФ Cu–12,9 Al–5,6 Mn–3,8 Fe (% мас.) одночасно проявляє повну НП у 12% в першому циклі навантаження й ЕПФ у 9% за двократного циклічного навантаження за кімнатної температури [12]. Для $Cu_{71,3}Al_{17}Mn_{8,7}Ni_3$ за температури випробовування у 500°С та швидкости деформування у $5 \cdot 10^{-4}$ с$^{-1}$ було одержано пластичність стопу на рівні 1150%, а за 450°С — 385% [25].

Порівняльні характеристики стопів зведено до табл. 1.

В плані керування механічними характеристиками феромагнетних металевих матеріялів додатковими важелями впливу може слугувати накладання постійних або змінних магнетних полів під час деформації, що позначається на величинах: межі плинности та міцности, видовженні, плазучости, втомної міцности, релаксації напружень. Наявність магнетного поля за пластичної деформації може сприяти знеміцненню (позитивний магнетопластичний ефект — МПЕ), так і зміцнення (від'ємний МПЕ) матеріялів під впливом магнетного поля різної природи [26]).

Виходячи із термомеханічної поведінки зазначених непружніх можливостей потрійних і четверних стопів CuAlMnFe, видається достатньо вагомим арґументом на користь застосування їх в якості робочих елементів актуаторів за термосилових впливів, величини

ТАБЛИЦЯ 1. Порівняльні характеристики непружньої поведінки відомих стопів (з певними аспектами) (d/t — відношення величини зерна до товщини зразка).

TABLE 1. Comparative characteristics of inelastic behaviour of known alloys (with certain aspects) (d/t is ratio of grain size to sample thickness).

Склад стопів	НП, %	ЕПФ, %	Особливості	Посилання
$CuAl_{12,4}Mn_{6,5}Fe_{3,2}$	5,8	8,8	Монокристал	[13]
$Cu_{71,9}Al_{16,6}Mn_{9,3}Ni_2B_{0,2}$	7,5		Полікристал	[14]
$Cu_{71,6}Al_{17,0}Mn_{11,4}$	6/4,5		Полі/монокристал	[15, 16]
$Cu_{68,4}Al_{27,8}Ni_{3,8}$	8,6		Монокристал	[17]
$Cu_{67,9}Zn_{16,1}Al_{16}$	8,5		Монокристал	[18]
$Cu_{67,11}Zn_{24,25}Al_{8,57}Zr_{0,07}$	4,5		Монокристал	[19]
$(Cu_{73,5}Al_{17,5}Mn_9)_{97}Ni_3$	$\approx 6\%$ (d/t)		Полікристал	[20]
$Cu_{71,5}Al_{17,5}Mn_{11}$	$> 14\%$		Стовпчасте зерно, двостадійне МП	[21]
$Ni_{50}Ti_{50}$	7,3		Полікристал	[22]
$Fe_{40,95}Ni_{28}Co_{17}Al_{11,5}Ta_{2,5}B_{0,05}$	13,5		Полікристал	[23]
на основі Cu		7,0		[24]

яких залежать від термосилових параметрів фазових перетворень.

Електричні та магнетні властивості потрійних і четверних стопів. Упродовж значного часу напрацьовано великий доробок результатів, пов'язаних з можливостями реґулювання параметрів ТМП стопів на мідній основі в результаті хемічного леґування, використання комплексних режимів термомеханічного оброблення для підгонки потрібних температур і діяпазонів перетворень, що впливатиме на керування фізичними властивостями, зокрема механічними, магнетними, електричними тощо [27]. За індукування ТМП відбувається зміна магнетних та електричних показників, використання яких може забезпечити відповідну фіксацію стану матеріялу щодо зовнішніх впливів, що важливо для використання в якості сенсорів. Варіюючи хемічний склад або термомеханічні оброблення можна досягати змін температури та величини гістерези в широкому інтервалі температур або підганяти параметри МП, його гістерези до заданої величини [28].

Під час індукування МП із вибуховою кінетикою в зразках стопу Fe–Ni спостерігається виникнення сиґналів [29, 30] термо-е.р.с. завдяки наявності ґрадієнту температур за переміщення міжфазної межі (із теплотою перетворення у 5,3 кал/г), тоді як за ізотермічної кінетики МП імпульси е.р.с. не спостерігаються. Зазначено, що із

збільшенням зерна аустеніту амплітуда сиґналу [30] збільшується до 0,7 мВ, а в разі накладання магнетного поля амплітуда сиґналу змінної форми може становити 10 мВ.

Зручними та надійними засобами ідентифікації ТМП є поширені методики ДСК, низькопольової магнетної сприйнятливости й електроопору. В якості об'єкта дослідження запропоновано четверний стоп $CuAl_{11,2}Mn_{6,35}Fe_{0,925}$, що демонструє типове ТМП з порівняно широкою температурною гістерезою. Трансформація ТМП у четверних сполуках [31] засвідчила істотні зміни в морфології та кінетиці ТМП: від термопружнього до двостадійного перетворення, в тому числі із вибуховою кінетикою. За результатами ДСК стоп виявляє ознаки ТМП з такими параметрами: $M_s = 10{,}1$°C, $M_f = -29{,}6$°C, $A_s = 3{,}4$°C, $A_s = 54{,}7$°C, $\Delta M = M_f - M_s \cong 40$°C, $\Delta A = 57$°C, $\Delta T \cong 30$°C. Мікроструктура (рис. 1) характеризується утворенням голчастого мартенситу і за кімнатної температури характеризується великим розміром зерна $y \cong 3$ мм переважно рівновісної форми. Треба зазначити, що температурні інтервали прямого й зворотнього МП мають протяжний характер, що є вірогідним наслідком неоднорідности хемічного складу зразків (рис. 2).

На сучасному етапі розвинуто та накопичено уявлення стосовно поведінки потрійних стопів Cu–Al–Mn за термомагнетного оброблення (ТМО). В цьому контексті значну увагу привертають зразки, які зазнали термомагнетного оброблення. ТМО вносить істотні корективи в магнетну й електричну поведінку потрійних наноструктурованих сполук під час індукування МП стопу Cu–12,4 Al–5,03 Mn (рис. 3).

Ріст електроопору за МП зумовлено більш дефектною структу-

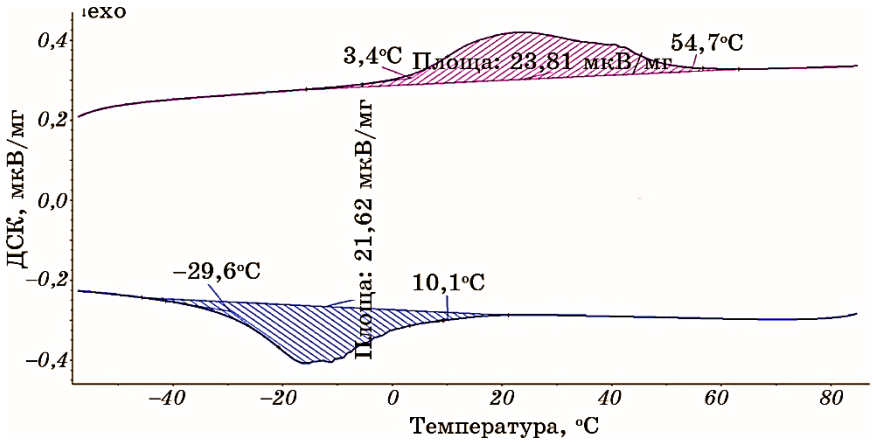

Рис. 1. ДСК четверного $CuAl_{11,2}Mn_{6,35}Fe_{0,925}$ стопу.

Fig. 1. DSC of the quaternary $CuAl_{11.2}Mn_{6.35}Fe_{0.925}$ alloy.

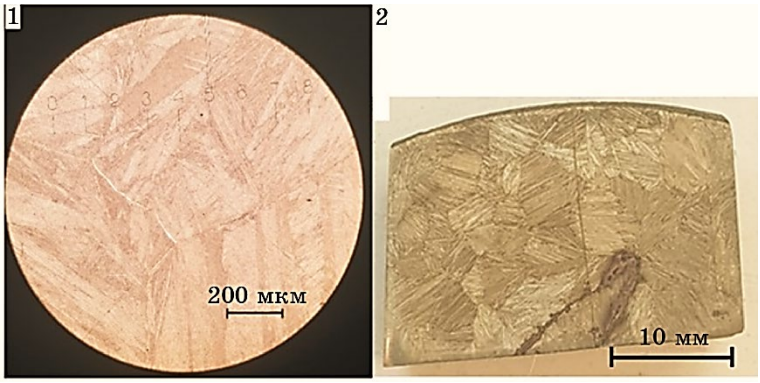

Рис. 2. Мікроструктура стопу $CuAl_{11,2}Mn_{6,35}Fe_{0,925}$ в загартованому стані: 1) збільшення у 130 разів, 2) без збільшення.

Fig. 2. Microstructure of $CuAl_{11.2}Mn_{6.35}Fe_{0.925}$ alloy in the tempered state: 1) 130-fold increase, 2) without increase.

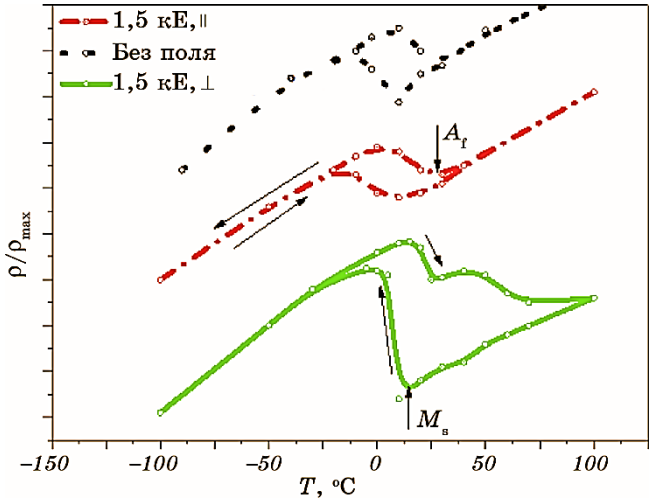

Рис. 3. Температурні залежності електроопору стопу Cu–12,4 Al–5,03 Mn за різного ТМО.

Fig. 3. Temperature dependence of the electrical resistance of the Cu–12.4 Al–5.03 Mn alloy at different TMT.

рою мартенситу, тоді як сиґнал χ/χ_{max} (рис. 4) пропорційний розмірам феромагнетних частинок Cu_2AlMn, розміщених у парамагнетній матриці, коли за зсувної деформації матриці виникає наведена анізотропія форми частинок.

Зменшення амплітуди сиґналу $\chi(T)$ є еквівалентним зменшенню

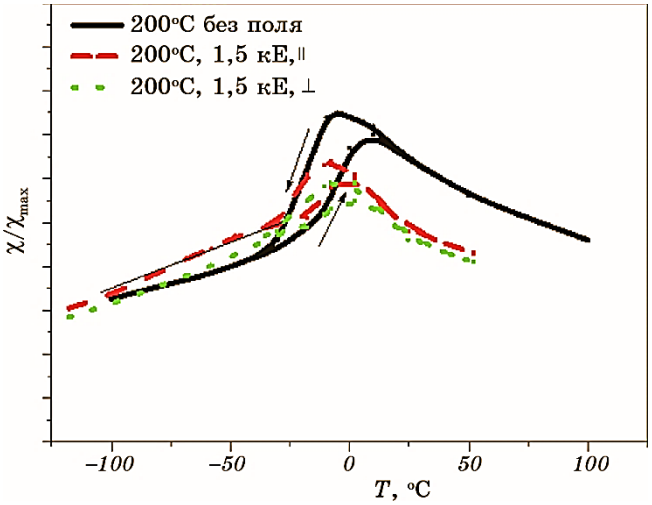

Рис. 4. Температурні залежності низькотемпературної магнетної сприйнятливости стопу Cu–12,4Al–5,03Mn за різного ТМО.

Fig. 4. Temperature dependence of the low-temperature magnetic susceptibility of the Cu–12.4Al–5.03Mn alloy at different TMT.

намагнетованости I/I_0 з температурою, що характеризується відповідним відношенням $I/I_0 \cong \mu H/(3kT)$ і за високих температур призводить до деґрадації магнетного впорядкування.

Зміни в кінетиці та морфології МП стопу з однаковим хемічним складом ймовірно пов'язані зі зменшенням розміру феромагнетних наночастинок відповідно до термодинамічних розрахунків [32] або із збільшенням анізотропії форми, а саме, до більш орієнтованого напрямку росту наночастинок відносно напрямку магнетного поля. До такого висновку можна підійти, враховуючи істотне зменшення амплітуди сиґналу χ та ρ в зразках за ТМО. За паралельної орієнтації головної осі зразка за ТМО магнетна сприйнятливість демонструє плавний перехід через трансформацію структури, як за прямого, так і зворотнього МП. Ізотермічний відпал за перпендикулярної орієнтації зразка із ТМО демонструє різкий перехід для прямого МП і двостадійну трансформацію за зворотнього ТМП. В роботі під час ідентифікації МП у стопах Cu–Al–Mn за накладання сталого магнетного поля не спостерігається зміщень температур переходу, а із збільшенням напруженості прикладеного магнетного поля зростає амплітуда електроопору [33].

Мінімізація вільної енергії з утворенням феромагнетної фази виділення відбувається в результаті конкурування між магнетостатичною та поверхневою. Якщо за термічного оброблення утворення форми фази виділення відбувається за конкуренції між пружньою

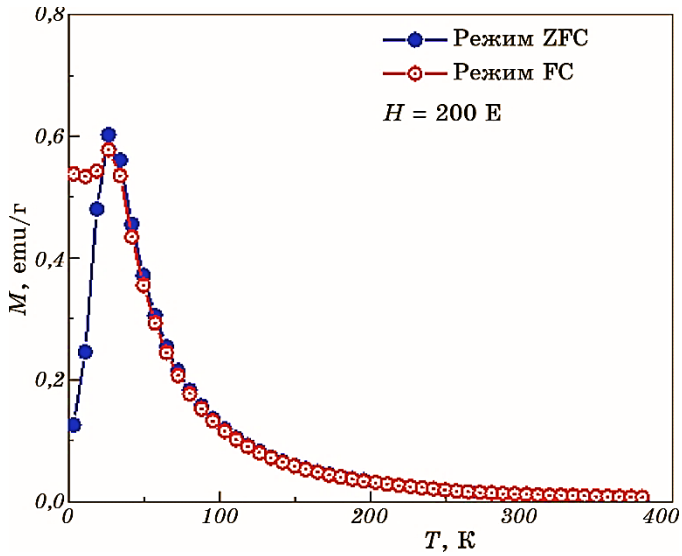

Рис. 5. Криві температурної залежности питомої намагнетованости стопу Cu–12,4 Al–6,5 Mn в режимі ZFC та FC за 200 Е.

Fig. 5. Curves of the temperature dependence of the specific magnetization of the Cu–12.4 Al–6.5 Mn alloy in the ZFC and FC modes with 200 Oe.

та поверхневою енергією, то за ТМО форма виділення залежить від конкуренції між поверхневою та магнетостатичною енергіями. Ефект ТМО в старіючих ФСПФ має анізотропний характер за формування феромагнетних наночастинок.

На рисунках 5, 6 представлено магнетну поведінку швидкозагартованої стрічки стопу Cu–Al–Mn: температурну залежність намагнетованости (рис. 5) та ізотермічні криві намагнетованости за різних температур від 3 К до 380 К (рис. 6). У високотемпературній області стоп перебуває в парамагнетному стані та в подальшому із пониженням температури переходить у суперпарамагнетний стан (відсутність коерцитивної сили), а за температури у 26,6 К — до стану спінового скла. Наявність переходу суперпарамагнетик–спінове скло можна пов'язати з дипольною взаємодією частинок, які за зсувної деформації в межах мартенситних кристалів зазнають наведеної анізотропії форми. Відповідні розрахунки [34] свідчать, що наведена напруженнями анізотропія на 2 порядки перевищує кристалографічну, що приводить до анізотропії форми частинок і фіксації магнетних властивостей саме через них. Із зменшенням температури зростає величина коерцитивної сили, що відповідає однодоменному стану анізотропних частинок переважно малого розміру (відносно низька температура переходу).

Ефект ізотермічного старіння та часу витримки не має сильного

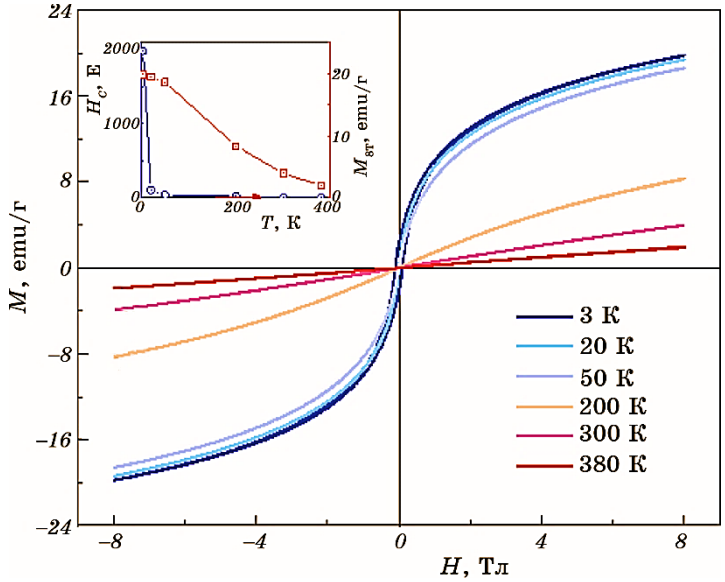

Рис. 6. Ізотермічні криві польових залежностей питомої намагнетованости Cu–12,4 Al–6,5 Mn за різної температури міряння. Вставка: залежності намагнетованости наситу та коерцитивної сили від температури.

Fig. 6. Isothermal curves of field dependences of the specific magnetization of Cu–12.4 Al–6.5 Mn at different measurement temperatures. Inset: dependences of saturation magnetization and coercive force on temperature.

впливу на магнетні характеристики стопу CuAlMnFe, і, можливо, це пов'язане з превалюванням антиферомагнетного впорядкування над феромагнетним, а також сильною магнетокристалічною анізотропією стопу, який за кімнатної температури перебуває в мартенситному стані (рис. 7), що притаманне потрійним стопам CuAlMn (рис. 7, *а*). Наведена МП кристалічна анізотропія матриці блокує його насит в полі до 20 кЕ на противагу випадку, коли частинки розміщені в аустенітній матриці.

Аналогічна картина спостерігається у стопах Cu–Al–Mn(Co), де падіння намагнетованости по відношенню до стопу без Кобальту сягає 5-кратного рівня. За думкою авторів, додавання Кобальту блокує виділення фази Cu_2AlMn, проте одночасно з цим вдвічі збільшується пластичність стопів [35].

Механічні характеристики Cu–Al–Mn(Fe). На рисунку 8 представлено діяграми вдавлювання $CuAl_{11,2}Mn_{6,35}Fe_{0,925}$. Мікротвердість та модуль пружности за кімнатної температури: $H = 3{,}7$ ГПа, $E = 61$ ГПа. Величина відновлюваної деформації за кімнатної температури — $Re = ((3{,}44 - 2.44)/3{,}44)\cdot 100\% = 29{,}069\%$. Відносно невеликі показники відновлюваної деформації стопу Cu–Al–Mn(Fe)

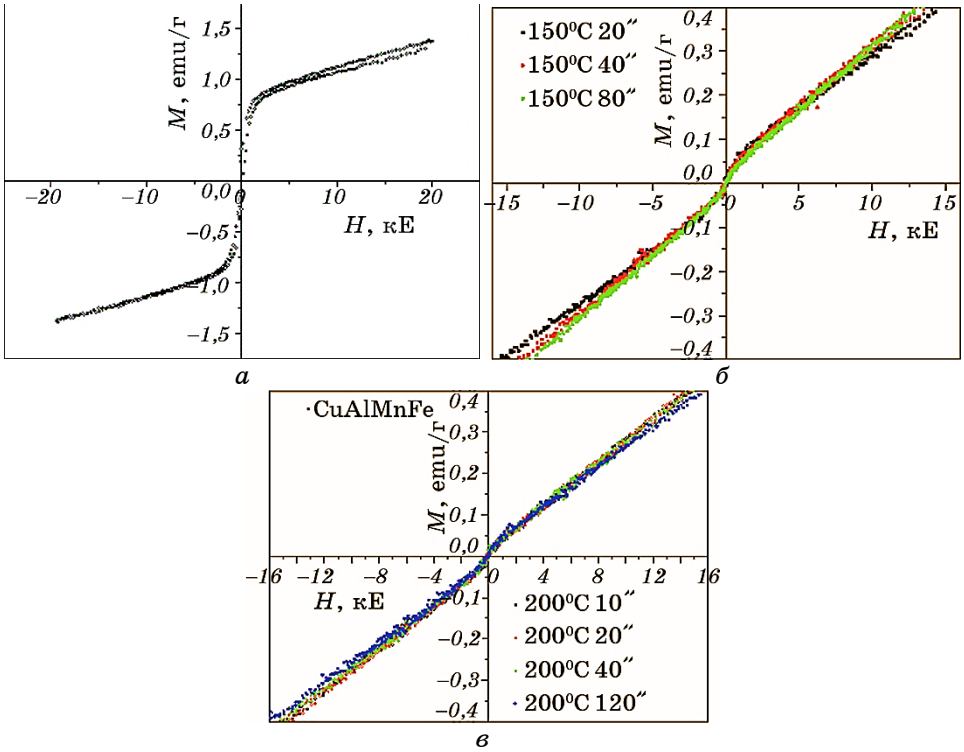

Рис. 7. Петлі гістерезисні питомої намагнетованости: стопів Cu–12,4 Al–5,03 Mn за старіння (200°C, 3 год.) (*а*), стопу $CuAl_{11,2}Mn_{6,35}Fe_{0,925}$ за відпалу (100, 150, 200°C в залежності від часу старіння) (*б*, *в*).

Fig. 7. Hysteresis loops of specific magnetization: Cu–12.4 Al–5.03 Mn alloys at 200°C 3 hours ageing (*а*); $CuAl_{11.2}Mn_{6.35}Fe_{0.925}$, when annealed at 100, 150, 200°C depending on the ageing time (*б*, *в*).

пов'язані з наявністю двофазного стану (аустеніт + мартенсит), коли термодинамічна стійкість індукованого навантаженням МП під зовнішнім впливом зберігається під час розвантаження, на відміну від деформування фолій Cu–Al–Mn в повністю аустенітному стані (рис. 9).

Для полікристалічних зразків з мікрозеренною структурою відносне збільшення відновлюваної деформації фіксується із збільшенням циклів навантаження–розвантаження через 1% отриманої деформації в результаті зміцнення матриці. Накопичення структурних дефектів під час циклювання також сприяє поліпшенню демпфувальних характеристик.

На рисунках 9, 10 представлено циклічні криві навантаження–розвантаження (за деформування зразків із збільшенням деформа-

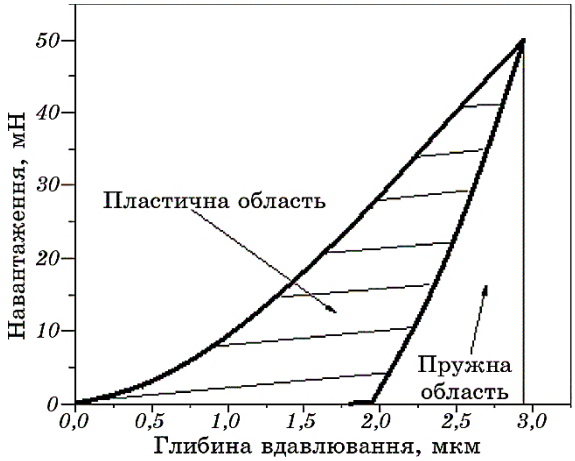

Рис. 8. Діяграма вдавлювання стопу Cu–Al–Mn–Fe.

Fig. 8. Indentation diagram of the Cu–Al–Mn–Fe alloy.

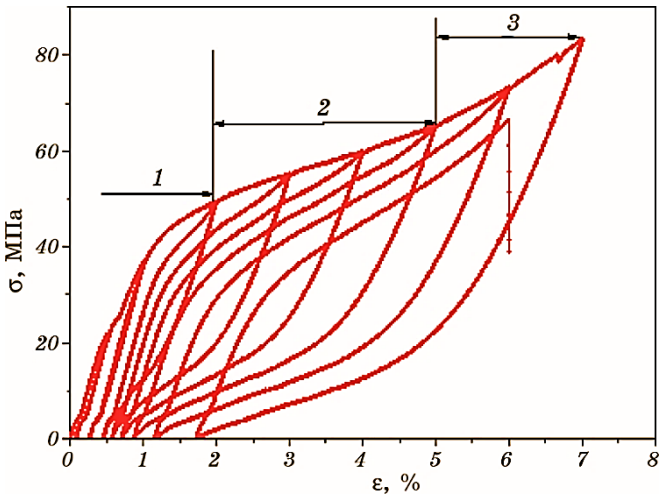

Рис. 9. Криві напруження–деформація (циклічні вздовж осі стрічки) стопу Cu–12,4 Al–6,5 Mn.

Fig. 9. Cyclic stress–strain curves (along the strip axis) of the Cu–12.4 Al–6.5 Mn alloy.

ції на кожний 1%) за одновісного розтягу швидкозагартованих стрічок стопу за кімнатної температури (з температурами прямого МП $M_s = -55$°C, $M_f = -95$°C (в інтервалі $\Delta M = 40$°C) та зворотнього МП $A_s = -34$°C, $A_f = -5$°C (в інтервалі $\Delta A = 30$°C)).

На деформаційних кривих прослідковується індукування марте-

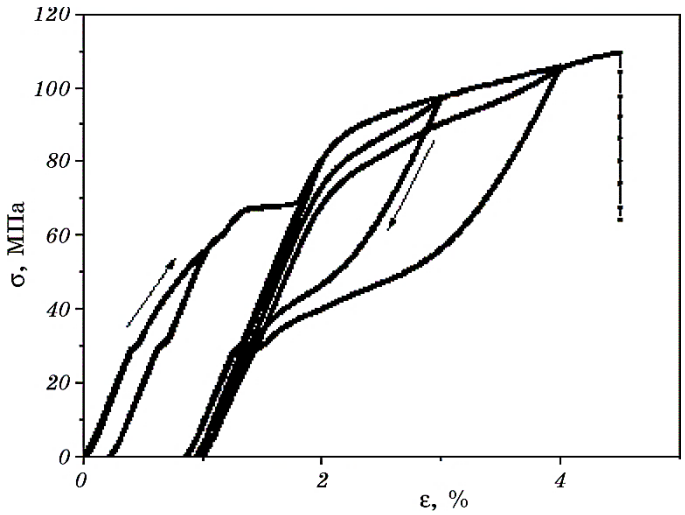

Рис. 10. Криві напруження–деформація (поперек осі стрічки) стопу Cu–12,4 Al–6,5 Mn.

Fig. 10. Stress–strain curves (across the strip axis) of the Cu–12.4 Al–6.5 Mn alloy.

нситного перетворення, оскільки температура випробовування $T > A_f$. Збільшення відновлюваної деформації пов'язане з прийнятною орієнтацією зразка по відношенню до зусилля, яке прикладається, та зміцненням матриці за деформування. З кожним циклом відновлювана деформація збільшується: *1* — 70% (0–2%), *2* — 82% (2–4,5%), *3* — 75% (4,5–7%), в той час як коефіцієнт деформаційного зміцнення $d\sigma/d\varepsilon$ в інтервалі *2* має сталу величину 5,22 і в третьому інтервалі збільшується вдвічі до 9 МПа. Модуль модуля в першому циклі становить $E = 5085$ МПа. В останньому циклі відбувається зрив напруження, що спричиняє розрив зразка. Для цього стопу має місце орієнтаційний характер деформування. Одновісний розтяг зразка поперек осі стрічки приводить до зміцнення на 20% через двократну втрату пластичности (рис. 10). Таке розходження в механічній поведінці стрічок пояснюється нерівномірністю по товщині та неоднорідним розподілом хемічних складових в об'ємі зразків. Робота в технологічному аспекті над структурними неоднорідностями та стабілізацією товщини може відкрити додаткові можливості керування механічними та магнетними параметрами стопів.

Практичні застосування. Перспективність застосування стопів на мідній основі зазначено в багатьох наукових джерелах [35]. Використовуючи високі механічні показники наноструктурованих Cu–Al–Mn–Fe-стопів в комбінації з електромагнетними показниками

Cu–Al–Mn, цілком вірогідне застосування наноструктурованих композицій в смарт-пристроях, робота яких базуватиметься одночасно на сукупності можливостей актуатора та сенсора. В цьому контексті запропоновані нові підходи до використання функціональних стопів ТМП (СПФ) в якості адаптивних пристроїв із змінною [36] та квазинульовою цупкістю з надпружніми стрижнями із Cu–Al–Mn [37, 38], а також в елементах переміщень [39].

Нова технологічна схема виготовлення СПФ на основі Cu–Al–Mn забезпечує значне поліпшення термосилових показників, підвищення якости та надійности за одночасної інтенсифікації процесу виготовлення їх в середньому в 10–15 раз і приводить до пониження собівартости продукції [40]. Новітні стопи Cu–Al–Mn мають широкий інтервал робочих температур і можуть бути використані під час виготовлення інтеґральних мікросхем, в оптичних навіґаційних приладах, телескопах, оптичних прицілах, далекомірах, проєкційних і знімальних апаратах, спектрометрах, спектрографах [41].

Таким чином, в роботі представлено аналітичне підґрунтя можливостей СПФ на основі стопів міді та наведено експериментальні докази використання їх в якості інтелектуальних матеріялів різноманітного призначення.

4. ВИСНОВКИ

1. Проведено якісну та кількісну оцінку деформаційної поведінки Cu–Al–Mn(Fe)-стопів, яка засвідчила демонстрацію значних деформаційних показників за реалізації ефектів надпружности та ефекту пам’яті форми у відповідних сполуках.
2. Зазначено істотний вплив магнетного поля на електричні властивості під час індукування мартенситного перетворення, які безпосередньо залежать від впливу зовнішнього поля та попереднього термомагнетного оброблення зразків.
3. Оброблення в магнетному полі стопу Cu–Al–Mn приводить до зміни кінетики та морфології за індукування мартенситного фазового перетворення. Можна стверджувати, що за термомагнетного оброблення зразки отримають наведену одновісну магнетну анізотропію або зменшення розмірів феромагнетних частинок.
4. Використовуючи високі механічні показники Cu–Al–Mn–Fe-стопів в комбінації з високими суперпарамагнетними показниками Cu–Al–Mn-стопів, цілком вірогідне застосування таких наноструктурованих композицій у смарт-пристроях, робота яких базуватиметься одночасно на сукупності можливостей актуатора та сенсора.

Роботу виконано в рамках проєкту «Фізичні основи створення матеріалів з керованими магнітоструктурними та термодинамічними характеристиками» (0122U001886) та за часткової підтримки

ґранту SSF Project UKR22-0042.

ЦИТОВАНА ЛІТЕРАТУРА—REFERENCES

1. D. Stoeckel, *Mater. Design*, **11**, No. 6: 302 (1990).
2. J. M. Jani, M. Leary, A. Subic, and M. A. Gibson, *Mater. Design*, **56**, No. 4: 1078 (2014).
3. L. Orgeas and D. Favier, *J. Phys. IV*, **5**, No. 8: 605 (1995).
4. K. Jacobus, H. Sehitoglu, and M. Balzer, *Metall. Mater. Trans.*, **27**, No. 10: 3066 (1996).
5. K. Otsuka and X. B. Ren, *Intermetallics*, **7**, No. 5: 511 (1999).
6. S. Y. Yang, T. Omori, C. P. Wang, Y. Liu, M. Nagasako, J. J. Ruan, R. Kainuma, K. Ishida, and X. J. Liu, *Sci. Rep.*, **6**: 21754 (2016).
7. S. Sugimoto, S. Kondo, H. Nakamura, D. Book, Y. Wang, T. Kagotani, R. Kainuma, K. Ishida, M. Okada, and M. Homma, *J. Alloys Compd.*, **265**, No. 1–2: 273 (1998).
8. Y. Sutou, T. Omori, J. J. Wang, R. Kainuma, and K. Ishida, *Mater. Sci. Eng. A*, **378**, Nos. 1–2: 278 (2004).
9. S. M. Ueland and C. A. Schuh, *Acta Mater.*, **60**, No. 1: 282 (2012).
10. S. Xu, H. Huang, J. Xie, Y. Kimura, X. Xu, T. Omori, and R. Kainuma, *Metals*, **7**, No. 4: 141 (2017).
11. S. Y. Yang, T. Omori, C. P. Wang, Y. Liu, M. Nagasako, J. J. Ruan, R. Kainuma, K. Ishida, and X. J. Liu, *Sci. Rep.*, **6**: 21754 (2016).
12. S. M. Ueland, Y. Chen, and C. A. Schuh, *Adv. Functional Mater.*, **22**, Iss. 10: 2094 (2012).
13. S. Yang, L. Guo, X. Qing, S. Hong, J. Zhang, M. Li, C. Wang, and X. Liu, *Sci. Technol.*, **57**: 43 (2020).
14. Y. Sutou, T. Omori, K. Yamauchi, N. Ono, R. Kainuma, and K. Ishida, *Acta Mater.*, **53**, No. 15: 4121 (2005).
15. T. Omori, T. Kusama, S. Kawata, I. Ohnuma, Y. Sutou, Y. Araki, K. Ishida, and R. Kainuma, *Science*, **341**, No. 6153: 1500, (2013).
16. T. Kusama, T. Omori, T. Saito, S. Kise, T. Tanaka, Y. Araki, and R. Kainuma, *Nature Commun.*, **8**: 354 (2017).
17. K. Otsuka, C. M. Wayman, K. Nakai, H. Sakamoto, and K. Shimizu, *Acta Metall.*, **24**, No. 3: 207 (1976).
18. T. Saburi, Y. Inada, S. Nenno, and N. Hori, *J. Phys. Colloid Chem.*, **43**, No. C4: 633 (1982).
19. R. J. Comstock Jr., T. E. Buchheit, M. Somerday, and J. A. Wert, *Metall. Mater. Trans. A*, **28**, No. 9: 3505 (1997).
20. Y. Sutou, T. Omori, J. J. Wang, R. Kainuma, and K. Ishida, *J. Phys. IV*, **112**, No. 11: 511 (2003).
21. S. Xu, H. Huang, J. Xie, Y. Kimura, X. Xu, T. Omori, and R. Kainuma, *Metals*, **7**, No. 7: 141 (2017).
22. Y. N. Liu, I. Houver, H. Xiang, L. Bataillard, and S. Miyazaki, *Metall. Mater. Trans. A*, **30**: 1275 (1999).
23. Y. Tanaka, Y. Himuro, R. Kainuma, Y. Sutou, T. Omori, and K. Ishida, *Science*, **327**, No. 5972: 1488 (2010).
24. K. Otsuka and C. M. Wayman, *Shape Memory Materials* (Cambridge: Cam-

bridge University Press: 1998), p. 27.
25. T. Omori, N. Koeda, Y. Sutou, R. Kainuma, and K. Ishida, *Mater. Trans.*, **48**, No. 11: 2914 (2005).
26. V. I. Alshits, E. V. Darinskaya, M. V. Koldaeva, and E. A. Petrzhik, *Crystallogr. Rep.*, **48**, No. 5768 (2003).
27. I. R. Bubley, Yu. N. Koval, and P. V. Titov, *Metallofiz. Noveishie Tekhnol.*, **36**, No. 12: 1661 (2014) (in Russian).
28. A. N. Titenko, L. D. Demchenko, A. Ye. Perekos, M. B. Babanli, A. Yu. Gerasimov, and Ya. V. Korenivska, *Metallofiz. Noveishie Tekhnol.*, **42**, No. 4: 531 (2020) (in Russian).
29. M. Robin, G. Lormand, and P. Gobin, *J. Phys. Colloques*, **43**, No. C4: 485 (1982).
30. Yu. N. Koval and A. Y. Molyn, *Fiz. Met. Metalloved.*, **50**, No. 5: 1099 (1980) (in Russian).
31. L. Demchenko, A. Titenko, L. Kozlova, A. Kravets, and M. Babanli, *Proc. of the IEEE 13th Int. Conf. 'Nanomaterials: Applications and Properties' (Sept. 10–15, 2023, Bratislava)*, p. NMM-04.
32. A. Titenko, L. Demchenko, L. Kozlova, M. Babanli, T. Z. Ren, and Ya. Titenko, *Appl. Nanosci.*, **10**, No. 5: 3097 (2020).
33. V. V. Kokorin, L. E. Kozlova, A. O. Perekos, O. M. Babiy, and T. V. Yefimova, *Metallofiz. Noveishie Tekhnol.*, **28**, No. 7: 889 (2006) (in Russian).
34. L. Yang, X. Jiang, H. Sun, Z. Shao, Y. Fang, and R. Shu, *Nanotechnol. Rev.*, **10**: 1560 (2021).
35. J. M. Jani, M. Leary, A. Subic, and M. A. Gibson, *Mater. Design*, **56**: 1078 (2014).
36. A. M. Titenko, L. D. Demchenko, Yu. M. Troshchenkov, V. K. Sulzhenko, and M. B. Babanly, *Sposib Zminennya Zhorstkosti Adaptyvnykh Konstruktsiy z Vykorystannyam Materialiv z Pam'yattyu Formy* [Method for Changing the Rigidity of Adaptive Structures Using Shape Memory Materials], Patent No. 131506 (Published February, 2019) (in Ukrainian).
37. Y. Araki, K. Kimura, T. Asai, T. Masui, T. Omori, and R. Kainuma, *J. Sound and Vibration*, **358**: 74 (2015).
38. W. Chang and Y. Araki, *ICE Proc. Civil Eng.*, **169**, No. 2: 87 (2016).
39. S. Naghashian, B. L. Fox, and M. R. Barnett, *Smart Materials and Structures*, **23**, No. 4: 065002 (2014).
40. Yu. M. Koval, L. M. Nehanov, and A. P. Shpak, *Sposib Vyhotovlennya Porystykh Termochutlyvykh Hradientnykh Elementiv iz Splaviv z Pam'yattyu Formy* [Method for Manufacturing Porous Thermosensitive Gradient Elements from Shape Memory Alloys], Patent of Ukraine No. 11915 (Published January 16, 2006) (in Ukrainian).
41. I. R. Bubliy, Yu. M. Koval, L. M. Nehanov, and T. H. Sych, *Splav na Osnovi Midi z Ehfektom Pam'yati Formy* [An Alloy Based on Copper with Shape Memory Effect], Patent of Ukraine No. 14165 (Published May, 2006) (in Ukrainian).

Metallophysics and Advanced Technologies
Металофіз. новітні технол.
Metallofiz. Noveishie Tekhnol.
2026, vol. 48, No. 5, pp. 513–526
https://doi.org/10.15407/mfint.48.05.0513
Reprints available directly from the publisher

PACS numbers: 61.66.Fn, 61.72.Ff, 65.80.+n, 68.55.J-, 72.15.Jf, 73.50.Lw, 81.15.Cd

Formation of Manganese-Silicide Films by Magnetron Sputtering, Measurement of Crystal Structure, Thermoelectric and Electrophysical Parameters

K. T. Dovranov, M. T. Normuradov, I. R. Bekpulatov,
T. O. Buzrukov*, E. O. Davranov**, R. Yorkulov**, and I. Akbarov

Department of Physics, Karshi State University,
17 Kuchabag Str.,
180119 Karshi, Uzbekistan
**Termez University of Economics and Service,*
4b Farovon Str.,
190111 Termez, Uzbekistan
***University of Economics and Pedagogy,*
45 Do'stlik Str.,
Karshi, Uzbekistan

In this work, thin Mn_4Si_7 films are grown by the solid-state ion-plasma method using a magnetron-sputtering device, and their surface morphology, crystal structure, Miller indices, lattice parameters, thermoelectric and electrophysical parameters of the films are measured. Seebeck coefficient decreases, and finally, the sample is changed from *p*-type to *n*-type. Power factor turns out to be small ($P \cong 1–4$ mW/(m·K^2)) and increases very little in the temperature range of 300–450 K and increases sharply in the range of 500–580 K ($P \cong 850–3690$ mW/(m·K^2)). As the thickness decreases, the power factor increases. The band gap at room temperature for the sample prepared by the ion-plasma method is measured optically to be $E_g = 0.354$ eV. Studies show that Mn_4Si_7 layers with a size of ≤ 40 nm can be grown on the surface of the Si

Corresponding author: Quvondiq Dovranov
E-mail: quvondiqdavronm@gmail.com

Citation: K. T. Dovranov, M. T. Normuradov, I. R. Bekpulatov, T. O. Buzrukov, E. O. Davranov, R. Yorkulov, and I. Akbarov, Formation of Manganese-Silicide Films by Magnetron Sputtering, Measurement of Crystal Structure, Thermoelectric and Electrophysical Parameters, *Metallofiz. Noveishie Tekhnol.*, **48**, No. 5: 513–526 (2026). DOI: 10.15407/mfint.48.05.0513

crystal formed by the magnetron sputtering, but the Si crystal does not form a full-size Mn_4Si_7 layer. During thermal heating at 300–750 K, nanosize bubbles are observed to form in the thin Mn_4Si_7 coating grown under vacuum conditions; then, they are ruptured and the nanosize defects are formed. Then, at 750 K, the defects narrow down to form a single thin Mn_4Si_7 coating. The measurement results show that the thin films grown by the solid-state ion-plasma method are formed and their thermoelectric and electrophysical properties are improved.

Key words: Miller indices, interplanar distance, strict monocrystalline structure, Seebeck coefficient, power factor.

У даній роботі методою твердотільної йонної плазми з використанням пристрою магнетронного розпорошення вирощено тонкі плівки Mn_4Si_7 та виміряно морфологію їхньої поверхні, кристалічну структуру, Міллерові індекси, параметри ґратниці, термоелектричні й електрофізичні параметри плівок. Зеєбеків коефіцієнт зменшився, і зрештою тип зразків змінився з p-типу на n-тип. Коефіцієнт потужности виявився малим ($P \cong 1$–4 мВт/(м·К^2)) та дуже слабо збільшувався в діяпазоні температур 300–450 К і різко зростав у спостережуваному нами діяпазоні 500–580 К ($P \cong 850$–3690 мВт/(м·К^2)). Зі зменшенням товщини збільшується коефіцієнт потужности. Ширину забороненої зони за кімнатної температури для зразка, виготовленого йонно-плазмовою методою, було виміряно оптично, що становило $E_g = 0{,}354$ еВ. Дослідження показали, що шари Mn_4Si_7 розміром у ≤ 40 нм можуть бути вирощені на поверхні кристалу Si, утвореного магнетронним розпорошенням, але кристал Si не утворює повнорозмірний шар Mn_4Si_7. Під час термічного нагрівання за 300–750 К спостерігалося утворення нанорозмірних бульбашок у тонкому покритті Mn_4Si_7, вирощеному в умовах вакууму, а потім вони розривалися й утворювалися нанорозмірні дефекти. За 750 К дефекти звужуються, утворюючи єдине тонке покриття Mn_4Si_7. Результати мірянь свідчать про формування тонких плівок, вирощених методою твердотільної йонної плазми, та поліпшення їхніх термоелектричних і електрофізичних властивостей.

Ключові слова: Міллерові індекси, міжплощинна віддаль, чітка монокристалічна структура, Зеєбеків коефіцієнт, коефіцієнт потужности.

(Received 15 March, 2025; in final version, 2 July, 2025)

1. INTRODUCTION

High manganese silicide (HMS) is one of the promising materials for use in the field of silicon microelectronics [1]. Based on HMS films, it is possible to create infrared thermal radiation detectors. Detectors can record data into memory devices and measure fast processes associated with data transmission through various channels. In addition, it is possible to create light sources at significant wavelengths in the infrared range [2–4]. Therefore, studying the growth and electrical properties of HMS films is of great interest.

There is ion implantation, molecular beam epitaxial, ion plasma and chemical methods for producing thin films. Thin films obtained by the ion plasma method are practically not found in previously published literature, and this method can be called new. The ion plasma method was created by ionizing argon gases under high vacuum conditions.

Of all the silicon compounds that have thermoelectric efficiency, it is possible to select compounds that are of practical importance. These are, for example, solid solutions based on cobalt monosilicide (CoSi), higher manganese silicide ($MnSi_{1.7}$) and Mn_2X (X = Si, Ge, Sn). There is little data on the thermoelectric properties of Mn_4Si_7 materials [5, 6]. The high Seebeck coefficient, low resistance and high application temperature make them very attractive for power generation [7, 8]. However, the thermoelectric properties of n-type Mn_4Si_7 films have rarely been reported. We developed and characterized n-type polycrystalline Mn_4Si_7 thin films to understand the basic thermoelectric properties of the movie.

When preparing the sample, a ready-made Mn_4Si_7 target, heated and compacted, was used. Pure silicon with the crystal direction [111] was taken as a substrate. First, the silicon surface was cleaned of surface impurities using an 'ion gun' device in a vacuum. The purified sample was heated to 1720 K for 2 hours. Then, using argon gases under high vacuum conditions, 'ion plasma' was created from a manganese silicide target and thin films of Mn_4Si_7 of various thicknesses were obtained. The electrical conductivity and Seebeck coefficient of the resulting thin films were measured using a 'Netzch®SBA 458' measuring instrument.

Research shows that Mn_4Si_7 layers ≤ 40 nm in size can be grown on the surface of a Si crystal produced by magnetron sputtering, but the Si crystal does not form a full-size Mn_4Si_7 layer. During thermal heating at 300–750 K, the appearance of nanosize bubbles in a thin Mn_4Si_7 coating grown under vacuum conditions was observed; then, they burst and formed nanosize defects. Then, at a temperature of 750 K, the defects narrowed and formed a single thin Mn_4Si_7 coating (Fig. 1).

The surface morphology of Mn_4Si_7 crystals was studied under a microscope (Scios FEI, Quanta 200 3D). The surface morphology of Mn_4Si_7 was studied using an SPM 9700HT scanning probe microscope. For this purpose, a sample area measuring 500×500 nm was selected, lines were drawn on this area in one arbitrary direction, and the thickness of their full width was determined.

2. EXPERIMENTAL/THEORETICAL DETAILS

Polycrystalline HMS thin films were prepared using a magnetron sputtering system. A schematic diagram of the magnetron sputtering system used in this work is presented in Fig. 2. A high vacuum was created at a pressure of 10^{-6} Torr using a molecular turbo-pump (Pfeiffer

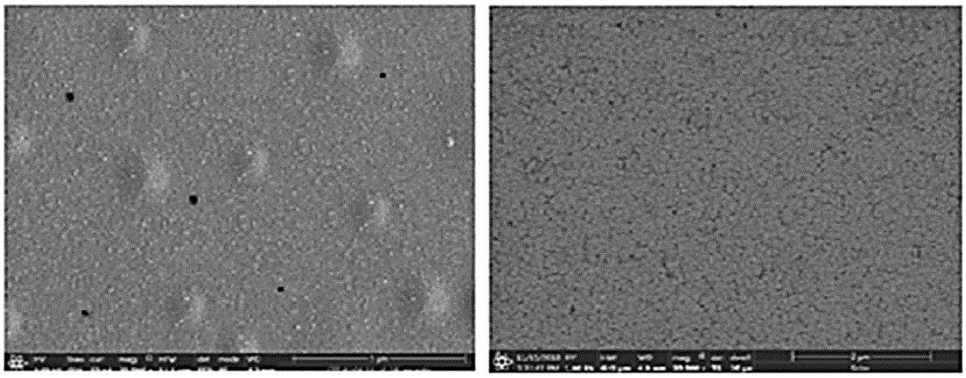

Fig. 1. Image of a thin Mn_4Si_7 film before and after heating to 300–750 K.

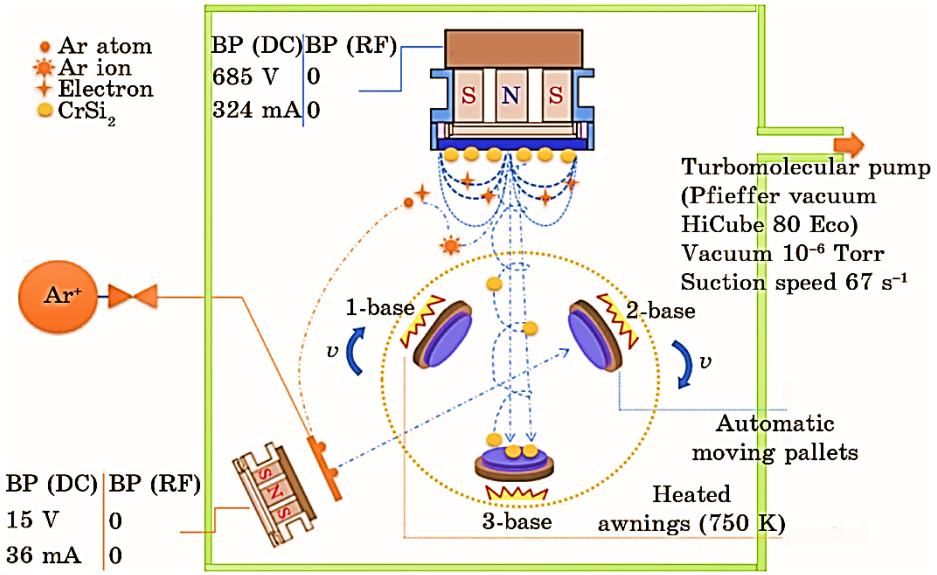

Fig. 2. Scheme of a magnetron-sputtering device.

vacuum) in the chamber of the Epos-PVD-Desk-Pro magnetron device for sputtering the Mn_4Si_7 target. First, the surface of the silicon wafers was mechanically cleaned with 20% dilute hydrofluoric acid, then the silicon surface was cleaned again by ionizing argon gas inside the chamber using an 'ion gun' treatment device installed in the chamber. A direct current source was used to sputter the Mn_4Si_7 target. The current in the magnetron power supply is of 657 mA, power is of 221 W, and voltage is of 336 V. The purity of the Mn_4Si_7 target is of 99.9%.

The deposition rate varies from 0.4 to 14 Å/s. The thickness of each

layer was controlled on an 'SP307' monitor.

The electrical parameters of a thin layer of Mn_4Si_7 samples with a thickness of approximately 34.7–172 nm was studied on an ECOPIA instrument (HMS-5000). The surface morphology was analysed using atomic force microscopy. Structural analysis of the Mn_4Si_7 crystal was recorded on an XRD-6100 x-ray diffractometer; spectra were recorded at room temperature. Spectrogram peaks based on Miller indices and interplanar distances indicate newly formed manganese silicide compounds. The thermoelectric parameters of manganese silicide were measured using the 'SBA-458' measuring system. This setup allows you to measure the Seebeck coefficient and electrical conductivity as a function of temperature. The diagram of the measuring cell is shown in Fig. 3.

The sample is placed on the ceramic supports, inside of which microheaters are located. Two thermocouples and two current probes are connected to the bottom surface of the sample. Electrical conductivity is measured by the four-point method. This scheme allows current to flow through the sample in the forward and reverse directions. During the measurement, three current values are passed in each direction: I_{max}, $2I_{max}/3$, $I_{max}/3$. The value of I_{max} is selected based on the geometry and material of the sample. The program determines three current values, and applies each sample to the sample five times in the forward direction and five times in the opposite direction. Next, the voltage values U_A and U_B are measured between two positive and two negative thermocouple branches. Based on the measurements, a graph of voltage dependence on the missed current is plotted, and the electrical conductivity is calculated.

To measure the Seebeck coefficient using two microheaters inside the sample, a temperature gradient is created. After heating one side

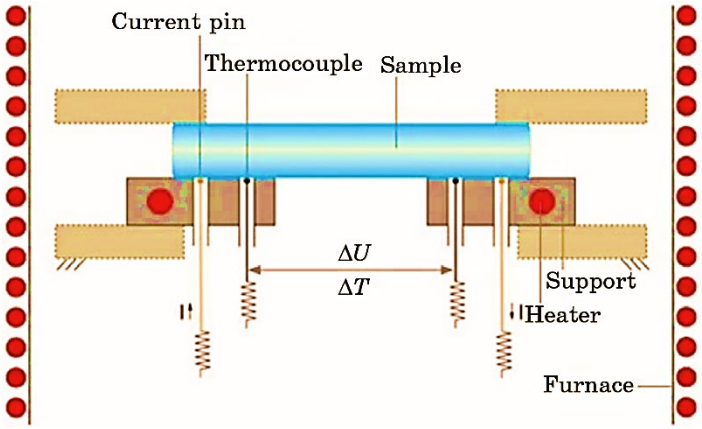

Fig. 3. Diagram of the SBA-458 Nemesis® measuring cell.

of the sample, it cools. Then, the other side of the sample is also heated and cooled. During this whole process, the values of the voltages U_A, U_B and U_{T1}, U_{T2} are measured. As for electrical conductivity, U_A and U_B are the voltages between the positive and negative branches of thermocouples. These values are measured concerning the temperature difference ΔT, which is the temperature gradient between the two sides of the sample. The value of ΔT is determined from the voltages U_{T1} and U_{T2}, coming from two thermocouples. Based on the measurement data, a graph of voltage versus temperature is plotted and the Seebeck coefficient is calculated. In this case, it is of ± 2 degrees from the point given by the operator.

The efficiency of thermoelectric materials is determined by a dimensionless quantity called the thermoelectric index [14]:

$$ZT = \sigma\alpha^2\tau/\lambda, \tag{1}$$

where σ is the electrical conductivity of the material, λ is the thermal conductivity, α is the Seebeck coefficient, and T is temperature. A material with $ZT = 1$ at room temperature is considered effective. As can be seen in formula (1), if there is the higher the quality factor, there is the higher the thermal conductivity and electrical conductivity of the material [15]. These parameters are directly related to the electronic properties of the material and, for convenience, include power factor. The thermoelectric power factor characterizes the ability of a thermoelectric generator to generate electrical energy in an external circuit and is defined as:

$$P = \sigma\alpha^2.$$

3. RESULTS AND DISCUSSION

3.1. Surface Morphology and Crystal Structure of Mn_4Si_7 Thin Films

Figure 4 shows a 3*D* image of a manganese silicide nanofilm grown by magnetron sputtering, obtained using an atomic force microscope. The average roughness height of the HMS film is $r_z = 34.7$ nm, and the surface is completely covered with a peak. Figure 5 shows a 2*D* image of a Mn_4Si_7 nanofilm. Moreover, if we take images in only two dimensions, we see that we cannot easily discern differences in surfaces. The height of the islands is more visible in 3*D*. In both cases, evenly distributed waves are generated under the surface over large areas. This means that the thin surface layer is manganese silicide. AFM analysis shows that evidence of formation is a nanosize film obtained by the ion-plasma method. Figure 6 shows the formation profile of a manganese silicide nanofilm grown by the solid-phase ion plasma method in a

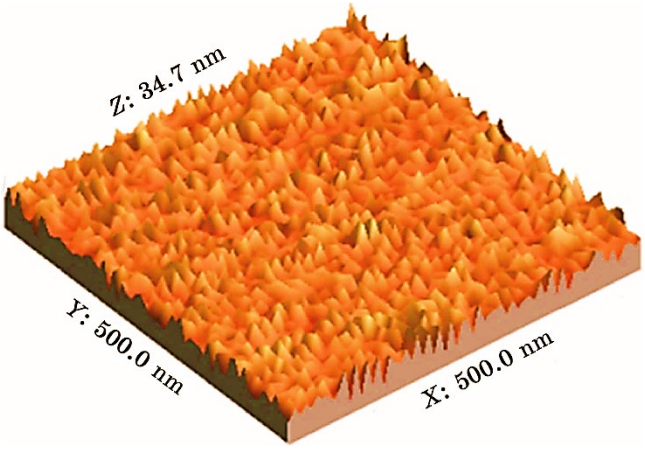

Fig. 4. 3*D* images of the surface of thin Mn_4Si_7 films obtained by atomic force microscopy.

magnetron sputtering device.

The qualitative composition of a thin film of manganese silicide, the crystal structure of the substance, as well as the arrangement of atoms in the unit cell have been determined. The texture of polycrystalline materials has been studied. In addition, the phase composition of the substance, phase diagrams, crystal sizes in the sample, radiation CuK_α (β-filter, Ni, $\lambda = 1.54178$ Å, current and voltage mode—30 mA, 40 kV) and constant rotation speed of the detector were assessed 0.05 degrees

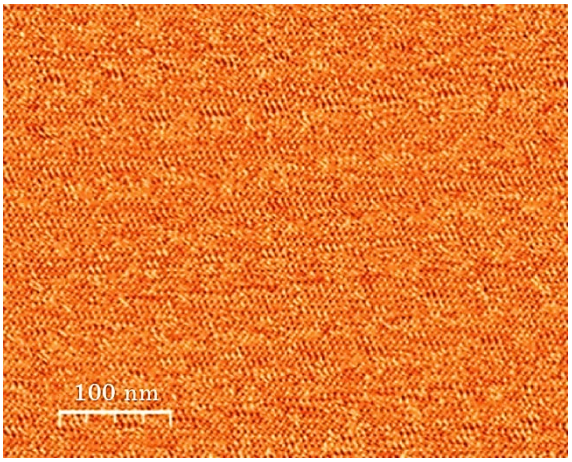

Fig. 5. 2*D* images of the surface of thin Mn_4Si_7 films obtained by atomic force microscopy.

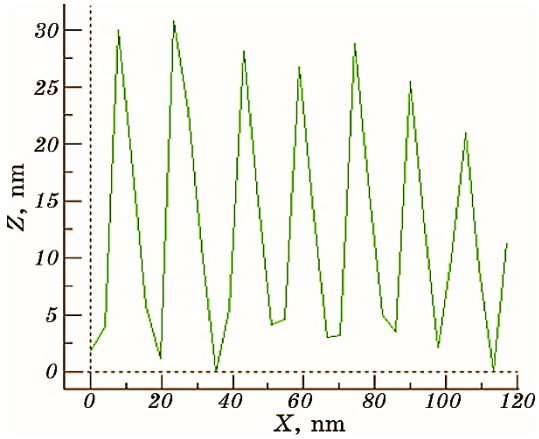

Fig. 6. Profile along the selected direction.

in steps of 4 degrees/min. The x-ray power was 2 kW. The results were analysed using a database. The penetration depth of radiation CuK_α is about 1 mm (980 μm) for light elements (carbon) and several microns for heavy elements (Ag, Pt). For most inorganic substances, CuK_α is tens of microns (μm) for simple compounds.

Figure 7 shows the spectral dependences obtained using the Mn_4Si_7 diffractometer method. In addition, Miller indices are given. We used the Rietveld method to refine the structure from x-ray data [9–11]. The principle of the method is to use independent intensity measurements at each point of the diffraction pattern to describe the line profile using analytical functions instead of using the integrated reflection intensity. Object parameters, including structural, hardware and other characteristics, are refined using the nonlinear least squares

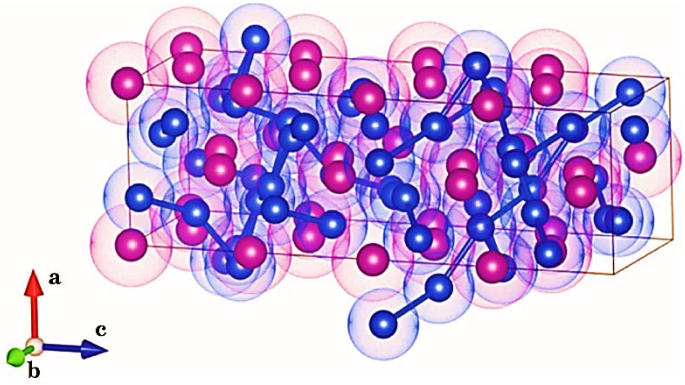

Fig. 7. Crystal structure (tetragonal structure, space group $Pm3m$).

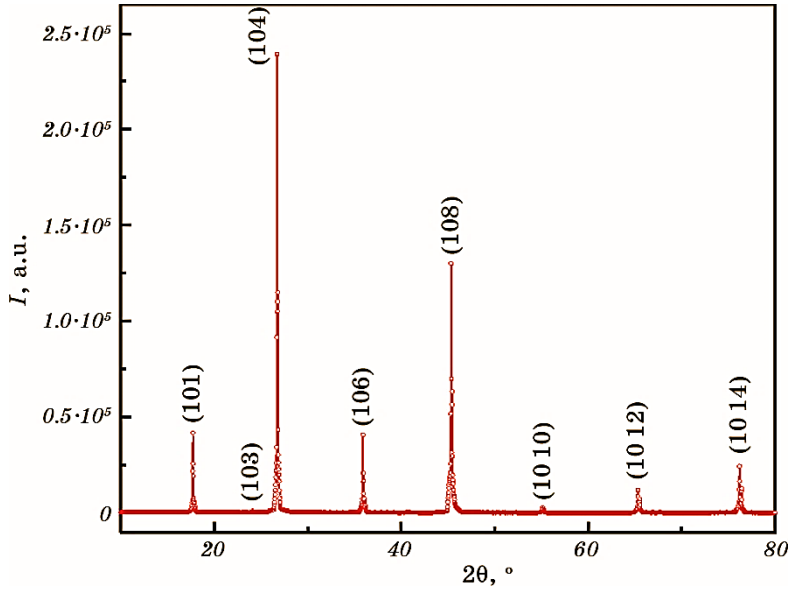

Fig. 8. X-ray diffraction pattern of Mn_4Si_7 crystal.

TABLE 1. Type and lattice parameters of silicide films.

Silicide	In this work	
	Grille type	Lattice parameters, Å
Si	Cubic	$a = 5.45$
$CoSi_2$ [5]	Cubic	$a = 5.40$
Mn_4Si_7	Tetragonal	$a = 5.7$, $c = 15.3$

method. Using this refinement method, we determined the Miller indices (*hkl*). As mentioned above, x-ray diffractometry of polycrystalline films allows quantitative elemental analysis.

Figure 8 shows x-ray diffraction analysis and spectral dependences of a thin film of manganese silicide. XRD analysis at room temperature shows that peaks 17.292, 27.412, 36.321, 45.842, 55.792, 65.247 and 77.634 are visible from several angles. The main ideal peak appears at an angle of 27.412 degrees (104).

When heated to 700 K, the angle of the peaks in the image does not change, but the intensity does. The release of some light volatile elements during heating and crystallization can be explained by the crystallization of the sample. The x-ray phase analysis method presented in the literature [12, 13] shows that in a sample heated to 800 K, x-ray phase analysis peaks appear at certain angles, although the peaks are

very small in intensity and contrast.

3.2. Measurement of Electrophysical and Thermoelectric Properties of Samples

The electrical parameters of manganese silicide films of various thicknesses deposited on the surfaces of silicon and glass by the ion-plasma method in high vacuum were measured on an ECOPIA instrument (HMS-5000), and comparative data on the electrical parameters of thin Mn_4Si_7 coatings are presented (Table 2). Figure 9 shows the tempera-

TABLE 2. Mn_4Si_7 film deposited on glass (1), Mn_4Si_7 film deposited on silicon (2).

Measurements	Mn_4Si_7 coated on glass surface (1)	Mn_4Si_7 coated on silicone surface (2)
Resistivity, Ω·cm	$4.1678 \cdot 10^{-3}$	$1.2453 \cdot 10^{-3}$
Resistance, Ω	612	454
Average Hall coefficient, cm^3/C	$5.7642 \cdot 10^{-2}$	$2.8979 \cdot 10^{-5}$
Conductivity, S/cm	239.94	802.99
Sheet concentration, cm^{-2}	$3.2488 \cdot 10^{15}$	$2.2036 \cdot 10^{18}$
Bulk concentration, cm^{-3}	$1.0829 \cdot 10^{20}$	$2.1541 \cdot 10^{23}$
Mobility, $cm^2/(V \cdot s)$	13.83	$2.327 \cdot 10^{-2}$
Sheet resistance, Ω/	138.93	121.74
A–C Hall coefficient, cm^3/C	$1.4251 \cdot 10^{-1}$	$2.9439 \cdot 10^{-5}$
B–D Hall coefficient, cm^3/C	$-2{,}7224 \cdot 10^{-2}$	$2.8519 \cdot 10^{-5}$
Ratio vertical/horizontal	0.77849	0.97469

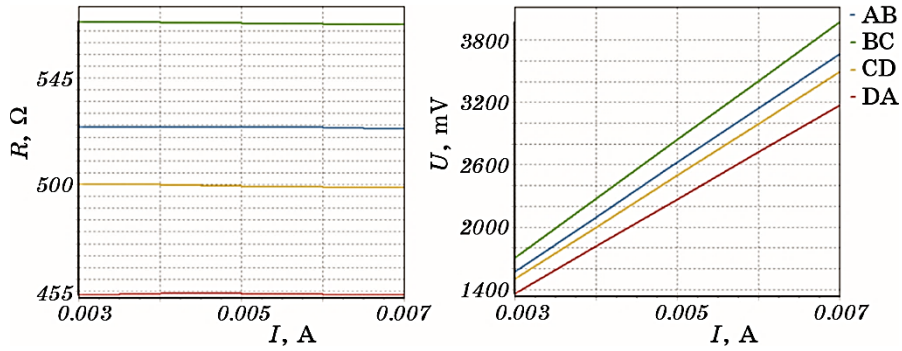

Fig. 9. Electrophysical parameters of Mn_4Si_7 thin films (resistance *vs.* current and *I*–*U* curve).

ture dependence of I–U curve and the electrical resistance of the samples.

The MnSi film deposited on a silicon substrate with a resistivity of 3–5 Ω·cm had an n-type and the Seebeck coefficient was close to –140 μV/K. The thickness of the films was about 146 nm. The resistance decreased with increasing temperature. However, the relationship between resistance and temperature was very complex due to the shrinkage effect of the substrate. The figures show the temperature dependences of the electrical conductivity and Seebeck coefficient of thin Mn_4Si_7 films of various thicknesses grown in ion-plasma oats (Fig. 10).

With increasing temperature, the resistivity first decreased from 124 to 118 mΩ·cm, increased slightly after 400 K, and then, sharply decreased. This behaviour indicates that Mn_4Si_7 is a semiconductor. Due to the average crystallinity of the film, the Seebeck coefficient was not very low.

The Seebeck coefficient of the film with an initial thickness of 172 nm was larger than that of sample-1, but the Seebeck coefficient increased faster after 560 K, which can be attributed to the crystallinity of the film thickness.

The resistivity of the sample deposited on the silicon surface was about 9.88 mΩ·cm at room temperature. With increasing temperature, the electrical conductivity increased slightly and then increased sharply above 530 K. The film was p-type at room temperature and n-type after 460 K. Near the Mn_4Si_7/Si interface, the silicon substrate heavily doped with manganese is n-type, and the donor state has separated from the conduction band with the energy level. We can say that $E_d = 0.354$ eV.

At temperatures above 580 K, the resist is thermally activated with apparent activation energy of 0.492 eV. If we take the activation ener-

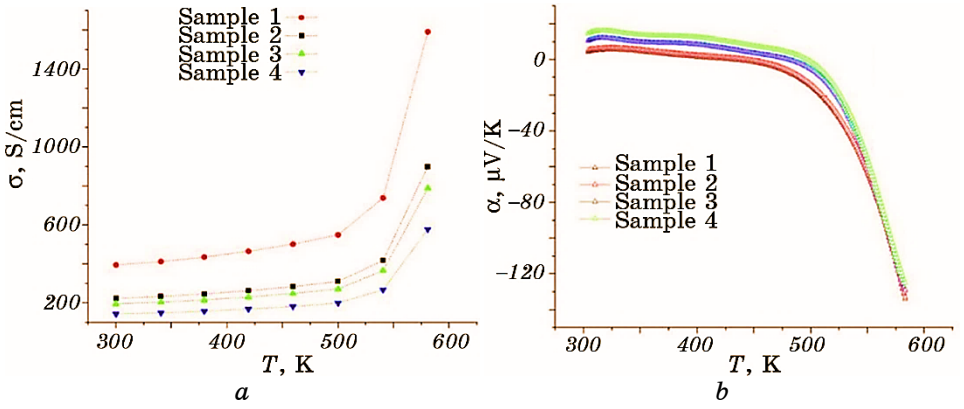

Fig. 10. Temperature dependence of electrical conductivity and Seebeck coefficients.

gy of the material in this intrinsic region to be half the forbidden energy gap, this indicates an estimated energy gap of about 0.984 eV:

$$E_g = E_g(0) \pm \beta\tau, \tag{2}$$

where E_g is the energy band gap, T is the temperature, then the coefficient $\beta = dE_g/dT = -0.80 \cdot 10^{-4}$ eV/K [16]. The Seebeck coefficient is −1.32 μV/K at 300 K and −136 μV/K at 530 K, respectively. With increasing temperature, the concentration of electrons excited from the donor state to the conduction band increases. As a result, the Seebeck coefficient decreases and finally the sample changes from *p*-type to *n*-type. For the sample prepared by the ion plasma method, the band gap at room temperature was $E_g = 0.354$ eV, measured by the optical method.

Figure 11 shows the power factor as a function of temperature for samples of four different thicknesses. As a result of measurements, the power factor turned out to be small ($P \cong 1$–4 mW/(m·K²)) and increased very little in the temperature range of 300–450 K and increased sharply in the range of 500–580 K ($P \cong 850$–3690 mW/(m·K²)). As the thickness decreases, the power factor increases. Using the magnetron sputtering method, a Mn_4Si_7 film with a resistivity of $1.24 \cdot 10^{-3}$ Ω·cm was obtained at room temperature. The power factor reached 3684 μW/(m·K²) at 575 K. Due to this high-power factor, the *n*-type HMS material can outperform the *p*-type HMS material in the development of thermoelectric generators.

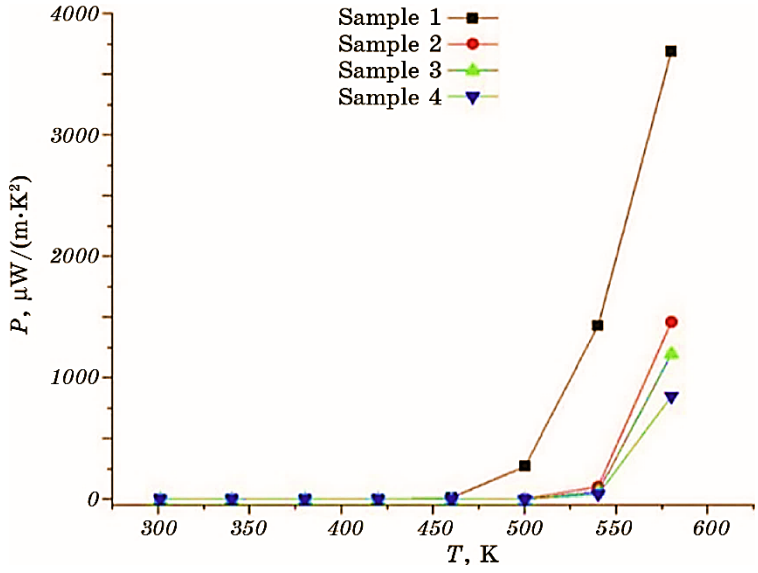

Fig. 11. Power factor dependence on temperature.

4. CONCLUSION

A film of high-manganese silicide of various thicknesses was grown on the surface of a silicon crystal in a magnetron sputtering installation using the solid-phase ion-plasma method. The surface morphology of Mn_4Si_7 crystals depending on their state was studied using a Quanta 200 3*D* microscope (Scios FEI). The electrical parameters of a thin layer of Mn_4Si_7 samples with a thickness of approximately 34.7–172 nm were studied on an ECOPIA device (HMS-5000). Structural analysis of the Mn_4Si_7 crystal was recorded on an XRD-6100 x-ray diffractometer; spectra were recorded at room temperature. Spectrogram peaks based on Miller indices and interplanar distances indicate newly formed manganese silicide compounds. As a result of the research, it was established that the electrical properties of Mn_4Si_7 coatings grown on the surface of glass and silicon by magnetron sputtering are higher on silicon. It has been established that when a Mn_4Si_7 nanocluster is heated and cooled, the Seebeck coefficient changes from –1.32 μV/K to –140 μV/K depending on the order of the nanolayer and the thickness of the coating, and the resistance of the coating decreases upward up to 1.5 times. As a result of the analysis of the measured thermoelectric properties, we concluded that the 'ion-plasma' method is a more effective method for producing high-quality thermoelectric materials. The resulting films can be used in sensors for IR and UV detectors.

REFERENCES

1. M. T. Normuradov, I. R. Bekpulatov, V. V. Loboda, B. D. Donaev, and I. Kh. Turapov, *J. Phys. Math.*, **16**: 78 (2023).
2. B. D. Igamov, G. T. Imanova, A. I. Kamardin, and I. R. Bekpulatov, *Bulletin of the Karaganda University. Series 'Physics'*, No. 3 (111): 50 (2023).
3. B. B. Pitarch, J. P. Gonjal, A. Powell, P. Ziolkowski, and J. G. Canadas, *J. Applied Phys.*, **124**, No. 2: 025105 (2018).
4. C. L. Shen, S. M. Yang, and K. C. Lu, *Nanomaterials*, **10**, Iss. 9: 1880 (2020).
5. K. T. Dovranov, M. T. Normuradov, Kh. T. Davranov, and I. R. Bekpulatov, *Ukrainian J. Phys.*, **69**, No. 1: 20 (2024).
6. D. Y. N. Truong, *Thermoelectric Properties of Higher Manganese Silicides* (Disser. for PhD in Chemistry) (Waterloo: 2015).
7. S. Choia, K. Kuboa, N. Uchiyamaa, and T. Takeuchi, *J. Alloys Compd.*, **921**: 166104 (2022).
8. Q. R. Hou, W. Zhao, Y. B. Chen, and Y. J. He, *Int. J. Modern Phys. B*, **23**, No. 16: 3331 (2009).
9. M. Yu. Tashmetov, F. K. Khallokov, N. B. Ismatov, I. I. Yuldashova, I. Nuritdinov, and S. Kh. Umarov, *Physica B: Cond. Matter*, **613**: 412879 (2021).
10. S. K. Umarov, I. Nuritdinov, Z. Z. Ashurov, and F. K. Khallokov, *Techn. Phys.*, **64**: 183 (2019).

11. M. T. Normuradov, Sh. T. Khozhiev, K. T. Dovranov, Kh. T. Davranov, M. A. Davlatov, and F. K. Khollokov, *Ukrainian J. Phys.*, **68**, No. 3: 210 (2023).
12. L. Smrcok, V. Langer, M. Halvarsson, and S. Ruppi, *J. Crystallography*, **216**, Iss. 7: 409 (2001).
13. K. Dovranov, M. Vinnichenko, A. Kodirov, M. Normuradov, M. Davlatov, J. Parmonov, Kh. Davranov, D. Nabiyev, and N. Kurbonov, *2024 Int. Conf. Electrical Eng. Photonics (EExPolytech) (Oct. 17–18, 2024)* (Saint Petersburg: 2024), p. 308.
14. I. V. Erofeeva, M. V. Dorokhin, V. P. Lesnikov, Yu. M. Kuznetsov, A. V. Zdoroveishchev, and E. A. Pitirimova, *XXI Int. Symp. 'Nanophysics and Nanoelectronics' (March 13–16, 2017)* (Nizhny Novgorod: 2017), p. 1403.
15. Q. R. Hou, W. Zhao, Y. B. Chen, D. Liang, X. Feng, H. Y. Zhang, and Y. J. He, *Appl. Phys. A*, **86**: 385 (2007).
16. Z. M. Wang, Q. R. Hou, and Y. J. He, *Appl. Phys. A*, **80**: 1807 (2005).

Metallophysics and Advanced Technologies
Металофіз. новітні технол.
Metallofiz. Noveishie Tekhnol.
2026, vol. 48, No. 5, pp. 527–536
https://doi.org/10.15407/mfint.48.05.0527
Reprints available directly from the publisher

PACS numbers: 07.10.Cm, 62.20.de, 62.25.-g, 73.40.Gk, 73.40.Rw, 77.55.+f, 81.70.Bt

Young's Modulus of Sub-10 nm MgO Films *via* the Tunnelling-Current Nanoindenter Method

V. O. Burlakov and O. V. Filatov

G. V. Kurdyumov Institute for Metal Physics, N.A.S. of Ukraine,
36 Academician Vernadsky Blvd.,
UA-03142 Kyiv, Ukraine

A novel method for determining the elastic properties of ultrathin dielectric films based on conductive-tip nanoindentation is applied. The approach enables the extraction of film deformation from variations in tunnelling current, thereby, eliminating contributions from the substrate, indenter, and instrument compliance. A 6 nm MgO film deposited on a Fe film is investigated as a model system. The load–displacement curve is calculated from the obtained data of tunnel current, allowing evaluation of the Young's modulus. The measured modulus of the MgO film is of ≅ 180 GPa, which is lower than bulk values and is attributed to reduced density and structural features of the deposited film. Repeated indentation results in an apparent increase in the Young's modulus up to ≅ 380 GPa, associated with densification and reduced porosity. The applied method provides a high-resolution approach for measuring the mechanical properties of dielectric films with thicknesses below 10 nm.

Key words: nanofilms, Young's modulus, mechanical properties, magnesium oxide MgO, nanoindentation, tunnelling current.

Застосовано новий метод визначення пружніх властивостей надтонких діелектричних плівок на основі наноіндентування провідним вістрям. Цей підхід уможливлює виокремити деформацію плівки за зміною тунельного струму, тим самим усуваючи внески від підкладинки, індентора та

Corresponding author: Viktor Oleksandrovych Burlakov
E-mail: odinpwnzpacan@gmail.com

Citation: V. O. Burlakov and O. V. Filatov, Young's Modulus of Sub-10 nm MgO Films *via* the Tunnelling-Current Nanoindenter Method, *Metallofiz. Noveishie Tekhnol.*, **48**, No. 5: 527–536 (2026). DOI: 10.15407/mfint.48.05.0527

податливости приладу. Плівка MgO товщиною у 6 нм, нанесена на плівку Fe, досліджується як модельна система. Крива навантаження–зміщення розраховується на основі одержаних даних стосовно тунельного струму, що дає змогу оцінити модуль Юнґа. Виміряний модуль плівки MgO становить ≅ 180 ГПа, що нижче за об'ємні значення та може бути пов'язано з пониженням густини та структурними особливостями нанесеної плівки. Повторне індентування приводить до помітного збільшення модуля Юнґа до ≅ 380 ГПа, що пов'язане з ущільненням і пониженням пористости. Застосований метод забезпечує дієвий підхід для міряння механічних властивостей діелектричних плівок товщиною менше 10 нм.

Ключові слова: наноплівки, модуль Юнґа, механічні властивості, оксид Маґнію MgO, наноіндентування, тунельний струм.

(Received 10 April, 2026; in final version, 20 April, 2026)

1. INTRODUCTION

Ultrathin dielectric films and multilayers with thicknesses below 10 nm are central to nanoelectronic, spintronic, and quantum technologies [1, 2]. Continued miniaturization of high-frequency devices and next-generation CMOS systems requires dielectric layers only a few atomic layers thick to achieve high capacitance and low power consumption [3]. In such architectures, mechanical integrity is critical, as the films must withstand stresses induced by thermal expansion mismatch and applied electric fields without fracture or delamination [4, 5].

Beyond their electronic functionality, ultrathin films are also crucial for nanoelectromechanical systems (NEMS), where elastic deformation and dynamic response are determined by mechanical properties. Device miniaturization enhances sensitivity, enabling subfemtometer-displacement resolution and zepto-scale mass and force detection [6–9].

Consequently, understanding the thickness dependence of elastic properties at the nanoscale is of fundamental and technological importance. At these scales, surface and dopant effects become dominant, leading to mechanical properties that can deviate significantly from bulk properties, exhibiting either softening or stiffening [10]. Thickness-dependent elasticity primarily arises from the high proportion of surface atoms, which may decrease stiffness since surface atoms have less restrictions on their movement [11] or increase it through electron charging redistribution and bond contraction [12, 13]. These effects have been both analysed (using continuum and atomistic approaches [13–16]) and confirmed experimentally [16, 17].

Within the field of green electronics called spintronics, in which magnetic tunnel junctions incorporating an MgO barrier layer serve as

key components in magnetic memory devices, magnetic sensors, radio-frequency and microwave applications, as well as logic and non-Boolean devices [18–20]. MgO seems to be one of the best candidates for use as a barrier layer due to its high dielectric constant and wide band gap. In addition, its cubic crystal structure ensures a relatively low lattice mismatch with many metals and semiconductors [21]. MgO thin films used as barrier layers enable high tunnelling magnetoresistance ratios *via* coherent spin-polarized tunnelling [22]. Therefore, MgO is selected as a model system for the present study, since the determination of its Young's modulus is essential for evaluating the mechanical stability and reliability of ultrathin barrier layers in nanoscale electronic and spintronic devices.

2. EXPERIMENTAL DETAILS

Accurate determination of the elastic properties of ultrathin films remains experimentally challenging, as most conventional techniques lack sufficient sensitivity for thicknesses below 10 nm [23, 24]. Commonly employed methods, such as nanoindentation, typically provide reliable characterization for films with thicknesses on the order of several hundred nanometres, particularly when combined with advanced modelling [25, 26].

To solve this problem, a novel approach to determining the mechanical properties of ultrathin dielectric films is presented. In this method, a conductive tip replaces the traditional diamond tip. The dielectric film under investigation is deposited onto a conductive substrate, and a constant potential difference is applied between the tip and the substrate (Fig. 1).

The current flowing through the tip–dielectric–substrate system is continuously monitored during the indentation process. Variations in the tunnel current result from changes in the dielectric film's thickness and defect mobility under applied load. By analysing these changes, a load–displacement curve is calculated, providing insights into the mechanical behaviour of the dielectric film.

The indenter is fabricated from hardened steel and is characterized by a truncated conical geometry with a tip area of $A \cong 4.8 \cdot 10^{-9}$ m^2. Prior to the measurements, the applied load is calibrated using standard reference weights. The corresponding calibration data are obtained by several measurements.

The dielectric film is a 6 nm thick MgO layer deposited under vacuum conditions onto a 100 nm thick Fe film. The tunnelling current between the tip and the underlying Fe film is measured using the electrical circuit shown in Fig. 1. A Zener diode is employed to maintain a constant bias voltage of 0.7 V. The tunnelling current is determined from the voltage drop across the reference resistor, allowing for quan-

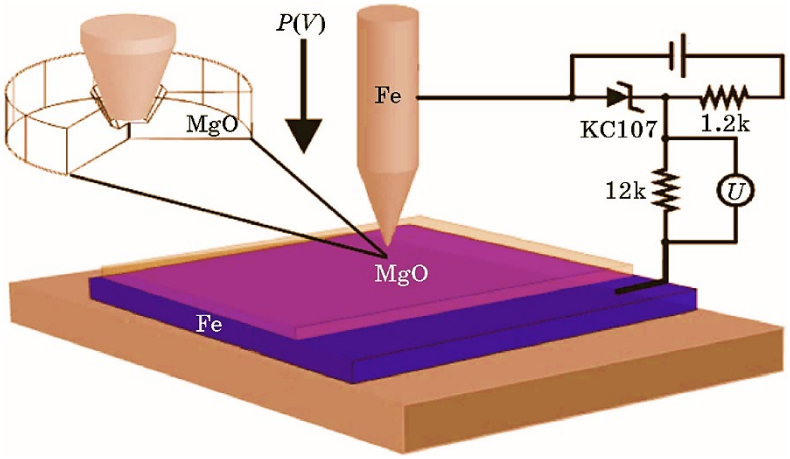

Fig. 1. Schematic representation of the tunnelling current nanoindenter method: a constant bias voltage is applied between the conductive indenter and the substrate, while the tunnelling current through the tip–dielectric–substrate system is monitored during loading to determine the deformation of the dielectric film.

titative analysis during indentation. The change in dielectric thickness under applied load from the tip is inferred from the corresponding variation in the tunnelling current.

3. RESULTS AND DISCUSSION

Reduced atomic co-ordination near a free surface leads to charge redistribution and changes in bonding, resulting in elastic properties that differ from those of the bulk material. While the surface region is only a few atomic layers thick and can be neglected in micron-scale structures, its influence becomes significant at the nanoscale because of the increased surface-to-volume ratio. As a result, the overall stiffness of a nanoscale film cannot be accurately described using the bulk modulus. In this context, the concept of an effective modulus is used to characterize the averaged mechanical response of a structurally inhomogeneous system. Nanoscale films must be regarded as inhomogeneous, since surface regions contribute substantially to their elastic behaviour. Consequently, the effective modulus becomes size-dependent and deviates from the corresponding bulk value [27, 28].

The Young's modulus determined by indentation is typically evaluated using the load–displacement (P–h) curve [29]. The indenter displacement under loading is influenced by the deformation of the film, the substrate, the indenter, and the instrument itself. This complicates the isolation of the film deformation contribution to the total

displacement h. When a conductive indenter is employed, the displacement (h_f) associated with the deformation of the dielectric film is determined from variations in the tunnelling current. At room temperature, the tunnelling current exhibits an approximately exponential dependence on the applied voltage. At low voltages (up to $\cong 0.3$ V) [30], thermal fluctuations significantly affect the current, introducing a source of error in the exponential approximation of the current–voltage relationship.

The exponential dependence of the tunnelling resistance provides high resolution in determining variations in the dielectric thickness. Under loading with a conductive indenter tip, the electrical resistance of the system is observed to vary in the range from 10 MΩ to 1 kΩ as the dielectric thickness decreases from 5 nm to 1 nm. The contact resistance between the indenter tip and the metallic film, without the dielectric film, is approximately 100 Ω and decreases linearly with increasing contact area. Its influence on the total tunnelling current is therefore negligible. Consequently, the displacement (h_f) calculated from variations in the tunnelling current I enables the determination of the dielectric deformation, while excluding contributions from the deformation of the substrate, the indenter, and the instrument.

During the experiment, the voltage across a reference resistor connected in series with the sample is monitored. Variations in the dielectric thickness affect both the current I in the circuit and the voltage U_f across the sample (Fig. 2). In Ref. [31], a series of I–U characteristics

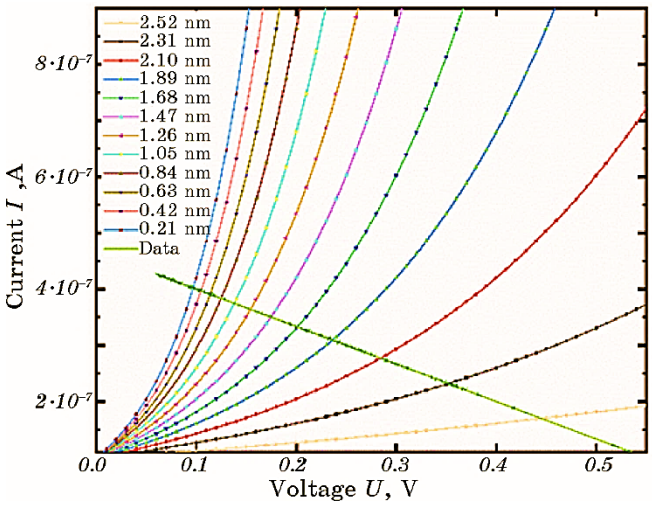

Fig. 2. Determination of dielectric thickness: the I–U_f characteristic (data line) measured during deformation is matched with calculated I–U curves for different MgO thicknesses (2.52–0.21 nm lines).

for different MgO thicknesses is experimentally obtained, and an empirical relationship for their calculation over a wide range of dielectric thicknesses is proposed. This relationship is used to determine the dielectric thicknesses by matching the measured I–U_f characteristic with the calculated I–U characteristics (Fig. 2).

The I–U_f characteristics obtained during the deformation of MgO intersects the calculated I–U characteristics corresponding to different dielectric thicknesses with a step of 0.21 nm. Using the intersection points, the values of the $\exp(h_f)$ on current I is constructed (Fig. 3). This relationship is approximated by a linear function in the selected co-ordinates. The dielectric deformation is then determined from the obtained functional relationship $h_f = f(\ln(I))$.

Based on the obtained data, the load–displacement curve ($P = f(h_f)$) is constructed (Fig. 4).

The loading is performed within the elastic deformation regime of the dielectric film (up to 10 MPa). No residual imprints associated with plastic deformation are observed during microscopic examination of the film surface, and the unloading curve returns to the initial point. The resulting diagram corresponds to the load–displacement response characteristic of instrumented (kinetic) indentation. The Young's modulus of the film is determined from the slope of the unloading curve in the range of $(0.8–0.4)P_{max}$. This portion of the curve is approximated by a linear function: red dash line in Fig. 4.

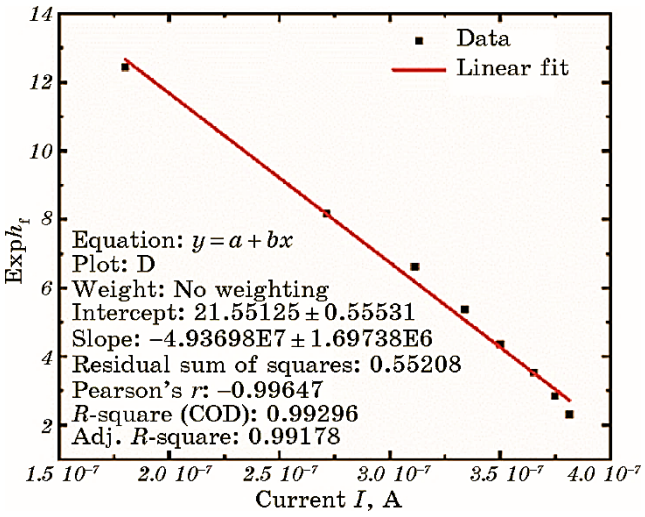

Fig. 3. Determination of dielectric deformation: the values of $\exp(h_f)$ on tunnelling current I constructed from the intersection points of experimental I–U_f characteristic and calculated I–U curves. The solid line is a linear fit in the selected co-ordinates.

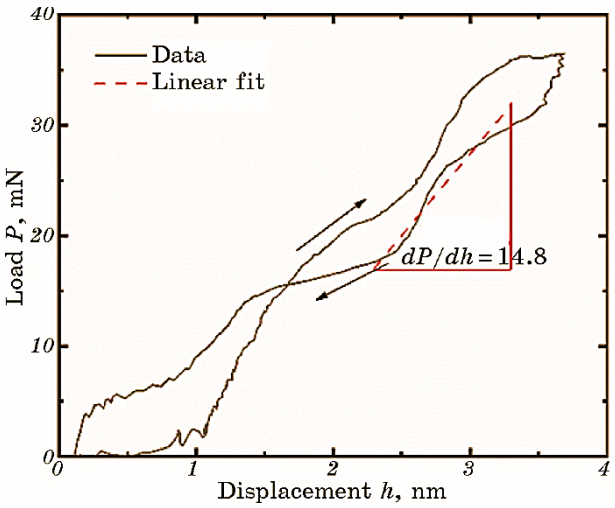

Fig. 4. Load–displacement curve of the MgO film obtained from tunnelling-current measurements.

Conventionally [29], the evaluation of the Young's modulus in indentation is performed using equations that account for the deformation of the indenter and the compliance of the measuring system. In the present study, the calculation is simplified, since only the deformation of the film is considered in constructing the load–displacement curve. Using the value of the Poisson's ratio of the MgO film [32], the contact area, and the slope of the unloading curve, the Young's modulus is calculated as:

$$E = \frac{\sqrt{\pi}(1-\nu^2)}{2\sqrt{A}} \frac{dP}{dh}, \tag{1}$$

where E is the Young's modulus, ν is the Poisson's ratio, A is the tip area.

The Young's modulus obtained for a 5 nm thick MgO film deposited on a 100 nm thick Fe film is ≅ 180 GPa. For bulk MgO, the Young's modulus ranges from 250 to 350 GPa depending on the crystallographic orientation [33]. The density of polycrystalline MgO is known to affect significantly the Young's modulus, which may vary within the range of 80–300 GPa [34]. Based on these data, the MgO film deposited by vacuum sputtering is estimated to have a density of approximately 3.2 g/cm^3, which is about 10% lower than that of single-crystalline MgO.

During repeated indentation at the same point, the load–displacement curve is determined using the same procedure. The resulting curve exhibits reduced hysteresis between the loading and un-

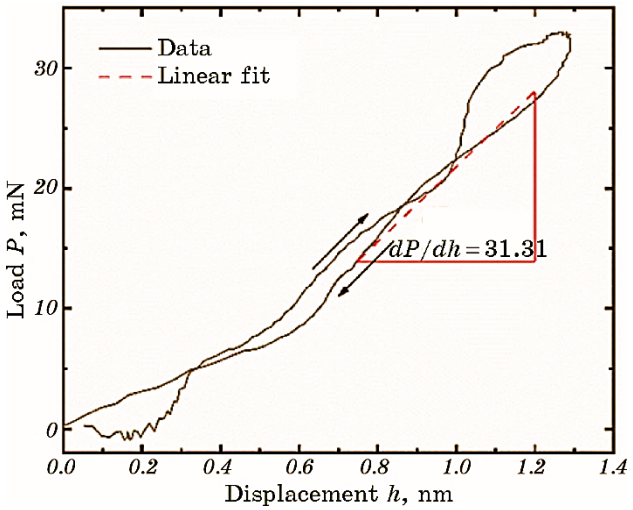

Fig. 5. Load–displacement curve obtained during repeated indentation at the same location of the MgO film.

loading curves, as well as smaller displacement under the same applied load (Fig. 5). The Young's modulus of the MgO film obtained under repeated loading is ≅ 380 GPa, which exceeds the reported values for bulk MgO [34]. The observed twofold increase in the Young's modulus can be attributed to the absence of plastic deformation and a reduction in porosity during repeated indentation.

4. CONCLUSION

A conductive-tip indentation method based on tunnelling current measurements is used to determine the elastic properties of ultrathin dielectric films. The proposed approach enables direct determination of dielectric film deformation by isolating its contribution from the total displacement, overcoming limitations of conventional nanoindentation techniques at the nanoscale.

Application of the method to MgO films with thicknesses below 10 nm demonstrates its capability to thickness changes and to calculating reliable load–displacement curves. The obtained Young's modulus of ≅ 180 GPa is consistent with bulk values of MgO with reduced density.

Repeated loading leads to a significant increase in the measured modulus to ≅ 380 GPa, which is associated with structural densification and a decrease in porosity. These results indicate that the mechanical properties of ultrathin films are strongly influenced by their structural state and loading history.

This contribution was created under the support of the project of the N.A.S. of Ukraine (No. 0122U002366).

AUTHORS' CONTRIBUTIONS

V. O. Burlakov performed the literature review and analysis of the current state of research, prepared the samples, and carried out the experimental investigations. Data acquisition, processing, and interpretation were conducted by V. O. Burlakov, including the implementation of the proposed method and the calculation of the mechanical properties of the investigated films.

O. V. Filatov supervised the overall direction of the research and provided methodological guidance. O. V. Filatov contributed to the development of the experimental approach, created software for processing the results, participated in the analysis and verification of the obtained results, and assisted in the interpretation of the data and theoretical considerations.

The manuscript, including the main text, discussion, and conclusions, was prepared jointly by both authors. All authors reviewed, revised, and approved the final version of the paper.

REFERENCES

1. T. D. Frazer, J. L. Knobloch, J. N. Hernández-Charpak, K. M. Hoogeboom-Pot, D. Nardi, S. Yazdi, W. Chao, E. H. Anderson, M. K. Tripp, S. W. King, H. C. Kapteyn, M. M. Murnane, and B. Abad, *Phys. Rev. Mater.*, **4**: 073603 (2020).
2. M. Bibes, J. E. Villegas, and A. Barthélémy, *Adv. Phys.*, **60**, Iss. 1: 5 (2011).
3. H. H. Radamson, X. He, Q. Zhang, J. Liu, H. Cui, J. Xiang, Z. Kong, W. Xiong, J. Li, J. Gao, H. Yang, S. Gu, X. Zhao, Y. Du, J. Yu, and G. Wang, *Micromachines*, **10**, Iss. 5: 293 (2019).
4. J.-H. Kim, H.-J. Kil, S. Lee, J. Park, and J.-W. Park, *ACS Omega*, **7**, Iss. 29: 25219 (2022).
5. Z. Zhao, H. Fu, R. Tang, B. Zhang, Y. Chen, and J. Jiang, *Int. J. Smart Nano Mater.*, **14**, Iss. 4: 510 (2023).
6. J. Moser, J. Güttinger, A. Eichler, M. J. Esplandiu, D. E. Liu, M. I. Dykman, and A. Bachtold, *Nature Nanotechnol.*, **8**: 493 (2013).
7. Y. T. Yang, C. Callegari, X. L. Feng, K. L. Ekinci, and M. L. Roukes, *Nano Lett.*, **6**, Iss. 4: 583 (2006).
8. M. Li, H. X. Tang, and M. L. Roukes, *Nature Nanotechnol.*, **2**: 114 (2007).
9. P. X.-L. Feng, *2020 IEEE 33rd Int. Conf. Micro Electro Mech. Syst. (MEMS)*, p. 212 (2020).
10. L. G. Zhou and H. Huang, *Appl. Phys. Lett.*, **84**: 1940 (2004).
11. R. J. Wang, C. Y. Wang, and Y. T. Feng, *Int. J. Mech. Sci.*, **130**: 267 (2017).
12. C. Cheng, P. S. Grant, and L. Lührs, *Adv. Electron. Mater.*, **6**, Iss. 1: 1900364 (2020).

13. C. Q. Sun, *Prog. Solid State Chem.*, **35**, Iss. 1: 1 (2007).
14. W. Xia and S. Keten, *J. Mater. Res.*, **30**: 36 (2015).
15. B. Gong, Q. Chen, and D. Wang, *Mater. Lett.*, **67**: 165 (2012).
16. Z. Ao and S. Li, *Nanoscale Res. Lett.*, **6**: 243 (2011).
17. K. Meganathan, G. Mangamma, M. J. Swaminadhan, V. Murugan, N. B. Shinde, S. Ghosh, and S. K. Eswaran, *J. Phys. Chem. Lett.*, **15**, Iss. 15: 4206 (2024).
18. B. Dieny, I. L. Prejbeanu, K. Garello, P. Gambardella, P. Freitas, R. Lehndorff, W. Raberg, U. Ebels, S. O. Demokritov, J. Akerman, A. Deac, P. Pirro, C. Adelmann, A. Anane, A. V. Chumak, A. Hirohata, S. Mangin, M. C. Onbaşlı, M. d'Aquino, G. Prenat, G. Finocchio, L. Lopez Diaz, R. Chantrell, O. Chubykalo-Fesenko, and P. Bortolotti, *Nature Electron.*, **3**: 446 (2020).
19. V. Burlakov, O. Filatov, and O. Pogorelov, *phys. status solidi (b)*, **258**, Iss. 4: 2000502 (2021).
20. V. O. Burlakov, O. E. Pogorelov, and O. V. Filatov, *Metallofiz. Noveishie Tekhnol.*, **42**, No. 7: 919 (2020) (in Ukrainian).
21. R. Lewandkyw, M. Grodzicki, P. Mazur, and A. Ciszewski, *Acta Phys. Pol. A*, **141**, No. 2: 116 (2022).
22. L. M. Kandpal, B. Taudul, E. Monteblanco, A. Kumar, K. Katcko, F. Schleicher, P. Gupta, S. Boukari, W. Weber, V. Da Costa, J. D. Costa, T. Böhnert, R. Ferreira, P. Freitas, M. Hehn, M. Alouani, P. K. Muduli, D. Lacour, and M. Bowen, *npj Spintronics*, **3**: 2 (2025).
23. V. O. Burlakov and O. V. Filatov, *Progress in Physics of Metals*, **26**, No. 4: 968 (2025).
24. J. N. Hernandez-Charpak, K. M. Hoogeboom-Pot, Q. Li, T. D. Frazer, J. L. Knobloch, M. Tripp, S. W. King, E. H. Anderson, W. Chao, M. M. Murnane, H. C. Kapteyn, and D. Nardi, *Nano Lett.*, **17**, Iss. 4: 2178 (2017).
25. K. Geng, F. Yang, and E. A. Grulke, *Mater. Sci. Eng. A*, **479**, Iss. 1–2: 157 (2008).
26. J. Hay and B. Crawford, *J. Mater. Res.*, **26**: 727 (2011).
27. R. Dingreville, J. Qu, and M. Cherkaoui, *J. Mech. Phys. Solids*, **53**, Iss. 8: 1827 (2005).
28. A. I. Fedorchenko, A. B. Wang, and H. H. Cheng, *Appl. Phys. Lett.*, **94**: 151904 (2009).
29. W. C. Oliver and G. M. Pharr, *J. Mater. Res.*, **7**: 1564 (1992).
30. J. G. Simmons, *J. Appl. Phys.*, **34**, Iss. 6: 1793 (1963).
31. V. O. Burlakov, O. Ye. Pohorelov, and O. V. Filatov, *Metallofiz. Noveishie Tekhnol.*, **45**, No. 2: 157 (2023).
32. *II–VI and I–VII Compounds; Semimagnetic Compounds* (Eds. O. Madelung, U. Rössler, and M. Schulz) (Berlin: Springer: 1999).
33. J. J. Swica and W. B. Crandall, *J. Am. Ceram. Soc.*, **48**, Iss. 2: 102 (1965).
34. D. Chung, J. J. Swica, and W. B. Crandall, *J. Am. Ceram. Soc.*, **46**, Iss. 9: 452 (1963).

Metallophysics and Advanced Technologies
Металофіз. новітні технол.
Metallofiz. Noveishie Tekhnol.
2026, vol. 48, No. 5, pp. 537–548
https://doi.org/10.15407/mfint.48.05.0537
Reprints available directly from the publisher

PACS numbers: 06.60.Vz, 46.55.+d, 61.72.Ff, 62.20.Qp, 68.47.De, 81.20.Vj, 81.40.Pq

Wear Behaviour of AA 7075 Joints Made by Double-Side Friction Stir Welding

V. Kiran Kumar[*,**], K. V. Durga Rajesh[*], S. R. Koteswara Rao[***], P. Venkateswara Babu[**], T. Srinivasa Rao[****]

[*]*Department of Mechanical Engineering,*
Koneru Lakshmaiah Education Foundation,
522 302 Vaddeswaram,
Andhra Pradesh, India
[**]*Department of Mechanical Engineering,*
Vasireddy Venkatadri Institute of Technology,
522 508 Nambur,
Guntur, Andhra Pradesh, India
[***]*Department of Mechanical Engineering,*
Sri Sivasubramaniya Nadar College of Engineering,
603 110 Chennai,
Tamil Nadu, India
[****]*Cornerstone Academy Private Limited,*
600 129 Chennai,
Tamil Nadu, India

Friction stir welding (FSW) of aluminium alloys became increasingly important across many industries, where the welded joints are required to have acceptable structural and functional properties. Conventional single-side FSW (SS-FSW), particularly, in thick-section joints, leads frequently to a reduction in weld properties, because of excessive heat input. Double-side friction stir welding (DS-FSW) has arisen as a potential solution to mitigate these limitations by balancing the thermal cycles and improving joint properties. In the present work, DS-FSW is executed on AA7075-T651 10 mm thick

Corresponding author: V. Kiran Kumar
E-mail: kiran.rlwc@gmail.com

Citation: V. Kiran Kumar, K. V. Durga Rajesh, S. R. Koteswara Rao, P. Venkateswara Babu, and T. Srinivasa Rao, Wear Behaviour of AA 7075 Joints Made by Double-Side Friction Stir Welding, *Metallofiz. Noveishie Tekhnol.*, **48**, No. 5: 537–548 (2026), DOI: 10.15407/mfint.48.05.0537

plates, and the resulting joints are evaluated methodically for wear performance with the help of a pin-on-disc wear testing setup. The microstructural features and precipitate morphology are also evaluated through optical microscopy and transmission electron microscopy. The DS-FSW joints exhibit superior wear performance, as evidenced by lesser friction coefficients and reduced specific wear rates, in comparison with both the base material and SS-FSW joints. Metallurgical characterization shows that the weld nugget of DS-FSW contained fine equiaxed grains, accompanied by significant re-precipitation of strengthening phases following their dissolution during welding. The combined effects of grain refinements and enhanced retaining of hardening precipitates are identified as the primary contributors to the improved wear resistance of DS-FSW joints. Overall, the findings establish DS-FSW as an effective technique for improving the wear properties of high-strength aluminium-alloy welds, chiefly in thick-section applications.

Key words: double-side friction stir welding, AA 7075, wear behaviour, optical microscopy, transmission electron microscopy.

Зварювання тертям з перемішуванням (ЗПТ) алюмінійових стопів стає все більш важливим у багатьох галузях промисловости, де від зварних з'єднань вимагаються прийнятні структурні та функціональні властивості. Традиційне одностороннє ЗПТ, особливо в товстоперерізних з'єднаннях, часто призводить до пониження властивостей зварного шва через надмірне підведення тепла. Двостороннє зварювання тертям з перемішуванням виникло як потенційне рішення для пом'якшення цих обмежень шляхом балансування термічних циклів і поліпшення властивостей з'єднань. У даній роботі двостороннє зварювання тертям з перемішуванням було виконано на пластинах AA7075-T651 товщиною у 10 мм, а одержані з'єднання були методично оцінені на зносостійкість за допомогою установки для випробування на знос «штифт на диску». Мікроструктурні особливості та морфологія преципітатів також були оцінені за допомогою оптичної мікроскопії та просвітлювальної електронної мікроскопії. З'єднання продемонстрували чудову зносостійкість, про що свідчать менші коефіцієнти тертя та понижені питомі швидкості зносу порівняно як з основним матеріялом, так і з'єднаннями одностороннім ЗПТ. Металургійна характеризація показала, що заготівка, зварювана двостороннім ЗПТ, містила дрібні рівновісні зерна, що супроводжувалося значним повторним осадженням зміцнювальних фаз після розчинення їх під час зварювання. Сукупний вплив подрібнення зерен і поліпшеного вмісту зміцнювальних осадів визначено як основні чинники, що сприяють поліпшенню зносостійкости з'єднань двостороннім ЗПТ. Загалом, одержані результати визначають двостороннє ЗПТ як ефективну техніку для поліпшення зносостійкости зварних швів високоміцних алюмінійових стопів, головним чином, у товстопрофільних застосуваннях.

Ключові слова: двостороннє зварювання тертям з перемішуванням, стоп AA 7075, зношування, оптична мікроскопія, просвітлювальна електронна мікроскопія.

(Received 31 August, 2025; in final version, 1 May, 2026)

1. INTRODUCTION

7000 series aluminium alloys, particularly, AA7075, are widely employed in automotive, aerospace, and structural sectors owing to their superior strength to weight ratios. However, their weldability is limited with conventional fusion techniques due to solidification cracking and strength degradation. Friction stir welding (FSW), a solid-state welding, has emerged as an effective alternative, with extensive studies addressing weld formation mechanisms, microstructural evolution, mechanical behaviour [1–3], and the influence of tool design [4–8] and process modelling [9, 10]. Advanced variants like friction stir additive manufacturing (FSAM) and friction stir processing (FSP) have further expanded applications in microstructural refinement, composite fabrication, and solid-state manufacturing [11–14].

Most FSW research has focused on plates below 10 mm thickness, while studies on thick sections highlight challenges in thermal management and joint performance [15–19]. Double-sided FSW, involving sequential welding from both sides, has been proposed to overcome these limitations by improving heat distribution and microstructural uniformity [20–22]. Although DS-FSW has shown promise in enhancing the mechanical performance of thick-section joints [23–26], limited work has explored its influence on wear properties of AA7075. To address this gap, the present study investigates DS-FSW of 10 mm thick AA7075 plates with emphasis on wear behaviour.

2. EXPERIMENTAL PROCEDURES

In this work, 10 mm thick rolled AA7075-T651 plates (110 mm × 250 mm) were used as the base material. The alloy composition [wt.%] was as follows: 6.00 Zn, 2.50 Mg, 1.40 Cu, 0.20 Cr, 0.08 Fe, 0.05 Ti, 0.03 Si, 0.01 Mn, with remaining Al. Double-side friction stir welds were produced sequentially, with the second pass executed such that the advancing side of Side *1* corresponded to the retreating side of Side *2*, ensuring balanced material flow and heat distribution. For comparison, single-side welds were also prepared. Welding parameters and tool designs were adopted from previous studies by the present authors [17, 23], with a constant tool tilt angle of 2° for both processes. Representative images of tools and welded plates are shown in Figs. 1 and 2.

Metallographic characterization was performed using optical microscopy and transmission electron microscopy (TEM). Specimens were extracted from heat-affected zone (HAZ), thermomechanically affected zone (TMAZ), weld nugget (WN) and base material (BM). Standard metallographic preparation included grinding with SiC papers, polishing with diamond suspension, and etching in Keller's reagent. Microstructural features were recorded at various magnifications using an

Fig. 1. Images of FSW tool: *a*—DS-FSW, *b*—SS-FSW.

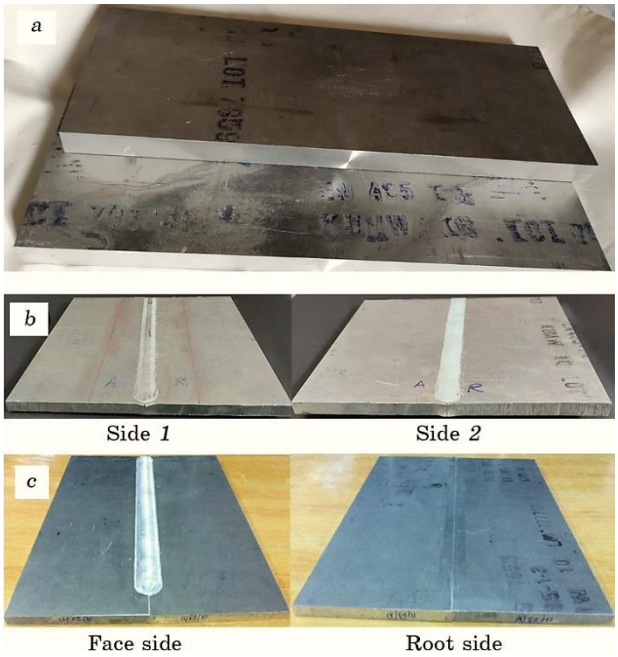

Fig. 2. Photographs of AA7075 plates before and after joining: *a*—As-received plates, *b*—DS- FSW, *c*—SS-FSW.

Olympus optical microscope.

Transmission electron microscopy was employed to examine precipitate morphology across different weld zones. Specimens were sectioned using an electrical discharge machine to minimize mechanical damage, followed by slow manual thinning to avoid thermal effects. Final thinning was performed electrolytically in a nitric acid–methanol solution to obtain electron-transparent foils. TEM observations were carried out using a JEM-2100 microscope.

Wear tests were performed using a pin-on-disc apparatus (Fig. 3) under dry sliding conditions following ASTM G99 standards. The set-up comprises a controller, testing unit and display unit. In the testing unit, a lever mechanism applied normal load to the stationary pin against the rotating disc, with the pin firmly held in a pin holder. Linear variable differential transducer (LVDT) sensors measured friction force and wear displacement, enabling calculation of the wear rate and friction coefficient. The controller unit regulated disc speed to maintain accurate sliding conditions.

Pin samples (10 mm×10 mm cross-section) were extracted from the weld nugget region (Fig. 4). The counter face disc was EN31 steel, 8 mm thick and 80 mm in diameter. Both pin and disc were ultrasonically cleaned in acetone for 10 min prior to testing. The pin was mounted vertically in the holder, and a normal load was applied against the rotating disc at the prescribed speed and sliding distance/time. Real-time friction force, friction coefficient, and wear displacement were recorded during testing. The test parameters considered for the work are provided in Table 1. The experiments were conducted on BM, SS-FSW and DS-FSW pin samples against the EN 31 rotating disc.

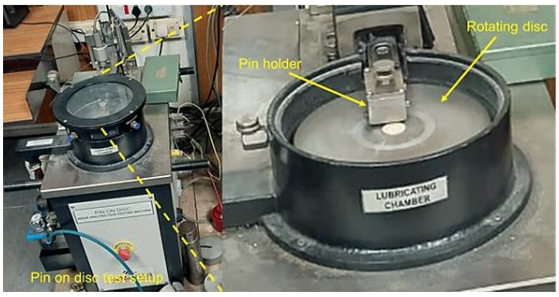

Fig. 3. Images of FSW tool: *a*—DS-FSW, *b*—SS-FSW

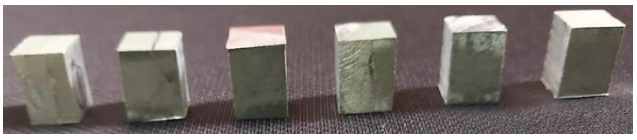

Fig. 4. Pin samples for tribological testing.

TABLE 1. Test parameters.

Parameter	Value	Unit
Normal load (F_n)	60, 80, 100	N
Speed (N)	500, 600, 700	rpm
Sliding time (t)	180	sec
Stationary pin roughness (R_a for pin)	0.31	microns
Rotating disc roughness (R_a for disc)	0.28	microns

All experiments were carried out for a constant duration of 180 seconds across different load–speed combinations. Each test was repeated three times, and the average values of specific wear rate and friction coefficient were considered. The weight of each pin was measured before and after testing, and weight loss was used to calculate the specific wear rate. Tribological parameters, namely friction coefficient and specific wear rate (SWR) [$mm^3/(N{\cdot}m)$], were determined using the following equations:

$$\text{friction coefficient} = F_f/F_n \; ; \; \text{specific wear rate} = (W_i - W_f)/(\rho F_n S) \; .$$

Here, F_f = force of friction [in N], F_n = normal load [in N], W_i = weight of the pin sample before the experiment [in g], W_f = weight of the sample after the experiment [in g], ρ = density of the pin material [in g/mm^3], and S = sliding distance [in m].

3. RESULTS AND DISCUSSION

3.1. Friction Coefficient

Figure 5 illustrates the effect of normal load and rotational speed on the friction coefficient. At 500 rpm, the coefficient increased with load due to higher interfacial pressure and ploughing action. Among all conditions, BM exhibited the highest friction coefficient, while DS-FSW showed the lowest, indicating superior resistance to sliding. With increasing rotational speed, the coefficient decreased for all samples; however, BM remained more sensitive to speed, particularly at lower ranges. DS-FSW consistently demonstrated a substantial reduction in friction coefficient, especially at higher speeds, suggesting smoother sliding with reduced asperity contact.

3.2. Specific Wear Rate

The influence of normal load and speed on specific wear rate is shown

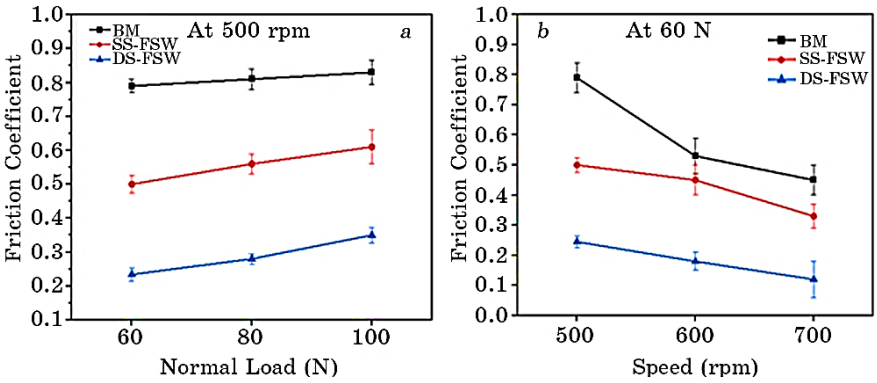

Fig. 5. Variation in friction coefficient with normal load and speed: *a*—normal load, *b*—speed.

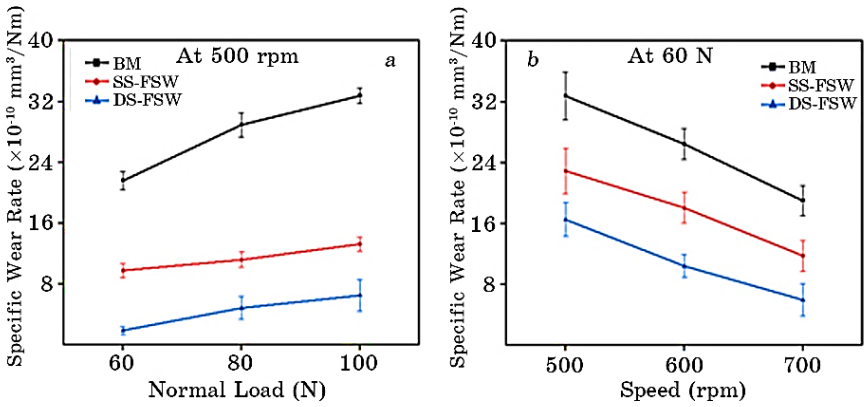

Fig. 6. Variation in specific wear rate with normal load and speed: *a*—normal load, *b*—speed.

in Fig. 6. BM again exhibited the highest SWR across all conditions, with a sharp rise at higher loads due to severe plastic deformation and material removal. DS-FSW samples demonstrated the lowest SWR, attributable to smoother and work-hardened surfaces coupled with lower interfacial shear stresses. With increasing rotational speed (500–700 rpm), SWR decreased for all samples, because higher speeds generally favoured reduced abrasive contact resulting in comparatively lower SWR.

Overall, DS-FSW joints exhibited superior tribological performance, simultaneously reducing both the friction coefficient and SWR compared to BM and SS-FSW samples. The combination of fine-grained microstructure and higher survival of strengthening precipitates likely contributed to their enhanced wear resistance. Favourable

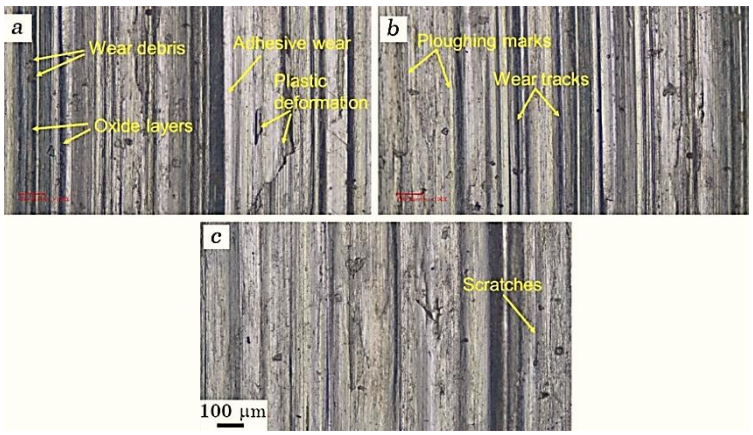

Fig. 7. The worn surfaces of pin samples at a load of 100 N and speed of 500 rpm: *a*—BM, *b*—SS-FSW, and *c*—DS-FSW.

tribological conditions were achieved under lower loads and higher speeds, where DS-FSW joints maintained stable friction and minimized material loss.

3.3. Surface Analysis

Typical worn surface micrographs of BM, SS-FSW, and DS-FSW samples are shown in Fig. 7.

Abrasive wear is evident through scratches, ploughing marks, and plastic deformation along the sliding direction, further aggravated by wear debris acting as third-body particles. Smooth smeared regions indicate adhesive wear, while dark oxide layers suggest oxidative wear due to frictional heating. These mechanisms were observed in all samples tested at 100 N load and 500 rpm. However, DS-FSW samples showed fewer grooves and lower weight loss, demonstrating reduced wear severity, consistent with their minimum specific wear rate values presented in Fig. 6.

3.4 Optical Microscopy

Representative micrographs of the base material and weld zones are given in Fig. 8. The base metal showed large, elongated pancake shaped grains (Fig. 8, *a*), typical of hot-rolled 7000 series alloys. In contrast, the weld nugget displayed fine equiaxed grains (Fig. 8, *b*), confirming extensive dynamic recrystallization brought by frictional heating and severe plastic deformation during FSW, in agreement with earlier reports [17, 18]. Grain refinement in the nugget zone is a key factor con-

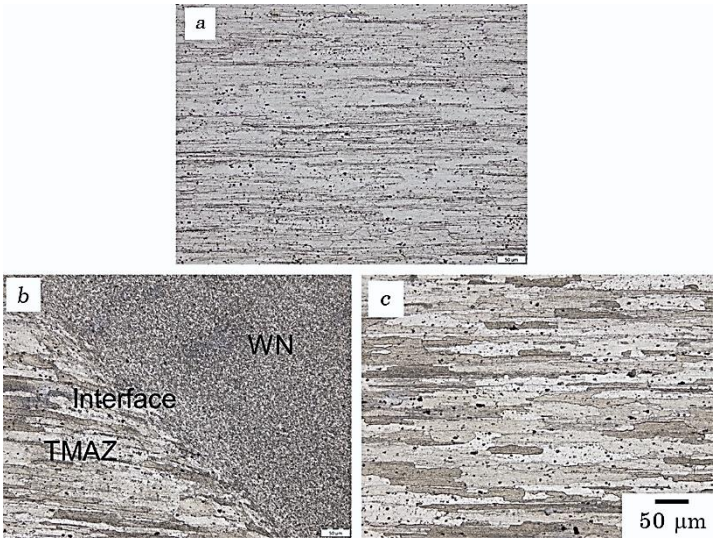

Fig. 8. Typical microstructures: *a*—base material, *b*—WN–TMAZ interface, and *c*—HAZ.

tributing to the reduced wear rate of the welded joints compared with the base material.

The thermo-mechanically affected zone represents the transition between the weld nugget and the heat-affected zone. In this region, the tool induces elevated temperatures and partial plastic deformation, resulting in elongated grains without recrystallization (Fig. 8, *b*). Alongside the TMAZ, the HAZ experiences only thermal exposure, leading to limited grain coarsening as shown in Fig. 8, *c*.

3.5. Transmission Electron Microscopy

Figure 9 illustrates the precipitate morphology of AA7075 in the T651 condition and within the TMAZ and HAZ. The base metal (Fig. 9, *a*) exhibited two distinct classes of strengthening precipitates, consistent with reports by Wert [27] and Lorimer [28]. Larger precipitates (40–60 nm) were identified either as Mg(Zn_2, AlCu) or Mg_{32}(Al, Zn)$_{49}$ phases, while smaller precipitates (10–15 nm) contributed significantly to the alloy high strength. Precipitation hardening achieved through deformation and artificial aging in the T651 temper conditions for the alloy ultimate tensile strength of ≅600 MPa, compared with ≅200 MPa in the annealed state.

The TEM micrograph of the TMAZ (Fig. 9, *b*) revealed partial dissolution of precipitates. While the larger particles remained largely unaffected, the finer precipitates showed slight coarsening. In the HAZ

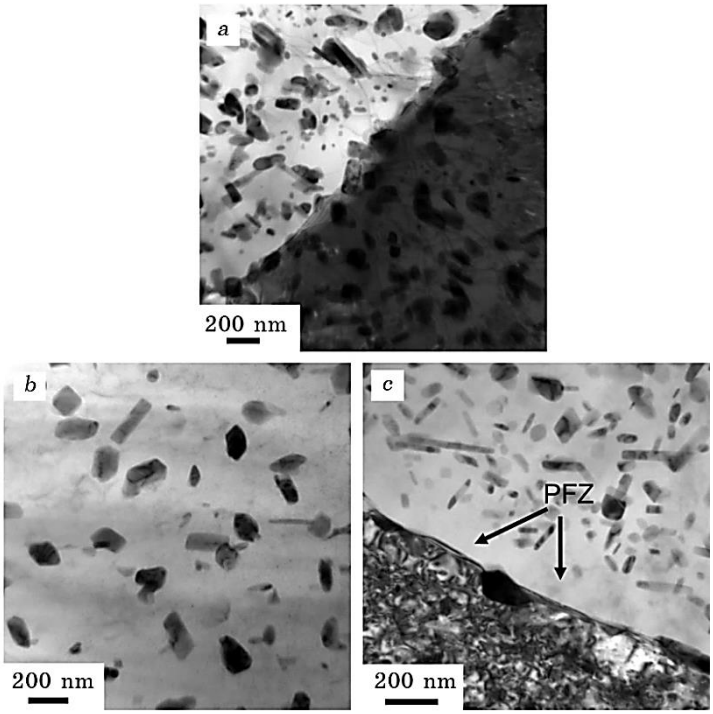

Fig. 9. Typical TEM images showing precipitate morphology in *a*—base material, *b*—TMAZ, and *c*—HAZ.

(Fig. 9, *c*), precipitates were uniformly distributed within grains, but precipitate-free zones (PFZs) were evident along grain boundaries. PFZ formation, widely reported in heat-treated AA7075 alloys, results from dissolution of boundary-adjacent precipitates during heating and their preferential re-precipitation along grain boundaries upon cooling.

TEM images of the weld nugget for SS-FSW and DS-FSW joints are shown in Fig. 10. The thermal cycles during FSW, typically above the solutionizing temperature but below the melting point, caused dissolution of strengthening precipitates, followed by partial re-precipitation and coarsening (Fig. 10, *a*). In DS-FSW joint (Fig. 10, *b*), a higher density and slightly larger size of precipitates were observed compared with SS-FSW, likely due to more favourable thermal conditions. The greater retention of hardening precipitates in DS-FSW explains its superior wear resistance.

4. CONCLUSIONS

1. AA7075–T651 aluminium alloy plates (10 mm thick) were success-

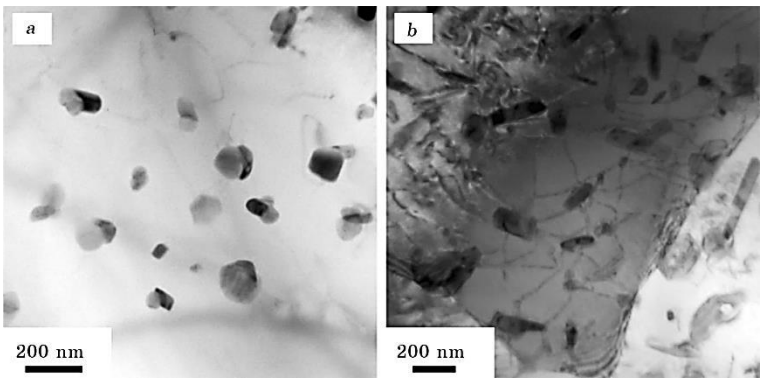

Fig. 10. Transmission electron micrographs of the WN: *a*—SS-FSW *b*—DS-FSW.

fully joined using single-side and double-side friction stir welding, and their wear performance was systematically evaluated.

2. DS-FSW joints exhibited superior wear resistance, reflected in lesser friction coefficients and specific wear rates than both the base material and SS-FSW joints. This improvement is attributed to dynamic recrystallization and enhanced retention of hardening precipitates in the weld nugget.

3. Friction coefficient and specific wear rate improved with applied normal load but decreased with sliding speed.

4. Microstructural analysis showed elongated grains in the base metal, refined into equiaxed grains in the weld nugget. The TMAZ contained plastically deformed grains, while the HAZ preserved the base metal structure with limited grain coarsening.

5. TEM observations confirmed dissolution and coarsening of precipitates in weld nugget, with DS-FSW promoting higher precipitate retention compared with SS-FSW, thereby contributing to improved wear behaviour.

AUTHORS' CONTRIBUTIONS

V. Kiran Kumar performed double side friction stir welding trials, conducted wear tests, examined weld microstructures and critically analysed the experimental results. K. V. Durga Rajesh supervised the project. S. R. Koteswara Rao supervised the project, devised the main conceptual ideas, verified analytical approaches, and provided critical feedback. P. Venkateswara Babu reviewed the literature and collected data on wear properties. T. Srinivasa Rao supervised the findings of this work, and wrote the manuscript with input from all authors. All authors approved the final version of the manuscript.

REFERENCES

1. W. M. Thomas, E. D. Nicholas, J. C. Needham, M. G. Church, P. Temple-Smith, and C. J. Dawes (G.B. Patent Application No. 9125978.8: December 1991).
2. R. S. Mishra and Z. Y. Ma, *Mater. Sci. Eng. R*, **50**, Iss. 1–2: 1 (2005).
3. G. Cam and S. Mistikoglu, *J. Mater. Eng. Perform.*, **23**, No. 6: 1936 (2014).
4. R. Rai, A. De, H. K. D. H. Bhadeshia, and T. DebRoy, *Sci. Technol. Weld. Joining*, **16**, Iss. 4: 325 (2011).
5. A. Arora, A. De, and T. DebRoy, *Scr. Mater.*, **64**: 9 (2011).
6. M. Mehta, A. Arora, A. De, and T. DebRoy, *Metall. Mater. Trans. A*, **42A**, No. 9: 2716 (2011).
7. A. Arora, M. Mehta, A. De, and T. DebRoy, *Int. J. Adv. Manuf. Technol.*, **61**: 911 (2012).
8. M. Mehta, A. De, and T. DebRoy, *Sci. Technol. Weld. Joining*, **19**, No. 6: 534 (2014).
9. X. He, F. Gu, and A. Ball, *Prog. Mater. Sci.*, **65**: 1 (2014).
10. Z. Y. Ma, A. H. Feng, D. L. Chen, and J. Shen, *Crit. Rev. Solid State Mater. Sci.*, **43**, Iss. 1: 269 (2018).
11. A. K. Srivastava, A. Nag, S. Dwivedi, A. R. Dixit, and S. Hloch, *Int. J. Adv. Manuf. Technol.*, **127**, Iss. 3–4: 1243 (2023).
12. A. K. Srivastava, N. Kumar, A. Saxena, and S. Tiwari, *Int. J. Cast Met. Res.*, **34**, Iss. 6: 169 (2021).
13. A. K. Srivastava, A. R. Dixit, M. Maurya, A. Saxena, N. K. Maurya, S. P. Dwivedi, and R. Bajaj, *Mater. Chem. Phys.*, **266**: 124572 (2021).
14. A. K. Srivastava, N. Kumar, and A. R. Dixit, *Mater. Sci. Eng. B*, **263**: 114832 (2021).
15. R. Kumar, K. Singh, and S. Pandey, *Trans. Nonferrous Met. Soc. China*, **22**, Iss. 2: 288 (2012).
16. P. Vincent, J. Alexis, E. Andrieu, J. Delfosse, M. C. Lafont, and C. Blanc, *Corros. Sci.*, **73**: 130 (2013).
17. T. Srinivasa Rao, G. Madhusudhan Reddy, and S. R. Koteswara Rao, *Trans. Nonferrous. Met. Soc. China*, **25**, No. 6: 1170 (2015).
18. T. Srinivasa Rao, S. R. Koteswara Rao, and G. Madhusudhan Reddy, *Materialwiss. Werkstofftech.*, **49**: 851 (2018).
19. T. Srinivasa Rao, M. Selvaraj, S. R. Koteswara Rao, and T. Ramakrishna, *Materialwiss. Werkstofftech.*, **52**: 308 (2021).
20. I. Hejazi, S.E. Mirsalehi, *Trans. Nonferrous Met. Soc. China*, **26**, Iss. 3: 676 (2016).
21. W. F. Xu, W. Zhang, and X. L. Wu, *Metall. Mater. Trans. A*, **48**: 1078 (2017).
22. M. R. Zhou, Y. Morisada, H. Fujii, and T. Ishikawa, *J. Mater. Process. Technol.*, **254**: 91 (2018).
23. V. Kiran Kumar, K. V. Durga Rajesh, S. R. Koteswara Rao, T. Ramakrishna, and T. Srinivasa Rao, *Metall. Res. Technol.*, **121**, No. 107: 1 (2024).
24. X. Zhou, Z. Li, J. Wang, and Y. Chen, *Wear*, **526**: 204993 (2023).
25. Y. Li, H. Wu, and B. Sun, *Mater. Today Commun.*, **26**: 102016 (2021).
26. A. Suresh, S. Natarajan, and R. Rathi, *Procedia Struct. Integr.*, **45**: 166 (2023).
27. J. A. Wert, *Scr. Mater.*, **15**, No. 4: 445 (1981).
28. G. W. Lorimer, *Precipitation Processes in Solids* (Eds. K. C. Russell and H. I. Aaronson) (Warrendale, PA: 1978).